1-1-2008

Particle Motion in Flows: Contributions to Airborne Aerosol Measurement

Maryam Darbeheshti
University of Denver

PARTICLE MOTION IN FLOWS:

CONTRIBUTIONS TO AIRBORNE AEROSOL MEASUREMENT

A Dissertation

Presented to

The Faculty of Engineering and Computer Science

University of Denver

In Partial Fulfillment

of the Requirements for the Degree

Doctor of Philosophy

---

by

Maryam Darbeheshti

November 2008

Advisor: Dr. James Charles Wilson

Author: Maryam Darbeheshti
Title: PARTICLE MOTION IN FLOWS: CONTRIBUTIONS TO AIRBORNE AEROSOL MEASUREMENT
Advisor: Dr. James Charles Wilson
Degree Date: November 2008

ABSTRACT

Accurate, in situ measurement of airborne particles is critical in understanding the global atmosphere. An airborne instrument is designed to sample and measure the aerodynamic diameter of particles in the size range of 1-30 μm. Knowledge of the aerodynamic size of a particle includes the impact of unknown variables such as shape, size and density of a particle. Particles of the same aerodynamic diameter have the same trajectory and settling velocity in air, regardless of their actual size, density or shape. Knowing the time a particle resides in air can improve the climate models substantially.

The developed instrument consists of a low turbulence inlet and a laser-Doppler velocimeter to sample and measure the super-micron particles all in one unit. Air enters the inlet at true air speed of the aircraft, which is a relatively high speed in the range of 100-200 ms^{-1}. The low turbulence inlet reduces the air speed to 5-10 ms^{-1} in a short distance without generation of additional turbulence. It uses boundary layer suction through a porous diffuser to remove a substantial amount of air that is responsible for turbulence generation and particle loss in deposition to the inlet walls. Reduction of turbulence makes it possible to model and solve the flows inside the inlets and calculate the particle trajectories using computational fluid dynamic (CFD) tools.

A new technique is developed to determine the size distribution of particles based on the motion of particles and measurement of the particles' velocity. Velocimetric measurement of particle size is achieved by slowing the velocity of the flow that is carrying the particles and measuring the velocity of the particles in response to this change. Larger particles have higher tendency to continue at a higher speed, while smaller particles tend to follow the air stream lines. A laser Doppler velocimeter (LDV) measures the velocity of the particles as they pass through the viewing volume of the velocimeter. The aerodynamic diameter of the particles and their concentration is determined from the velocity measurements.

Accurate determination of particle size distribution at the location of measuring sensor does not guarantee the accuracy of the ambient size distribution. The modification of number of particle due to particle loss, enhancement, and particles bouncing off the leading edge of the inlet is considered to accurately measure the ambient size distribution of particles.

This research work also focuses on quantifying the effects of particle enhancement in the low turbulence inlet used in ACE-Asia sampling inlet and the deposition of particles in transport through the bends of ACE-Asia and NOAA inlets. The effect of force of gravity on deposition efficiency of particles has also been analyzed.

Acknowledgements

I express sincere appreciation to my advisor, Dr. James Charles Wilson for his guidance and insight throughout the research.

Thanks go to the chair and the committee members, Dr. Donald H. Stedman, Dr. Marvin A. Hamstad, and Dr. Mohammad A. Matin for their valuable suggestions on the content of this thesis.

I also want to thank my husband Hamid and my daughters Yalda and Ida for their patience, support and love throughout my study.

Lastly, but in no sense the least, I am thankful to all colleagues and friends who made my stay at the University of Denver a memorable and valuable experience.

Table of Contents

Table of Figures

Table of Tables

Symbols and Acronyms

A	Hamaker constant
A	Actual concentration of particles at viewing volume
a	Velocity of sound in air
a_1	Constant of drag coefficient
a_2	Constant of drag coefficient
a_3	Constant of drag coefficient
α_p	Under-relaxation factor for pressure
BLS	Boundary Layer Suction
b_i	Source term in discretized Equations
CFD	Computational Fluid Dynamics
C_c	Cunningham slip correction factor
C_D	Coefficient of drag
C_2	Porous material inertial resistance coefficient
d	Diffuser diameter
dt	Time differential
D_a	Aerodynamic diameter of the particle
De	Dean number
D_p	Particle diameter
d_f	Fringe spacing
E	Total energy
F_D	Drag force on a particle)
F_x	Body force
f_D	Doppler frequency
g	Gravitational acceleration
I	Instrument output
J_f	Mass flux through face f
J_f	Mass flux correction factor
KE	Kinetic energy of bounce
L	Length scale
m	Mass flow rate
Ma	Mach number
N	Particle concentration
n	Iteration number
p	Pressure
p'	Pressure correction in the cell
p_s	Static pressure
P_b	Probability of bounce

R	Response matrix
R_1	Radius of limiting trajectory circle
R_2	Radius of viewing volume
Re	Reynolds number
Stk	Stokes number
t	Time
T	Temperature
u	Fluid velocity
u_p	Particle velocity
v_x	Axial velocity
v_r	Radial velocity
W	Width of the impactor throat
α	Porous material permeability Coefficient
Γ	Diffusion coefficient
λ	Mean free path of air
ρ	Density of air
ρ_p	Particle density
μ	Dynamic viscosity
$\overline{\overline{\tau}}$	Stress tensor
Δn	Thickness of the porous medium

Chapter 1. Introduction

This research work contributes in three areas of aerosol measurement from aircraft. An instrument is designed to accurately measure the aerodynamic diameter of suspended dust particles and their concentration in the 1-30 μm diameter range from aircraft. Inlet performance and correction factors are predicted for a low turbulence inlet used in the ACE-Asia field program in 2000 and the effect of gravity and particle deposition by inertia are calculated for an inlet used in NOAA research in 2004.

1.1 Airborne Measurement of Aerodynamic Diameter of Coarse Particles

In situ measurement of aerosols is critical in determination of the various effects of aerosol particles that describe the global atmosphere. Without accurate knowledge of aerosol concentration in various regions of the atmosphere, there is no way of testing aerosol models (Langner and Rodhe, 1991; Raes and Vandingenen, 1992).

Accurate, in situ measurement of dust particles is critical in understanding the global atmosphere. Dust particles have a direct effect on radiative budget of the atmosphere by reflecting the light back into space. They can also serve as nuclei in the formation of cloud particles and thus affect the radiative budget of the atmosphere indirectly.

Knowledge of the aerodynamic diameter of a particle includes the impact of unknown variables such as shape, size and density. Particles of the same aerodynamic diameter have the same trajectory and settling velocity in air, regardless of their actual

size, density or shape. Knowing the time a particle resides in air can improve the climate models substantially.

The developed instrument consists of a low turbulence inlet and a laser-Doppler velocimeter to sample and measure the super-micron particles all in one unit. Air enters the inlet at a relatively high speed of 100-200 ms^{-1}. The low turbulence inlet reduces the air speed to 5-10 ms^{-1} in a short distance without generation of additional turbulence. It uses boundary layer suction through a porous diffuser to remove a substantial amount of air that is responsible for turbulence generation and particle loss in deposition to the inlet walls. Reduction of turbulence makes it possible to model and solve the flows inside the inlets and calculate the particle trajectories in computational fluid dynamic tools.

A new technique is developed to determine the size distribution of particles based on the motion of particles and measurement of the particles' velocity. Velocimetric measurement of particle size is achieved by slowing the velocity of the flow that is carrying the particles and measuring the velocity of the particles in response to this change. Larger particles have higher tendency to continue at a higher speed, while smaller particles tend to follow the air stream lines. A laser Doppler velocimeter (LDV) measures the velocity of the particles as they pass through the viewing volume of the velocimeter. The aerodynamic diameter of the particles and their concentration is determined from the velocity measurements.

Accurate determination of particle size distribution at the location of measuring sensor does not guarantee the accuracy of the ambient size distribution. The modification of number of particle due to particle loss, enhancement, and particles bouncing off the

leading edge of the inlet needs to be considered to accurately measure the ambient size distribution of particles.

The laser-Doppler velocimetry technique is explained in detail in Chapter 3. Chapters 4 and 5 discuss the numerical analysis of the instrument.

1.2 Airborne Sampling of Coarse Particles in ACE-Asia Inlet

ACE-Asia inlet is a sampling instrument that consists of a low turbulence inlet (LTI), followed by a 65° bend. The low turbulence inlet is a conical diffuser that contributes to the enhancement of particles as a function of their size. Particles are lost in the bend in transporting to the measuring instruments. The particle enhancement in the conical diffuser and particle loss due to deposition to the bend are quantified to accurately measure the size distribution of ambient aerosol from aircraft.

Conical diffusers reduce the speed of the air as a result of the expansion in the area of flow. They also generate some turbulence due to the diverged streamlines. LTI takes care of the generated turbulence by removing about 80% of the air near the diffuser walls. Removal of this boundary layer air reduces the turbulence but at the same time removes the smaller particles that follow the flow and do not have enough inertia to resist the flow. Larger particles tend to remain in the domain due to their inertia, and therefore increase the mixing ratio of the sampled air as compared to the mixing ratio of the ambient air. Mixing ratio is defined as the number of the particles per unit mass of the air.

The Enhancement Factor, EF, determines the factor by which the particles are enhanced during sampling as a function of the particle size. The enhancement factor is determined using the methods of limiting trajectory and direct injection corresponding to

total flow and internal flow models. These calculations are explained in great detail in chapter 6.

ACE-Asia (http://saga.pmel.noaa.gov/field/aceasia/) was a research program sponsored by the NSF. It involved the NCAR C-130 aircraft, which was equipped with a low turbulence inlet. The enhancement factor described in Chapter 6 permitted the investigators whose samples were drawn through the LTI to relate the concentrations seen at their instruments to those in the ambient air (Kline et al., 2004).

The 65° bend, which is attached to the diffuser, is responsible for losing some of the sampled particles by deposition to the surface of the bend. The deposition efficiency of the particles in the bend is a function of particle size. The larger particles do not follow the curved streamlines in the bend and are therefore lost by hitting the outer surface of the bend. Chapter 7 covers the detailed analysis of the particle deposition efficiency.

1.3 Airborne Sampling of Coarse Particles in NOAA LTI under Gravity

The sampling of coarse particles in the NOAA LTI was studied to determine the effect of gravity in particle deposition in bends. The unit density particles in the range of 1-20 μm were introduced to the flow and the effect of gravity was analyzed to determine the trajectory of the particles exiting the bend. The details of including gravity in solving the equations of fluid flow and particle trajectory are presented in chapter 7. The losses in the bend under gravity were calculated to support the measurement made using an LTI in NOAA field studies with the NOAA P3 aircraft (Brock et al., 2008 and Brock et al., 2004).

Chapter 2. Descriptions of Fluid Dynamics and Particle Motion

2.1 Introduction

The numerical analysis of fluid flow and particle motion are presented in this chapter. Equations of conservation of mass and Navier-Stokes equation are solved in order to determine the flow field in the designed instrument, as well as in the low turbulence inlet (LTI) and the bend. The equations of particle motion are solved and the numerical solutions of particle trajectories are used to determine the velocity of particles. The calculated particle velocities are converted into the actual size distribution of aerosol particles in ambient air.

The solution of fluid flow and particle motion equations are also used to calculate the deposition efficiency and enhancement factor of particles in ACE-Asia and NOAA inlets.

The validity of numerical analysis of fluid flow and particle motion are verified in section 2.6.

2.2 Governing Equations for Fluid Flow

To determine the flow field in a fluid flow, the equations of conservation of mass (continuity) and conservation of momentum (momentum) need to be solved numerically. The Navier-Stokes equation is derived from the equation of momentum. The flow field inside and around the diffuser is calculated by solving the equations of continuity and momentum for compressible flow. The flow inside the bend is calculated for the incompressible flow.

Equations (2.1) and (2.2) are the continuity and momentum equations of fluid motion for compressible, viscous unsteady flows (White, 2003):

$$\frac{\partial \rho}{\partial t} + \nabla.(\rho \vec{v}) = 0 \tag{2.1}$$

and,

$$\rho\left(\frac{\partial v}{\partial t} + (v.\nabla)v\right) = \rho g - \nabla p + \nabla.\tau_{ij} \tag{2.2}$$

ρ is the air density, p is the pressure and τ_{ij} is the viscous stress sensor acting on the fluid element. $\partial v / \partial t$ is the local acceleration, which vanishes if the flow is steady, and $(v.\nabla)v$ is the convective acceleration, which arises when the fluid moves through regions of spatially varying velocity, as in a nozzle or diffuser.

The conservation of mass or continuity equation must hold in every flow field.

The assumption of constant density is valid as long as the pressure drop across the flow field is small compared to atmospheric pressure (Wilson, 1977).

A commonly accepted criterion for the assumption of incompressible flow is Ma ≤ 0.3 (White, 2003), where Ma is the flow Mach number and is defined as the ratio of velocity of flow to the speed of sound. For air at standard condition, a flow can be considered incompressible if the velocity is less than about 100 ms^{-1}.

The simplification of the above equations by assuming the steady flow removes all the terms that consist of derivatives of variables with respect to time, therefore all flow properties are functions of position only.

For incompressible flow with constant density and viscosity, the basic Equations of motion (2.1) and (2.2) reduce to:

$$\nabla \cdot v = 0 \tag{2.3}$$

$$\rho\left(\frac{\partial v}{\partial t} + (v.\nabla)v\right) = \rho g - \nabla p + \mu \nabla^2 v \tag{2.4}$$

The equations of continuity and momentum for 2-D steady, incompressible, laminar, axisymmetric flow are given by:

$$\frac{\partial v_x}{\partial x} + \frac{\partial v_r}{\partial r} + \frac{v_r}{r} = 0 \tag{2.5}$$

$$v_r \frac{\partial v_x}{\partial r} + v_x \frac{\partial v_x}{\partial x} = -\frac{1}{\rho}\frac{\partial p}{\partial x} + \frac{\mu}{\rho}\left(\frac{\partial^2 v_x}{\partial r^2} + \frac{\partial^2 v_x}{\partial x^2} + \frac{1}{r}\frac{\partial v_x}{\partial r}\right) \tag{2.6}$$

$$v_r \frac{\partial v_r}{\partial r} + v_x \frac{\partial v_r}{\partial x} = -\frac{1}{\rho}\frac{\partial p}{\partial r} + \frac{\mu}{\rho}\left(\frac{\partial^2 v_r}{\partial r^2} + \frac{\partial^2 v_r}{\partial x^2} + \frac{1}{r}\frac{\partial v_r}{\partial r} - \frac{v}{r^2}\right) \tag{2.7}$$

x is the axial coordinate, r is the radial coordinates, v_x is the axial velocity, and v_r is the radial velocity.

2.3 Governing Equations for Particle Motion

In order to determine the trajectory of particles, the equation of particle motion is solved repeatedly for specified intervals. The force balance on particles is given by (Fluent 6.2.16):

$$\frac{du_p}{dt} = F_D(u - u_p) + \frac{g_x(\rho_p - \rho)}{\rho_p} + F_x \tag{2.8}$$

F_x is the body force, u is the fluid velocity, u_p the particle velocity, ρ the fluid density, ρ_p the particle density, and F_D the drag force per unit mass.

The integration of particle force balance equation determines the particle velocity at each point along the flow path. A second integration of velocity with respect to time gives the particle's position at any specific point along the flow field.

The drag force for particles larger than 1 micron in diameter is given by:

$$F_D = \frac{18\mu}{\rho_p D_p^2} \frac{C_D \,\mathrm{Re}}{24} \tag{2.9}$$

D_p is the particle diameter, μ the dynamic viscosity of fluid, Re the relative Reynolds number and C_D is the drag coefficient.

The relative Reynolds number is:

$$\mathrm{Re} = \frac{\rho D_p |u_p - u|}{\mu} \tag{2.10}$$

and, the coefficient of drag is:

$$C_D = a_1 + \frac{a_2}{\mathrm{Re}} + \frac{a_3}{\mathrm{Re}^2} \tag{2.11}$$

a_1, a_2 and a_3 are constants that apply for smooth spherical particles (Moris and Alexander, 1972). Table 2.1 shows the values of a_1, a_2 and a_3 for different ranges of particle Reynolds number that covers both Stokes and ultra-Stokes regimes.

Table 2.1 Constant for determination of drag coefficient for spherical particles of different Reynolds numbers (Morris and Alexander, 1972).

$Re_p < 0.1$	$0.1 < Re_p < 1$	$1 < Re_p < 10$	$10 < Re_p < 100$
$a_1 = 0$	$a_1 = 3.69$	$a_1 = 1.222$	$a_1 = 0.617$
$a_2 = 24$	$a_2 = 22.73$	$a_2 = 29.167$	$a_2 = 46.5$
$a_3 = 0$	$a_3 = 0.0903$	$a_3 = -3.889$	$a_3 = -116.67$

This implies that for $Re_p < 0.1$, the particle drag force is calculated from the Stokes drag law and the drag coefficient is: $C_D = 24 / Re$.

Substituting the drag coefficient into the equation of drag force cancels out the effect of the drag coefficient from the equation for particles in Stokes regime ($Re_p < 0.1$).

Although the focus of this study is on the super-micron particles in the range of 1-30 micron in diameter, the Stokes drag law is also introduced to emphasize the importance of considering the slip correction factor for particles 1-10 micron. In general, the slip correction factor is introduced to the equation of drag force for particles smaller than 1 micron. This is because the assumption that gas velocity is zero at the surface of the particle is not true for particles whose diameter approaches the mean free path of the air. There is a slip at the surface of small particle that allows the particles to move faster than predicted by the Stokes law.

For accurate work, slip-correction factor should be applied for particles less than 10 micron (Hinds, 1982). Slip-correction factor for a 1- micron particle at standard conditions is 1.16. Slip-correction increases as pressure decreases, because the mean free path increases. The slip correction factor for particles 1-20 μm is included in Appendix C.

For sub-micron particles, F_D is given by the Stokes' drag law:

$$F_D = \frac{18\ \mu}{D_p^2\ \rho_p\ C_c} \tag{2.12}$$

C_c is the Cunningham slip-correction factor:

$$C_c = 1 + \frac{2\lambda}{D_p}\left[1.257 + 0.4 \exp\left(-1.1\frac{D_p}{2\lambda}\right)\right] \tag{2.13}$$

λ is the mean free path of air. According to the U.S. Standard Atmosphere, λ is given by:

$$\lambda = (2.333\ E-05)\ \frac{T}{P} \tag{2.14}$$

For pressures other than standard, (Hinds, 1982):

$$C_c = 1 + \frac{2}{P * D_p}\left[6.32 + 2.01 \exp\left(-0.1095\ P * D_p\right)\right] \tag{2.15}$$

P is the absolute pressure in cm Hg, and D_p is the particle diameter in micron.

Although the effect of slip-correction factor on particle's trajectory becomes significant for particles less than 1-micron in diameter, it can change the results of particle trajectory calculations for 1-10 micron particles. For example a 1-micron particle settles 16 % faster than the one predicted without consideration of slip correction factor.

2.4 Numerical Technique for Solving Fluid Flow

In order to determine the flow field in the diffuser, the governing equations of conservation of mass and momentum are solved numerically in Fluent. The following discussion of the solution technique follows the discussion in the Fluent documentation (fluent 6.2.16). The solution technique employs a finite volume approach to solve the equations. It first divides the domain into discrete control volumes using a computational grid. The next step is the integration of the governing equations to construct algebraic equations for the discrete dependent variables or unknowns such as velocity, pressure and temperature. The final step is to linearize the equations and solve the resultant linear equation system to yield updated values of the dependent variables. Basically, there are two numerical methods to solve the equations: segregated and coupled solution methods. The two methods employ a similar discretization process, but the approach used to linearize and solve the equations is different.

The numerical analysis in this work follows the segregated solution method. The segregated solver is a solution algorithm by which the governing equations of continuity and momentum are solved sequentially, i.e. segregated from each other. Because the governing equations are non-linear, several iterations of the solution loop must be performed before a converged solution is obtained.

In each iteration, first the fluid properties are up dated, based on the current solution. If the calculation has just begun, the fluid properties will be updated based on the initialized solution. The next step is to solve the momentum equations using current values of pressure and mass flow rate, in order to up date the velocity field. Now, this up-dated velocity may not satisfy the continuity equation. Therefore, a “Poisson-type”

equation for the pressure correction is derived from the continuity equation and the linearized momentum equation. This pressure correction equation is then solved to obtain the necessary corrections to the pressure and velocity fields and the mass flow rate such that continuity is satisfied. A check for convergence of the equation set is obtained.

2.4.1 Discretization of Conservation Equations

As mentioned earlier, Fluent uses the finite volume technique to discretize the conservation equations. This technique consists of integrating the governing equations about each control volume, yielding discrete equations that conserve each quantity on a control volume basis. Discretization of the governing equations is explained in detail in Appendix A. Several discretization methods are introduced based on the specific flow conditions.

2.4.2 Linearization of Conservation Equations

The discrete, non-linear governing equations are linearized to produce a system of equations for the dependent variables in every computational cell. The resultant linear system is then solved to yield an up dated flow field solution.

The manner in which the governing equations are linearized is implicit with respect to the dependent variables of interest. The implicit approach to linearize the governing equations means that for a given variable, the unknown value in each cell is computed using a relation that includes both existing and unknown values from neighboring cells. Therefore, each unknown will appear in more than one equation in the system, and these equations must be solved simultaneously to give the unknown quantities.

In segregated solution method, each discrete governing equation is linearized implicitly with respect to that equation's dependent variable. This will result in a system of linear equations with one equation for each cell in domain. In other words, the segregated approach solves for a single variable field, for example pressure, by considering all cells at the same time. It then solves for the next variable field by again considering all cells at the same time, and so on.

2.4.3 Solution Technique for Discretized Equations

The segregated solver applies the following approach to the discretization of the momentum and continuity equations and their solution:

Considering the steady-state continuity and momentum equations in integral form:

$$\oint \rho \vec{v} . d\vec{A} = 0 \tag{2.16}$$

$$\oint \rho \vec{v} \vec{v} . d\vec{A} = -\oint p I . d\vec{A} + \oint \overline{\overline{\tau}} . d\vec{A} + \int_V \vec{F} \, dV \tag{2.17}$$

where I is the identity matrix, $\overline{\overline{\tau}}$ is the stress tensor, and $\vec{F}$ is the force vector.

The continuity Equation (2.16) may be integrated to give the discrete Equation (2.18):

$$\sum_f^{N_{faces}} J_f A_f = 0 \tag{2.18}$$

where J_f is the mass flux through face f, ρv_n.

The discretization scheme described in Appendix A for a scalar transport equation is also used to discretize the momentum equations. For example, the x-momentum equation can be obtained by setting: $\phi = u$

$$a_p\, u = \sum_{nb} a_{nb}\, u_{nb} + \sum p_f A.\hat{i} + S \tag{2.19}$$

If the pressure field and face mass fluxes were known, Equation (2.19) could be solved in the manner outlined in Appendix A, and a velocity field obtained. However, the pressure field and face mass fluxes are not known a priori and must be obtained as a part of the solution. There are important issues with respect to the storage of pressure and the discretization of the pressure gradient term; these are addressed next.

Fluent uses a co-located scheme, whereby pressure and velocity are both stored at cell centers. However, Equation (2.19) requires the value of the pressure at the face between cells C_0 and C_1 (Refer to Appendix A). Therefore, an interpolation scheme is required to compute the face values of pressure from the cell values.

As mentioned earlier, the momentum and continuity equations are solved sequentially. In this sequential procedure, the continuity equation is used as an equation for pressure. However, pressure does not appear explicitly in Equation (2.18) for incompressible flows, since density is not directly related to pressure. The SIMPLE (Semi-Implicit Method for Pressure-Linked Equations) family of algorithms is used for introducing pressure into the continuity equation.

In order to proceed further, it is necessary to relate the face values of velocity, v_n, to the stored values of velocity at the cell centers. In Fluent, the face value of velocity is not averaged linearly; instead, momentum-weighted averaging, using weighting factors based on the a_p coefficient from Equation (2.19) is performed. Using this procedure, the face flux, J_f, may be written as:

$$J_f = \hat{J}_f + d_f (p_{C_0} - p_{C_1}) \tag{2.20}$$

p_{C_0} *and* p_{C_1} are the pressures within the two cells on either side of the face, and $\hat{J}_f$ contain the influence of velocities in these cells. The term d_f is a function of $\overline{a}_p$, the average of the momentum equation a_p coefficients for the cells on either side of face *f*.

2.4.4 Pressure-Velocity Coupling

Pressure-velocity coupling is achieved by using Equation (2.20) to derive an equation for pressure from the discrete continuity Equation (2.18). A SIMPLE algorithm is used for a relationship between velocity and pressure to enforce mass conservation and to obtain the pressure field.

If the momentum equation is solved with a guessed pressure field p^*, the resulting face flux, J^*_f, computed from Equation (2.20)

$$J^*_f = \hat{J}^*_f + d_f(p^*_{C_0} - p^*_{C_1}) \tag{2.21}$$

does not satisfy the continuity equation. Consequently, a correction J'_f is added to the face flux J^*_f so that the corrected face flux, J_f

$$J_f = J^*_f + J'_f \tag{2.22}$$

satisfies the continuity equation. The SIMPLE algorithm postulates that J'_f be written as

$$J'_f = d_f(p'_{C_0} - p'_{C_1}) \tag{2.23}$$

where *p*'is the cell pressure correction.

The SIMPLE algorithm substitutes the flux correction Equations (2.22) and (2.23) into the discrete continuity Equation (2.18) to obtain a discrete equation for the pressure correction p' in the cell:

$$a_p\, p' = \sum_{nb} a_{nb}\, p'_{nb} + b \tag{2.24}$$

The source term b is the net flow rate into the cell:

$$b = \sum_{f}^{N_{faces}} J_f^* A_f \tag{2.25}$$

The pressure-correction Equation (2.24) may be solved using the algebraic multigrid (AMG) method. Once a solution is obtained, the cell pressure and the face flux are corrected using

$$p = p^* + \alpha_p p' \tag{2.26}$$

$$J_f = J_f^* + d_f (p'_{C_0} - p'_{C_1}) \tag{2.27}$$

α_p is the under-relaxation factor for pressure(see Appendix A). The corrected face flux, J_f, satisfies the discrete continuity equation identically during each iteration.

2.5 Numerical Technique for Solving Particle Trajectories

2.5.1 Integration of Trajectory Equations

Integration in time of Equation (2.8) yields the velocity of the particle at each point along the trajectory, with the trajectory itself predicted by:

$$\frac{dx}{dt} = u_p \tag{2.28}$$

The trajectory equations are solved by stepwise integration over discrete time steps. The accuracy of the discrete phase calculation thus depends on the time accuracy of the integration and upon the appropriate coupling between the discrete and continuous phases when required. Equations (2.8) and (2.28) are solved in each coordinate direction to predict the trajectories of the discrete phase.

Assuming that the term containing the body force remains constant over each small time interval, and linearizing any other forces acting on the particle, the trajectory equation can be rewritten in simplified form as:

$$\frac{d\,u_p}{d\,t} = \frac{1}{\tau_p}\left(u - u_p\right) \tag{2.29}$$

τ_p is the particle relaxation time. Fluent uses a trapezoidal scheme for integrating Equation (2.29), which gives:

$$\frac{u_p^{n+1} - u_p^n}{\Delta t} = \frac{1}{\tau}\left(u^* - u_p^{n+1}\right) + \ldots \tag{2.30}$$

$$u^* = \frac{1}{2}\left(u^n + u^{n+1}\right) \tag{2.31}$$

$$u^{n+1} = u^n + \Delta t\, u_p^n . \nabla u^n \tag{2.32}$$

n represents the iteration number.

Equations (2.28) and (2.29) are solved simultaneously to determine the velocity and position of the particle at any given time. In all cases, care must be taken that the time step used for integration is sufficiently small that the trajectory integration is accurate in time.

There are two parameters to control the time integration of the particle trajectory equations:

- The number of particles per cell used to set the time step for integration within each control volume.
- The maximum number of time steps used to abort trajectory calculations when the particle never exits the flow domain.

The maximum number of steps is the maximum number of time steps used to compute a single particle trajectory via integration of Equations (2.8) and (2.28). When the maximum number of steps is exceeded, Fluent abandons the trajectory calculation for the current particle injection and reports the trajectory as incomplete. The limit on the number of integration time steps eliminates the possibility of a particle being caught in a recirculation region of the continuous phase flow field and being tracked infinitely. Length scale controls the integration time step size used to integrate the equations of motion for the particle. The integration time step is computed by Fluent based on a specified length scale L, and the velocity of the particle u_p and of the continuous phase u_c,

$$\Delta t = \frac{L}{u_p + u_c} \tag{2.33}$$

L is the length scale which is proportional to the integration time step and is equivalent to the distance that the particle will travel before its motion equations are solved again and its trajectory is updated. A smaller value for the length scale increases the accuracy of the trajectory. It is worth mention that particle positions are always calculated when particles enter or leave a cell regardless of the length scale specified. The time step for the integration will be such that the cell is traversed in one step.

In general, if a domain consists of N grid cells, then the maximum number of steps would be length scale times the number of grid cells, N.

2.6 Validation of Calculation of Particle Trajectories in Laminar Flow

2.6.1 Introduction

Verification of the validity of numerical analysis is the key to the successful design of the practical aerosol measuring instrument, as well as the successful prediction of enhancement factors and losses in the bend. The agreement between theoretical analysis of a model and experimental results of the practical application of the actual instrument allows the confident application of theory to practical instrument design

The comparison of experimental data with numerical modeling of laminar flow in two different geometries is presented in this section.

2.6.2 Comparison of Experimental Data with Numerical Results

2.6.2.1 Deposition of Particles in a 90° Bend

In order to validate the numerical calculation of particle trajectories in laminar flow, the deposition efficiency of particles in the size range of 1-20 μm in an inlet with a 90° bend are calculated in Fluent. The numerical results of this calculation are compared with the experimental results obtained from the study of the particle deposition under the same flow conditions and inlet geometries.

The experimental inlet is a 90° bent tube with an internal diameter of 5.03×10^{-3} m. The entrance length prior to the 90° bend is extended 20 times the entrance diameter of the tube, which delivers a partially developed flow to the bend. The flow Reynolds number is set at Re = 1000. Particles in the range of 1-20 μm in diameter are injected to the flow and the particles exiting the bend are counted. The deposition efficiency of the particles is calculated as the ratio of the number of particles deposited in the bend to the total number of particles sampled.

The 3-D axisymmetric model of an inlet with exact same geometry and flow conditions of the experimental inlet was generated in Fluent. The flow field was calculated using the equations of continuity and momentum for axisymmetric, steady, laminar, incompressible flow. Then, the unit density particles in the size range of 1-20 μm were injected to the flow and the particle trajectories were calculated using the equation of particle motion. The deposition efficiency of the particles that entered the inlet was then calculated as a function of particles Stokes number.

The parameters that affect the particle deposition efficiency in bends are: flow Reynolds number, particle Stokes number, Curvature ratio of the bend, Dean number, and the inlet velocity profile. For the validation of numerical analysis, the effects of Stokes number and inlet velocity profile on particle deposition efficiency are investigated, keeping the flow Re and curvature ratio of the bend constant. The density of particles has no effect on their deposition pattern as a function of Stokes number.

Dean number is the ratio of Reynolds number to the square root of curvature ratio. At a fixed Re and inlet diameter, as the radius of curvature increases, the curvature ratio increases and as a result the Dean number decreases. Smaller Dean number means less particle deposition at the same Stokes number. Therefore, a sampling instrument with a larger radius of curvature, (or smaller degree of bend) results in sample aerosol characteristics that are closer to reality.

The effect of inlet velocity profile on particle deposition efficiency has been studied numerically in Fluent and the results have been compared with the numerical analysis for the different inlet velocity profiles (Tsai and Pui, 1990) and (Cheng and Wang, 1981). Tsai and Pui have studied the effect of uniform, partially developed and

fully developed inlet velocity profiles on deposition efficiency of particles in 90° bends. Cheng and Wang have also studied a case of bend deposition with fully developed flow entering the bend.

The uniform inlet velocity profile results in less particle deposition as compared to the parabolic velocity profile. In a parabolic profile, the centrifugal forces acting on the center streamlines are increased. Therefore, the streamlines will skew toward the outside of the bend, which will increase the concentration of particles close to the outer wall. As the particles pass through the bend, less deviation from the streamline is required for the particles to contact the wall, thus increasing the particle deposition efficiency. Therefore, a uniform inlet velocity profile and an increased curvature ratio (or a decreased Dean number) are the best settings as far as the particle losses in bend are concerned at a fixed Re. They have worked on different geometries which are summarized in Table2.2.

As seen in the table, Tsai and Pui consider the after bend extension of 10D in all of their numerical modeling. The particle deposition in the straight portion after the bend can be significant.

Table 2.2 The Models generated in Fluent for comparison between numerical analysis and experimental results.

Fluent Models Generated for Comparison	Geometry
Experimental Study (Pui et. al, 1987) Partially Developed Profile	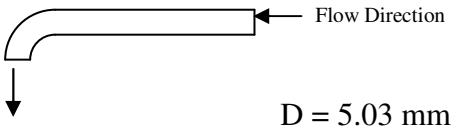 D = 5.03 mm Entrance Length = 20D After Bend Extension = 0
Numerical Study (Cheng & Wang, 1981) Fully Developed Profile	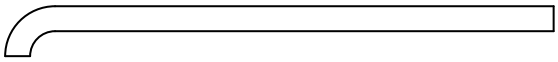 Entrance Length = 60D After Bend Extension = 0
Numerical Study (Tsai and Pui, 1990) Uniform Velocity Profile	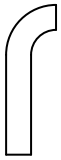 Entrance Length = 0 After Bend Extension = 10D
Numerical Study (Tsai and Pui, 1990) Partially Developed Profile	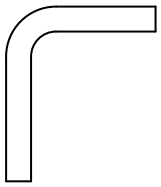 Entrance Length = 5D After Bend Extension = 10D
Numerical Study (Tsai and Pui, 1990) Fully Developed Profile	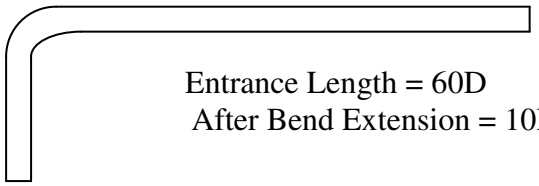 Entrance Length = 60D After Bend Extension = 10D

Tsai and Pui consider a 5D entrance length for the numerical modeling of the case with partially developed inlet profile. Partially developed flow is a general term used for all the flows that are not fully developed. They do not specify the entrance length required to achieve a fully developed flow at the bend entrance. There are different opinions on how long should the entrance length to be for a fully developed inlet profile, however, we consider 60D entrance length for our numerical model. The flow solution in Fluent agreed with our assumption.

Cheng & Wang numerical results are calculated for flow Re=1000, with a curvature ratio of R_o=8, whereas other results (Tsai & Pui, 1990) are for R_o=5.7. Lower the curvature ratio, higher the particle deposition efficiency. Therefore, we should expect Tsai & Pui to show higher particle deposition efficiency than what Cheng & Wang have predicted for the same Stokes number.

Four models are generated in Fluent with the exact geometry and flow conditions of the reported numerical data. Therefore, a total of five 90° bend models are solved in Fluent each to compare with one of the available data (4 numerical and 1 experimental). The flow Re=1000, Tube I.D. =5.03×10^{-3} m, Curvature Ratio, R_o=5.7 in all the cases.

The particle losses in the straight portion after the bend are not included in experimental determination of deposition efficiency by Pui et.al, 1987, and in numerical analysis of bend deposition by Cheng & Wang, 1981. On the other hand, the numerical results of particle deposition efficiency of Tsai and Pui include the particle deposition efficiency in the bend and a straight portion of 10D following the bend. It is seen that the particle deposited after the bend is only a small fraction of the total deposition efficiency,

in most cases, less than 2%. When De is large and the inlet velocity profile is uniform, this after-bend deposition efficiency can increase to about 8% (Tsai and Pui, 1990).

Pui et al. experimental data were obtained under a condition that flow was not fully developed at the inlet of the bend. Therefore, the data points are scattered around the numerical curves for the case of partially developed inlet profile. In the numerical study, he considers three cases of parabolic, partially developed with a 5D entrance length, and uniform velocity profiles at the inlet to the bend. The highest particle deposition efficiency occurs with the parabolic inlet profile due to the stronger secondary flow and also the fact that the axial velocity profile is skewed towards the outside of the bend.

Figure 2.1 shows the comparison between the experimental results (Pui et al., 1987) and the numerical results obtained in this work from modeling the inlet with similar geometry and flow parameters in Fluent.

Figure 2.2 adds the other two available numerical results of bend deposition efficiency (Tsai & Pui, 1990 and Cheng & Wang, 1981) to Figure 2.1.

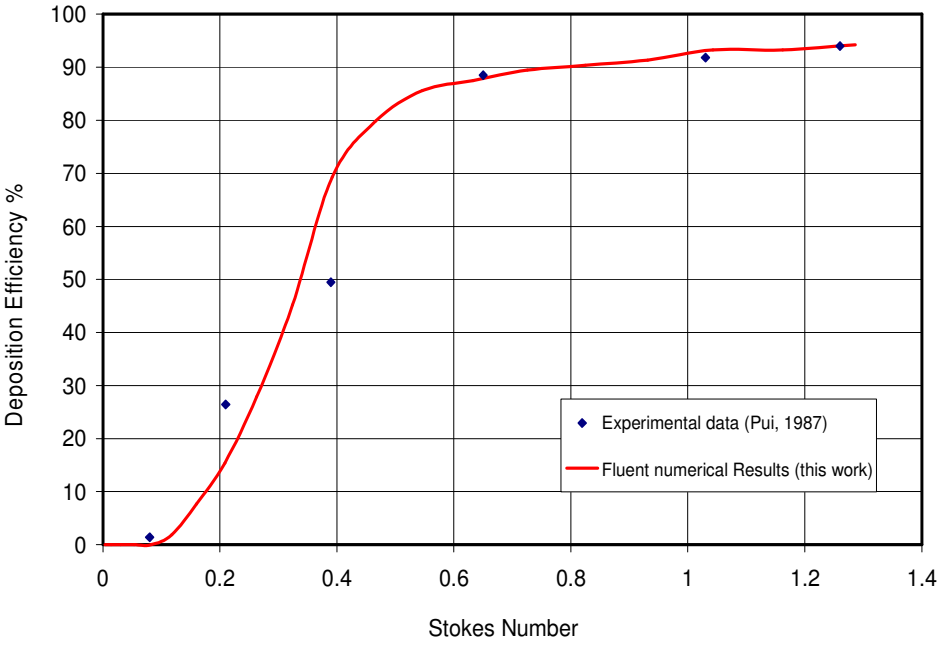

Figure 2.1 Deposition efficiency of particles in a 90° bend, comparison of Fluent numerical results (this work) with experimental data (Pui et al., 1987)for a partially developed inlet velocity profile, Re=1000, De=419, tube I.D.=5.03 mm.

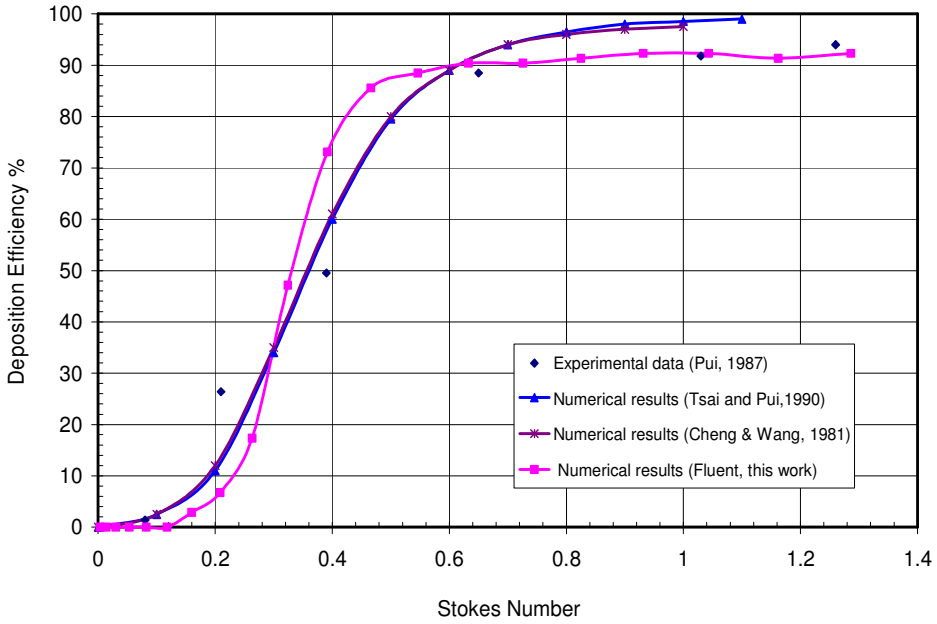

Figure 2.2 Comparison of experimental data (Pui, et.al, 1987) with three numerical results (Tsai and Pui, 1990; Cheng and Wang, 1981; Fluent (this work).

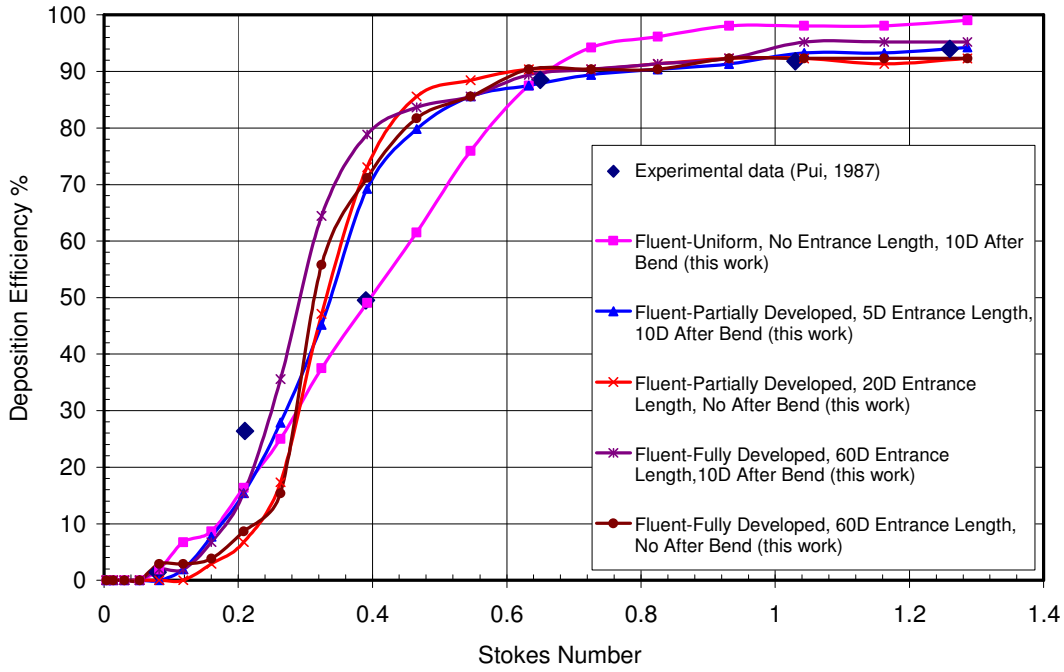

Figure 2.3 Deposition efficiency of particles in a 90° bend, comparison of five Fluent calculations with different velocity inlet profiles (this work) with experimental data (Pui et al., 1987), Re=1000, De=419, tube I.D.=5.03 mm.

Figure 2.3 shows the deposition efficiency as a function of Stokes number for five different geometries that were created in fluent to match the geometries of the previous calculations by Tsai & Pui, 1990 and Cheng & Wang, 1981. The solved cases in Fluent all have the same flow Re and curvature ratio with different velocity inlet profiles. The comparison of the Fluent numerical results with the experimental data shows a close agreement for particles larger than 13 micron in diameter which corresponds to Stokes number greater than 0.6. However, the Stk_{50} for the experimental data (0.39) matches with Stk_{50} for the Fluent numerical results of a uniform velocity inlet profile.

2.6.2.2 Determination of Particle Trajectory in Impactors

The determination of particle trajectory in impactors and the agreement between the experimental data and the numerical results shows the successful performance of the impactor designed by Marple and Liu, 1974. However, in order to validate the numerical results calculated by Fluent in the instrument design and in low turbulence inlet, the geometry of the impactor should be compatible to the geometry of the designed instrument and LTI. The impactor creates a stagnation region prior to the impaction surface. Marple and Liu have successfully predicted the flows through the stagnation region. There is a stagnation region developed in the measurement region of the designed instrument as well as LTI. This stagnation region is responsible for the reduction of air velocity from about 100 ms^{-1} to around 4-5 ms^{-1}, and therefore, generation of laminar flow in the region which allows the determination of the flow field by Fluent.

Inertial impactors collect and separate airborne particles into finite size ranges. The impactor performance based on particle trajectory calculations is determined numerically by solving the equations of particle motion. The flow fields in impactors were previously determined by solving the Navier-Stokes equations. The results of numerical analysis are then verified experimentally. The effects of jet-to-plate distance, jet Reynolds number and jet throat length on impactor efficiency curves have been studied (Marple and Liu, 1974).

To calculate the particle trajectory through the rectangular impactor, the equation of particle motion in the x-y coordinate is given by (Marple and Liu, 1974):

$$m\frac{d^2x'}{dt'^2} = \frac{3\pi\mu D_p}{C}\left(V_{x'} - \frac{dx'}{dt'}\right) \tag{2.34}$$

$$m\frac{d^2y'}{dt'^2} = \frac{3\pi\mu D_p}{C}\left(V_{y'} - \frac{dy'}{dt'}\right) \tag{2.35}$$

which can be written in dimensionless form as:

$$\frac{Stk}{2}\frac{d^2x}{dt^2} = \left(V_x - \frac{dx}{dt}\right) \tag{2.36}$$

$$\frac{Stk}{2}\frac{d^2y}{dt^2} = \left(V_y - \frac{dy}{dt}\right) \tag{2.37}$$

$$Stk = \frac{\rho_p C V_0 D_p^2}{9\mu W} \tag{2.38}$$

x, y are the dimensionless rectangular coordinates, x', y' are the rectangular coordinates, V_x, V_y are the dimensionless gas velocity and $V_{x'}, V_{y'}$ are the gas velocity. *W* is the width of the throat. V_0 is the mean gas velocity at throat.

The size of the particle is then determined from Equation (2.38). A particle is considered to have impacted if its center has come to a distance of one particle radius from the plate. In many cases, it is only necessary to decide whether a particle will actually impact, given its position and velocity components at a point sufficiently close to the plate.

To verify the results of the numerical calculations, polydisperse particles in the range of 6-14 μm with a density of 1050 Kgm^{-3} were directed to the impactor and the point of impact of the particles and the particle diameter were measured and compared with the theoretical calculations. Fig 2.3 shows the comparison of theoretical and

experimental impaction points in the variable point impactor for Re=2000 and particle starting point at $Xc/W = 0.407$.

Xc is the distance of particle directing to the impactor from the center of the variable point impactor.

X_i is the particle's point of impact or the distance from center of impaction plate.

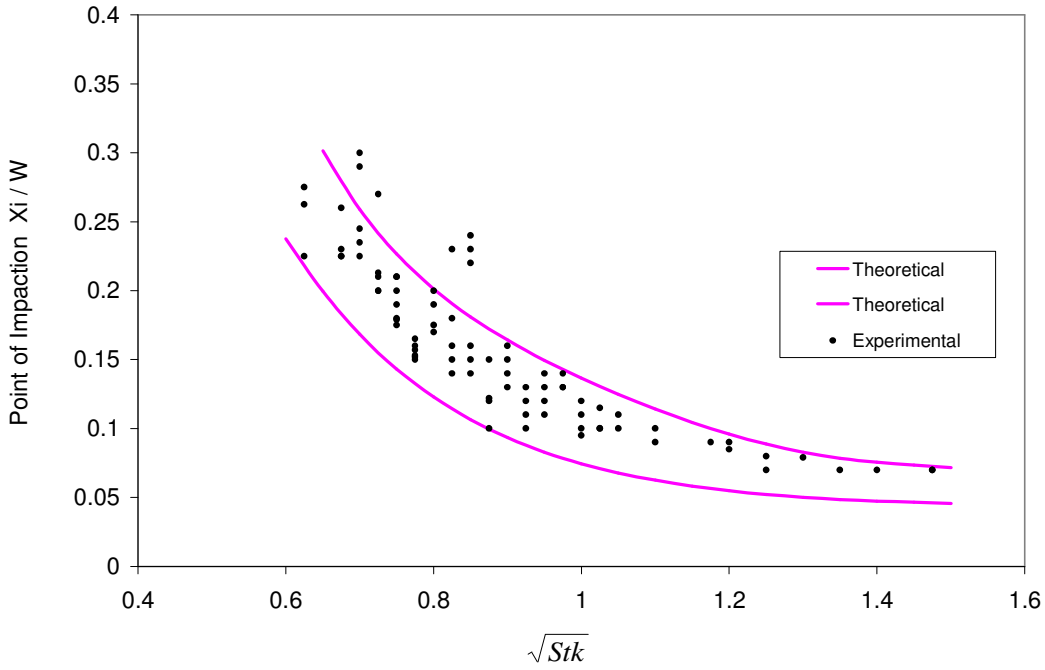

Figure 2.4 Comparison of theoretical and experimental impaction points in variable point impactor for Re=2000 and particle starting point at $Xc/W = 0.407$ (Marple and Liu, 1974).

The square root of the Stokes number is used on the x-axis as a measure of the dimensionless particle size. It should be noted that larger particles with a higher Stokes number impact closer to the center line, as expected by the theory. The shaded areas bounded by the two curves are the theoretically predicted areas of impaction. Finite areas

of impaction are predicted by the theory because of the finite size of the aerosol inlet tube.

The area between the two theoretical lines is the impaction region predicted by theory. The agreement between theoretical analysis and experimental data is good for the Xc/W ratios of 0.407.

2.6.3 Effect of Grid Size on Numerical Results

The choice of appropriate grid size for the diffuser model used in this study was evaluated by Gesler, (2000). In this work, the model of the bend generated for the study of particle deposition efficiency in ACE-Asia and NOAA inlets was meshed with different grid densities. The flow was solved and the flow field was determined. The optimum grid size was then achieved by reaching a solution which was independent of the grid density. In such a case, a finer grid would generate the same numerical results as the case with a lower density of grids.

The effect of grid size on numerical results of a simple geometry with sudden pipe contraction was investigated (Gesler, 2000). The experimental data on the same geometry was available (Durst and Loy, 1985). Four different grid densities were generated and the numerical results of velocity distribution along the pipe were compared with the experimental results of Durst and Loy, 1985.

To evaluate solution grid-dependency, all of the four separate cases of different grid densities were solved in Fluent and the velocity profiles at different measuring planes were plotted against the experimental results. The numerical results of velocity profile were improved by about 10% while the grid density was increased by 200%. The grid independent solution was achieved when the agreement between the numerical

results and the experiment reached 1%, on the highest grid density of the four calculated cases.

The grid size information for the diffuser and bend geometries are summarized in table 2.3.

Table 2.3 The grid size information for all the models used in this study.

Model	Cells	Faces	Nodes
Diffuser Internal Flow	20,560	41,505	20,946
Diffuser Total Flow	22,758	46,116	23,359
90° Bend	581,850	1,765,395	603,004
65° Bend	623,700	1,872,000	625,294

Chapter 3. Airborne Measurement of Aerodynamic Diameter of Coarse particles by Laser Doppler Velocimetry: Hardware

3.1 Introduction

This chapter focuses on the design of an instrument to determine the aerodynamic diameter of particles by measuring the particle velocity with a laser-Doppler velocimeter. The instrument functions by perturbing the flow and quantifying the particles response to flow perturbation. The ambient air from the atmosphere enters a diverging nozzle. Air slows down from the aircraft speed to about 5 ms^{-1} in a relatively short distance. The particles response to this velocity reduction is a direct function of their size and density. Smaller particles follow the air streamlines while the larger particles move forward and cross the air streamlines due to their inertia. The difference between the particle and gas velocity is primarily dependent on the aerodynamic diameter of the particles. Therefore, accurate measurement of velocity will lead to determination of aerodynamic diameter of the particles.

The geometry of the designed instrument is studied in detail in section 3.3. A low turbulence inlet (LTI) samples the air from the atmosphere and slows the flow using boundary layer suction through a porous diffuser. The slowing is accomplished in laminar flow. The reduction of turbulence in the inlet has two major benefits, it reduces the particle loss due to turbulent deposition of the particles on the inlet wall and it makes it possible to model the laminar flow in Fluent and calculate the flow field and particle trajectory accurately.

3.2 Laser-Doppler Velocimetry

Laser Doppler Velocimetry (LDV) is a well known technique that has been used to measure the velocity of particles for almost four decades. The particle velocity is determined by measuring the transit time of the particle across a known number of interference fringes. This section explains the components of a laser-Doppler velocimeter (LDV), description of the technique, determination of particle size from the velocity measurements and the effects of particle size, shape and density on velocity of a particle. The viewing volume and its effect on velocity measurement will be discussed as well.

3.2.1 Components of a Laser Doppler Velocimeter

A laser-Doppler velocimeter (LDV) comprises a light source (which is always a laser), optical arrangements to transmit and collect light, a photodetector and a signal processing arrangement.

The laser is a source of coherent light of appropriate intensity. The laser beam is split into two parts which cross to provide an interference pattern in the local region of the flow where velocity measurements are required. Part of the volume of interference is observed by a light collecting system and imaged on a photodetector. The photodetector converts the optical signal to an electronic signal which is processed by an appropriate signal processing arrangement.

Two intersecting light beams of equal intensity produce a pattern of fringes within their volume of intersection. The fringes are nearly parallel to the line which bisects the angle between the beams and perpendicular to the plane of the two beams. The fringe spacing, d_f, is given by:

$$d_f = \frac{\lambda}{2 \sin(\varphi)} \tag{3.1}$$

λ is the wavelength of the laser beam and φ is the half angle between the beams.

As each particle crosses the fringes, it scatters light and the intensity of the scattered light is modulated as the particle passes through the dark and bright fringes. The frequency of this modulation is directly proportional to the velocity of the particle in the direction perpendicular to the fringes. Radiation scattered from the particle is collected and focused onto a photodetector which measures the scattered intensity and responds quickly enough so that the frequency of modulation, called the Doppler frequency, can be detected. The velocity of the particles, V_p, perpendicular to the fringes equals:

$$V_p = f_D \, d_f \tag{3.2}$$

f_D is the Doppler frequency.

The utilization of the Doppler effect to measure the velocity of moving particles results in optical signals which show intensity variations and have frequencies which contain the required velocity information. A photodetector converts the optical signal into an electrical signal using a photoelectric mechanism. A photoelectric transition includes the conversion of the photon flux of the optical signal to an electron flux.

The light scattered from the particles has a sinusoidal intensity variation with time. The frequency of this variation is a function of the particle's velocity. Therefore, the information obtained from the frequency of intensity variations caused by the movement of particles through the intersection volume is used to determine the velocity of the particles. The fringe spacing is a function of the wavelength of incident beams and the angle between the beams, which are both fixed for a single configuration. Then the

only variable in determination of the particle velocity is the frequency of intensity variations.

In general, an increase in angle between the two beams results in a decrease of both signal strength and signal quality. A comparison of values for different sizes reveals that an optical arrangement, with a certain angle between the two incident light beams, may work satisfactorily for one particle size but can fail to produce good signals for another. Hence, the generally accepted assumption that an increase in particle size will result in an increase of signal strength and signal quality is not correct. Careful matching of fringe spacing and particle size is desirable to obtain optimum signals.

Figure 3.1 shows the schematic diagram of a laser-Doppler velocimeter for the measurement of particle velocity.

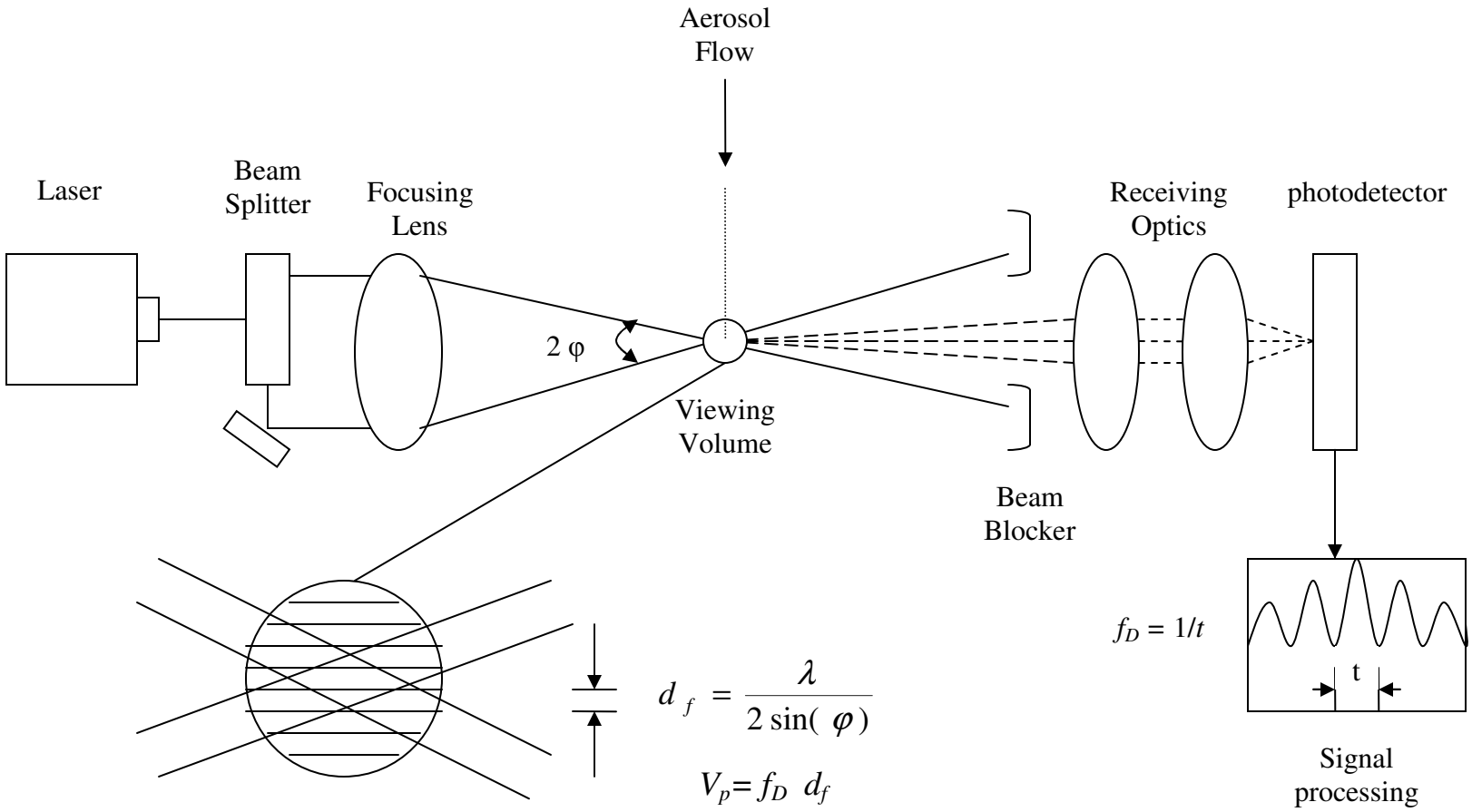

Figure 3.1 principles of Laser-Doppler velocimetry for the measurement of particle velocity.

The receiving optics are light-collecting lenses that are used to image the light scattered from the particles onto the photodetector. The beam blocker position controls the size of the measuring control volume, known as viewing volume. The size of the hole in front of the photodetector is given by:

$$d_{ph} = \frac{N_{ph} M \lambda}{2 \sin \varphi} \tag{3.3}$$

N_{ph} is the number of interference lines seen by the photodetector, M is the magnification by the lens and λ and φ are the wavelength of the incident beam and the angle between the two beams, respectively.

It is necessary to choose the optical components prior to the viewing volume to ensure that at least N_{ph} interference fringes are inside the viewing volume. The beam blockers control the solid angle over which light is contributing to the input signal to the photodetector. In general, the receiving optics should be positioned on the central axis of the optical arrangement to yield optimal signal-to-noise ratio.

The theory of laser-Doppler velocimeter signals consider the time dependence of beat signals resulting from interference between two scattered light waves. These considerations yield the relationship between the measured signal frequency and the velocity of the particles as a function of the optical geometry and the wavelength of the incident light beam.

The signal-processing systems yielding laser-Doppler information in frequency domain are, in general, amplitude sensitive and hence the final information is dependent on the duration of laser-Doppler signals.

The signals from a laser-Doppler velocimeter are characterized by both amplitude and frequency modulation. The amplitude modulation results from scattering by particles of non-uniform size crossing regions illuminated by non-uniform light intensity, whereas the frequency modulation carries the required information on the velocity of each of the moving particles.

3.2.2 The Sources of Error in Laser-Doppler Velocimetry

The first source of error initiates from unequal fringe spacing, which results in different frequency measurements for particles of the same velocity. The optical system design should consider the Gaussian characteristics of the laser beams. The optics should be aligned property to ensure the equal fringe spacing in the viewing volume.

Another source of error arises from the variation of velocity across the viewing volume. Different Doppler frequencies are measured if there is a strong velocity fluctuation due to spatial velocity differences and these have to be minimized by matching the optical system to the existing velocity gradients. If matching does not reduce gradient-imposed velocity fluctuations to an acceptable level, then the final data have to be corrected.

The effects of sound fields and temperature gradients on particle motion should be taken into account. The influence of gradients in particle concentration may also necessitate careful optical design and possible corrections.

In addition to these optical errors, which can be minimized or even eliminated by proper optical design, there are also effects of the electronic system which have to be understood to allow systems optimization and data correction.

3.2.3 Measurement of Particle Concentration from Frequency Signals

Particle concentration at the measuring volume of the LDV can be determined by knowing the number of particles instantaneously in viewing volume, and the volume of the viewing volume itself.

Figure 3.2 shows the transit time of individual particles A, B and C in the viewing volume, as τ_A, τ_B and τ_C respectively.

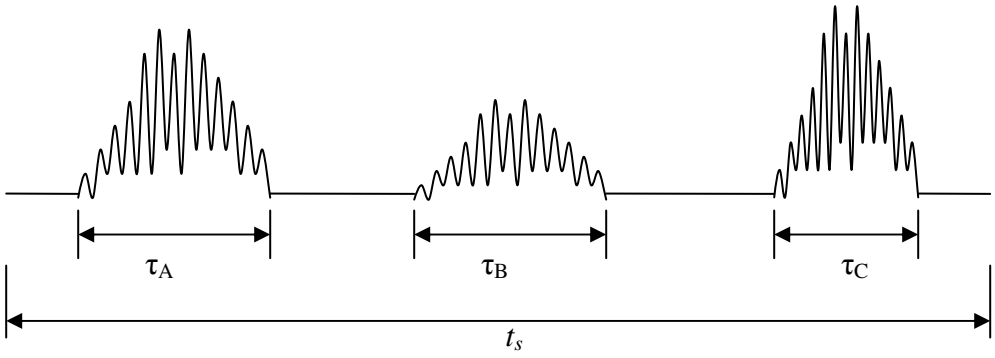

Figure 3.2 Determination of particle concentration from frequency signals.

The fraction of the total time t_s for which particles are present in the measuring volume can be found from $\sum \tau_{k/} t_s$ provided the range of times τ_k, the transit time of individual particles, does not vary significantly. This ratio is also the fraction of time n for which particles are present in the scattering region whose volume V is calculated from the optical characteristics of the system.

$$N \approx \frac{n}{V} \tag{3.4}$$

The particle concentration N (number of particles per unit volume of air) is then found from n / V, which is the ratio of the number of particles to the total volume of the control volume. The estimate of particle concentration by this method is valid only when

there is less than one particle on average in the scattering volume at any time and also, when the transit time of individual particles is not too variable.

$$n = \frac{\Sigma \tau_k}{t_s} \tag{3.5}$$

n is the number of particles simultaneously in control volume, τ_k is the transit time of individual particles, t_s is the total time for which particles are present in the viewing volume, V is the volume of the control volume and N is the particle concentration.

3.2.4 Determination of Aerodynamic Diameter of Particles from Velocity Measurements

The signal from LDV can provide information about the size and number density of the aerosol particles. The determination of number concentration of particles has been described in the previous section. Measurement of particle size from LDV signals has the advantage that the method is independent of refractive index, a property which may be unknown in many aerosols.

The visibility of LDV signal and the known fringe spacing can be used to estimate the particle diameter. In general, visibility of light scattering signals decreases as diameter of the particle becomes large relative to fringe spacing. A typical velocimeter geometry with $\varphi = 9°$ and $\lambda = 633$ nm has a fringe spacing of 2 μm. Therefore, a particle larger than 2 μm in diameter loses its visibility as a function of its size.

As mentioned earlier, the diameter of a spherical particle with known density can be determined from particle velocity. In most aerosol investigations, the shape and density of particles are not known. In such cases, an aerodynamic diameter is determined from the particle velocity.

The aerodynamic diameter of a particle is defined as the diameter of a unit density spherical particle having the same settling velocity and Stokes number as the particle in question under the same flow conditions and geometry. Therefore, particles with the same aerodynamic diameter have the same trajectory in a known flow condition and geometry.

The Stokes number of a particle is given by:

$$Stk = \frac{\rho_p D_p^2 V_g C(D_p)}{9 \mu d} \tag{3.6}$$

ρ_p is the particle density, D_p is the particle diameter, V_g the gas velocity, C is the slip correction factor and μ and d are the dynamic viscosity of air and diameter of the diffuser at the measurement point respectively.

Based on the definition of the aerodynamic diameter of a particle, the Stokes number can be written as:

$$Stk = \frac{D_a^2 V_g C(D_a)}{9 \mu d} \tag{3.7}$$

D_a, the aerodynamic diameter of the particle, in Equation (3.7) is then replaced by $\rho_p D^2_p$ in (3.6).

$$\sqrt{C(D_a)} D_a = \sqrt{C(D_p)\rho_p}\, D_p \tag{3.8}$$

Knowing the aerodynamic diameter of a particle, the actual diameter of a spherical particle is determined by estimating its density.

The aerodynamic diameter of a particle is determined from Equation (3.9):

$$\sqrt{C(D_a)}\, D_a = \sqrt{\frac{Stk\ (9 \mu d)}{V_g}} \tag{3.9}$$

3.3 A device for slowing the flow: the Low Turbulence Inlet

3.3.1 Introduction

Sampling of aerosols from aircraft is difficult primarily because of large differences between the aircraft speed and the speed of the aerosol measurement instruments, which typically accept airspeeds on the order of 1 to 10 m/s.

For a variety of reasons, such as transmitting particles around bends, the flow in an inlet taking air to aerosol instrumentation must be slower than the aircraft speed. Decelerating flows are prone to turbulence and loss of particles (Murphy et. al, 2004). Turbulence generated in an inlet makes it difficult to know the relationship between the measured aerosol size distribution and that existing in the ambient air prior to sampling.

In some cases most of the aerosol mass is deposited on the walls of the inlet rather than transmitted to instrumentation inside the airplane (Huebert et. al, 1990).

Reduction of turbulence makes it possible to model and solve the flows inside the inlets and calculate the particle trajectories using computational modeling tools

The velocity reduction is achieved by sampling the ambient air into a conical diffuser, which is part of a low turbulence inlet developed at University of Denver. The conical diffusers reduce the flow velocity proportional to the ratio of the diffuser entrance area to exit area. The low turbulence inlet (LTI) uses the boundary layer suction through a porous medium to remove the generated turbulence as a result of the area expansion in the diffuser.

The porous diffuser walls act as a momentum sink and therefore, the boundary layer can not develop enough to obtain the adverse pressure gradient required to cause separation and turbulence. The experiments incorporating boundary layer suction (BLS)

along internal porous diffuser walls have reduced turbulence intensities fro 24%-30% to less than 1% at the diffuser exit, thus laminarizing the internal expanded flow.

3.3.2 Components of a Low Turbulence Inlet

A low turbulence inlet (LTI) is comprised of a conical diffuser, porous medium, suction and core flow channels, Differential pressure transducers and a suction pump. The conical diffuser is a converging nozzle with an area ratio of 25. Figure 3.3 shows the details of an LTI used in this work.

Air enters the inlet at true air speed of the airplane under isokinetic sampling conditions. The velocity of airplane is in the order of 200 ms^{-1}. The conical diffuser of the inlet reduces the air velocity at a rate which is proportional to the area ratio of the inlet. The expansion of air and separation of flow generates high turbulence. Particles are lost due to the turbulent deposition to the diffuser wall, which in turn, may alter the size distribution of the sampled aerosol.

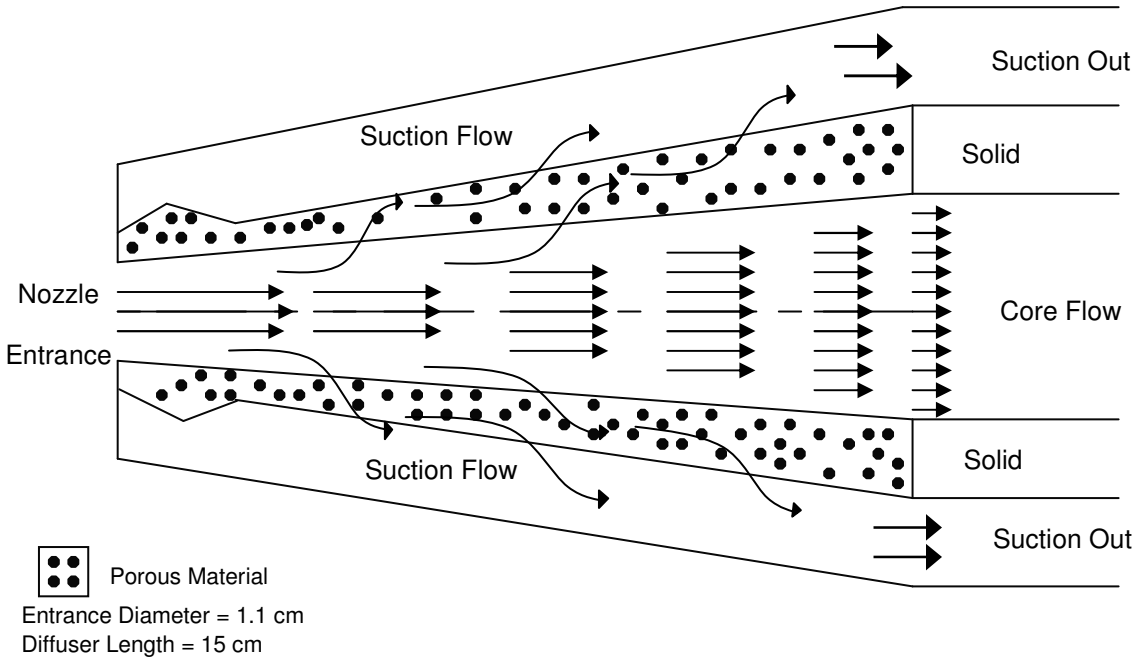

Figure 3.3 Diagram of a Low Turbulence Inlet (Maryam Darbeheshti, 2008).

The reduction of turbulence is achieved by removal of about 80% of the boundary layer air through the porous medium into the suction flow.

Porous media is a flow resistance. It is an added momentum sink in governing equation. The momentum sink contributes to the pressure gradient in porous cell, creating a pressure drop that is proportional to v^2. The volume blockage that is physically present in the porous diffuser is not represented in the model. Therefore, Fluent uses and reports a superficial velocity inside the porous medium, based on the volumetric flow rate, to ensure continuity of velocity vector across the porous medium interface.

The use of true physical velocity is also available by Equation (3.10).

$$V_{superficial} = \gamma\, V_{physical} \tag{3.10}$$

γ is the porosity of the porous medium, which is the ratio of the volume of the medium that is occupied by the fluid to its total volume (in this case, 0.2).

The viscous losses in porous medium are given by Darcy's law:

$$\nabla P = -\frac{\mu}{\alpha} V \tag{3.11}$$

$1/\alpha$ is the coefficient of permeability = 1.74×10^{11} $1/m^2$. Therefore the viscous losses in x and y-directions are:

$$\Delta P_x = \sum_{j=1}^{3} \frac{\mu}{\alpha x_j} V_j \, \Delta n_x \tag{3.12}$$

$$\Delta P_y = \sum_{j=1}^{3} \frac{\mu}{\alpha y_j} V_j \, \Delta n_y \tag{3.13}$$

Δn is the thickness of the porous medium.

The inertial losses in porous medium are given by:

$$\nabla P \approx -\sum_{j=1}^{3} C_{2ij} \left(\frac{1}{2} \rho V_j V_{mag}\right) \tag{3.14}$$

C_2 is the inertial resistance factor = 2.89×10^6 1/m. Therefore, the inertial losses in x and y-directions are:

$$\Delta P_x \approx \sum_{j=1}^{3} C_{2xj} \, \Delta n_x \left(\frac{1}{2} \rho V_j V_{mag}\right) \tag{3.15}$$

$$\Delta P_y \approx \sum_{j=1}^{3} C_{2yj} \, \Delta n_y \left(\frac{1}{2} \rho V_j V_{mag}\right) \tag{3.16}$$

3.3.3 Turbulence and its Effect on LTI Performance

3.3.3.1 Generation of Turbulence

As mentioned earlier, the turbulence generation is a major flow issue for aerosol inlets using conical diffusers. The boundary layer growth, transition and separation are the main causes of turbulence generation. At some distance from the leading edge of the diffuser, the turbulence patches form and grow to generate a turbulent boundary layer.

In converging diffusers, the adverse pressure gradient in the flow (increasing pressure in the flow direction) accelerates the transition process from a laminar to turbulent boundary layer. Increasing adverse pressure gradient causes the velocity at a given height from the wall to decrease with distance along the wall. Larger pressure gradients cause the flow to separate from the surface producing a region of reversed flow between the edge of the boundary layer and the wall. The flow separation causes more turbulence in the flow. If a sufficient length straight duct is attached to the exit of the diffuser, the separated flow reattaches to the surface. The velocity at the centerline remains higher than that predicted by one-dimensional ideal flow calculations, while the velocity near the wall is lower than the ideal flow (Seebaugh, 1991).

Diffusers typically used for aerosol sampling from aircraft have near uniform velocity profile at the entrance. They also have the highest pressure gradient at the entrance, which increases with increasing entrance velocity and expansion angle. The pressure gradient decreases with increasing entrance diameter of the diffuser. Therefore, diffusers for aerosol sampling from aircraft have high adverse pressure gradients due to high entrance airspeeds and small entrance diameters.

The generated turbulence in the diffusers is responsible for the deposition of super-micron particles on the diffuser walls. At some instances, the deposition of nearly 50% of the mass of the aerosol particles on the walls of the inlets has been reported (Huebert et. al, 1990).

3.3.3.2 Elimination of Turbulence

The removal of a fraction of air at the boundary layer, known as boundary layer suction (BLS), eliminates the generated turbulence by removing the flow disturbances through a porous medium. Removing flow disturbances suppresses the growth of the turbulent patches, which are partially responsible for initiating the transition process. The suction flow passes through the porous wall of the diffuser. The exit diameter of the porous diffuser is 0.0267 m. The porous medium is a 20 μm stainless steel. The amount of suction is determined by the volume of the boundary layer. It may not be necessary to remove the entire boundary layer flow to inhibit turbulence generation.

The elimination of turbulence reduces the losses of super-micron particles by turbulent deposition and permits the use of laminar flow calculations in numerical modeling to accurately predict particle trajectory along the diffuser. The rate of turbulent deposition depends on particle size and bigger particles typically suffer larger losses.

Chapter 4. Airborne Measurement of Aerodynamic Diameter of Coarse particles: Numerical Analysis of the Instrument

4.1 Introduction

The numerical analysis of the instrument is discussed in this chapter. A low turbulence porous diffuser is modeled in Fluent. Super micron particles in the size range of 1 to 30 micron enter the diffuser and the particle trajectories are calculated. Two different inlets, used in ACE-Asia and PELTI field programs, are modeled with different leading edge geometries.

A total of seven cases have been studied at five different altitudes and six different true air speeds of the aircraft. The ambient pressure varies in the range of 400 to 900 mb, corresponding to altitudes from 1 to 8 km above the sea level.

In each case, the velocity of the particles are calculated for the measurement points along the diffuser path in 2cm intervals in order to find the best measuring spot that would demonstrate the highest velocity gradient in the size range of the interest.

Based on the analysis of the velocity variations, the sensing volume of LDV is located at a distance of 2.16 cm from the entrance to the diffuser.

The flow of air into the diffuser is sub-isokinetic, which refers to an entrance air speed that is lower than the aircraft true air speed. The isokinetic ratio is determined for each case as the ratio of the true air speed of the aircraft to the velocity of the air at the entrance to the inlet.

4.2 Determination of the Measurement point

In order to choose the best measuring point along the flow path, the velocity of particles is calculated for several locations with approximately 2 cm intervals. The flow conditions, inlet geometry, true air speed, and particle characteristics are kept constant throughout the measurement. Figure 4.1 shows the velocity of particles as a function of particle size for 1-100 μm particles at x=2, 4, 6, 8, 10 and 12 cm from the entrance to the inlet.

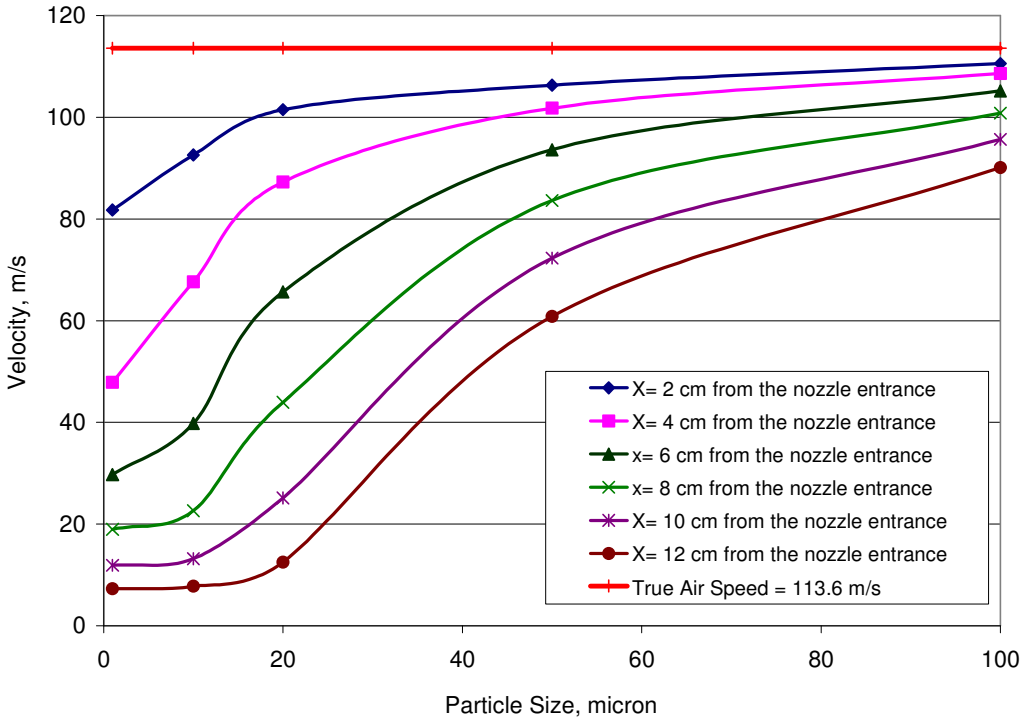

Figure 4.1 Particle velocities as a function of particle size for various x-coordinates along the diffuser.

The above figure covers the range of particles beyond the interested range of particles for this work. It provides a bigger picture of the particle trajectory for particles

as large as 100 μm. For further analysis, only the particles in 1-30 μm range have been considered.

As it is evident from the graph, smaller particles show a great velocity reduction at the beginning of the diffuser. Measurements at x=2 and x=4 cm have the highest velocity gradient in particles 1-30 μm. As the measurement point moves towards the end of the diffuser, the velocity gradient for smaller particles diminishes, and instead, the larger particles have a better chance of being detected.

The sensing volume of the laser-Doppler velocimeter is located at 2.16 cm from the entrance. Although this point could have moved a little further into the flow to get a better velocity gradient for the lower end of the size spectrum (Figure 4.1), the fact that the smaller particles are sucked out of the flow at a much higher rate than the larger particles was an important factor to keep the measuring point as close to the entrance of the inlet as possible.

Figure 4.2 shows the velocity of particles with the diameters of 1, 10 and 20 μm as a function of the measuring point along the diffuser. The trajectory of 1-micron particles is the same as the gas velocity, since the smaller particles follow the flow streamlines. A 10-micron particle travels 14% faster than a 1-micron particle at x=2 cm from the entrance and a 20-micron particle moves 25% faster than a 1-micron particle at the same measurement point.

A typical laser-Doppler velocimeter has an accuracy of 0.1-0.2% with a resolution of 0.3%. Therefore, it will be well-suited for the velocity measurements and the accuracy requirements to distinguish particles in the size range of 1-30 μm.

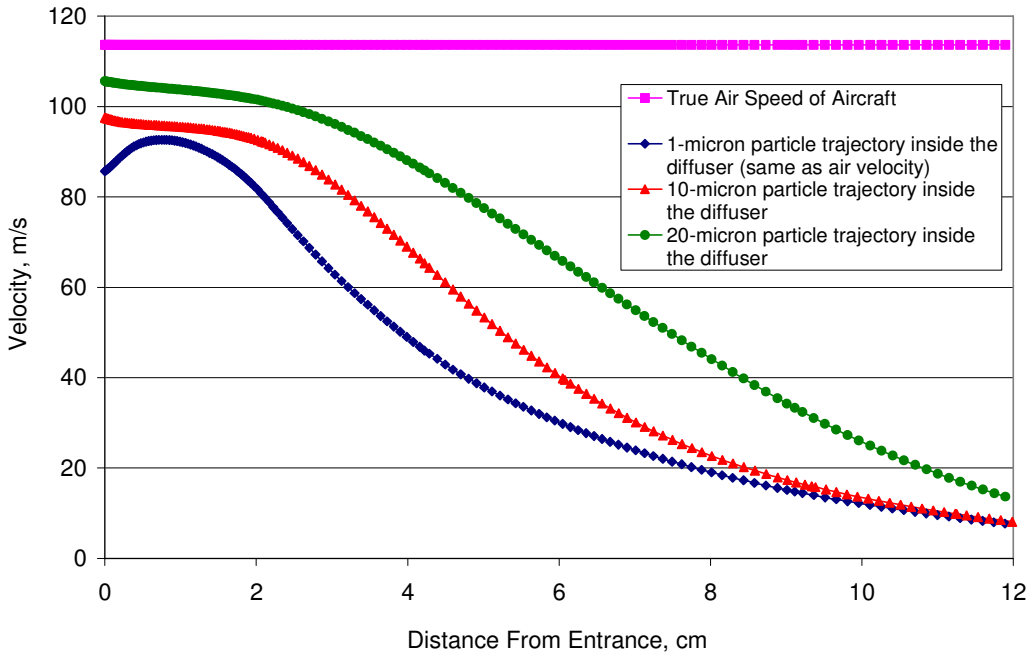

Figure 4.2 Comparison of particle velocity as a function of particle distance from entrance and true air speed of the aircraft.

The data in Figure 4.2 are the result of Fluent simulations on ACE-Asia LTI at an altitude of 5 km, with a true air speed of 113.6 ms^{-1}. The flow of air at entrance to the inlet is sub-isokinetic. The isokinetic ratio of the flow is about 0.76. In other words, there is a reduction of 24% to the air velocity right before it enters the diffuser. There are several factors that contribute to this velocity reduction at the diffuser entrance. The presence of the stagnation area in front of the nozzle disturbs the flow streamlines before they enter the inlet. The misalignment of the inlet with the direction of the wind may also cause the flow to divert and loose its velocity.

Figure 4.3 shows the measurement point, where the viewing volume of LDV is located. The trajectory shown is for 10 μm particles passing through the diffuser.

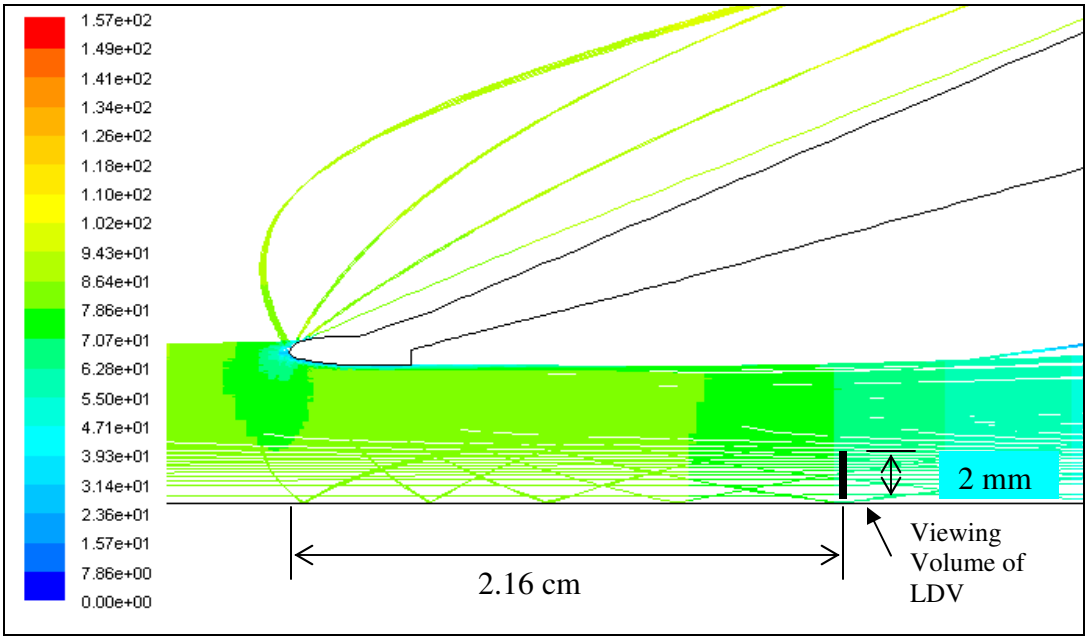

Figure 4.3 Location of measuring point (LDV viewing volume) from inlet entrance.

4.3 Modeling Two Different Geometries

As mentioned earlier, the velocity of particles is a function of particle size, shape, density, flow conditions and inlet geometry. The effect of inlet geometry on particle trajectory is discussed in this section. Diffusers of two different geometries have been modeled in Fluent keeping all other factors constant. Particles in the size range of 1-30 micron are injected to the flow and particle trajectories are compared to analyze the effect of inlet geometry on particle velocity.

4.3.1 LTI used in PELTI Experiments

The LTI used in PELTI experiments is shown in Figure 4.4. The flow around and inside the inlet is modeled in Total flow. PELTI field experiments have been conducted under different environments, from an altitude of about 700 m to 6 km above the sea level. The aircraft true air speeds have been modeled in the range of 115 to 155 ms^{-1}. The flow of air at the inlet entrance is sub-isokinetic for all the cases studied. The isokinetic ratio of the flow varies from 0.75 to 0.9.

A 2-D geometry that covers 0.5 m prior to the inlet leading edge is created in Gambit and imported to Fluent. The inlet is 26 cm long. The diverging area of the nozzle is 15 cm followed by 11 cm of straight section that separates the core flow from the suction flow.

The difference in the inlet leading edges of the two inlets is apparent by comparing Figures 4.4 and 4.5. The elliptical shape of both of the leading edges helps with the maintenance of laminar flow throughout the diffuser. The sharp-edged inlets have shown to initiate separation of flow and generation of more turbulence at the entrance to the inlet.

The vertical lines in Figures 4.4 and 4.5 are provided for scaling purposes. Each interval is about 1.3 cm wide in the x-direction.

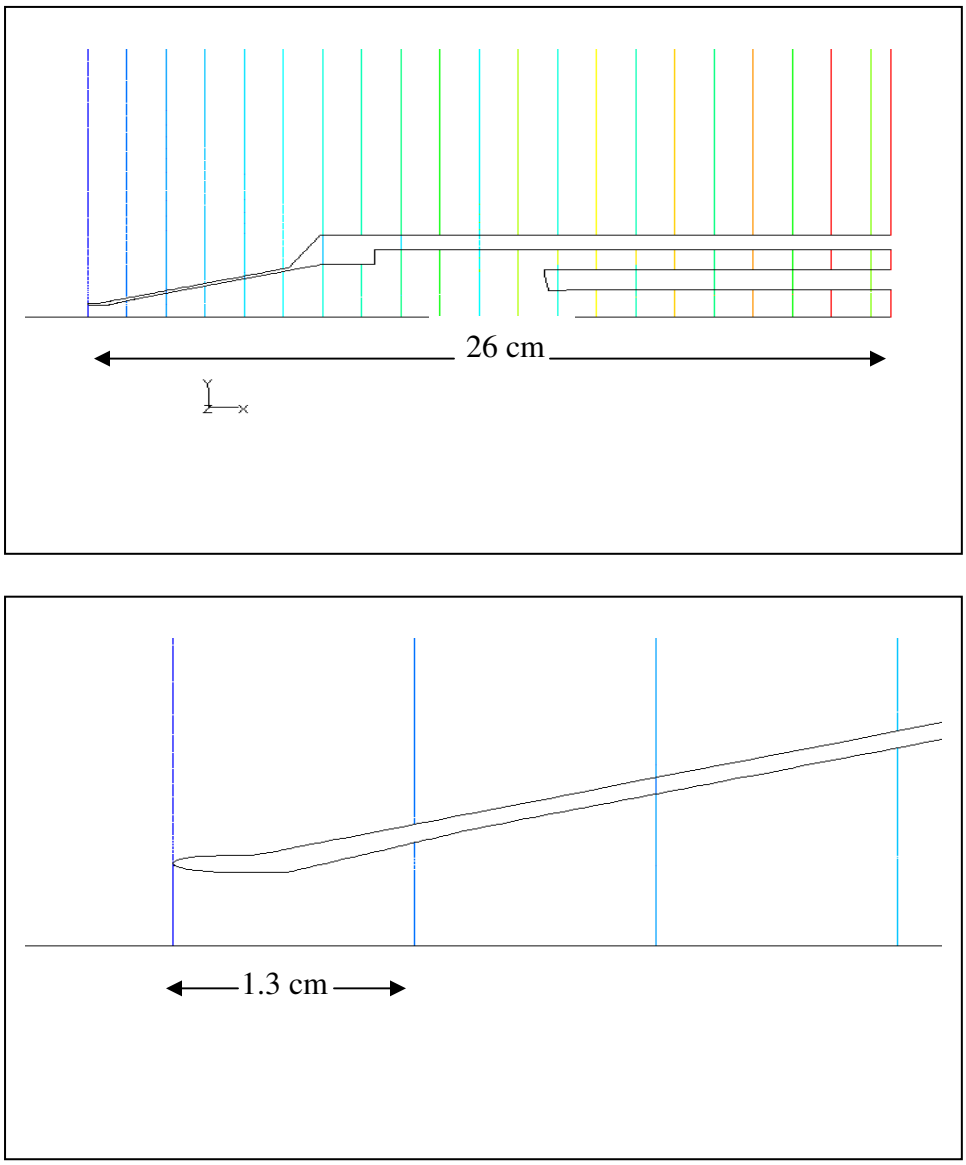

Figure 4.4 LTI used in PELTI experiment, complete view (up), leading edge (down).

4.2.2 LTI used in Ace-Asia Mission

The ACE-Asia LTI is shown in Figure 4.5. The flow around and inside the inlet is modeled in Total flow. A 2-D geometry that covers 0.5 m prior to the inlet leading edge is created in Gambit and imported to Fluent.

The inlet is 50 cm long; with 15 cm of the diverging nozzle and 35 cm of the straight section that divides the core flow from the suction flow.

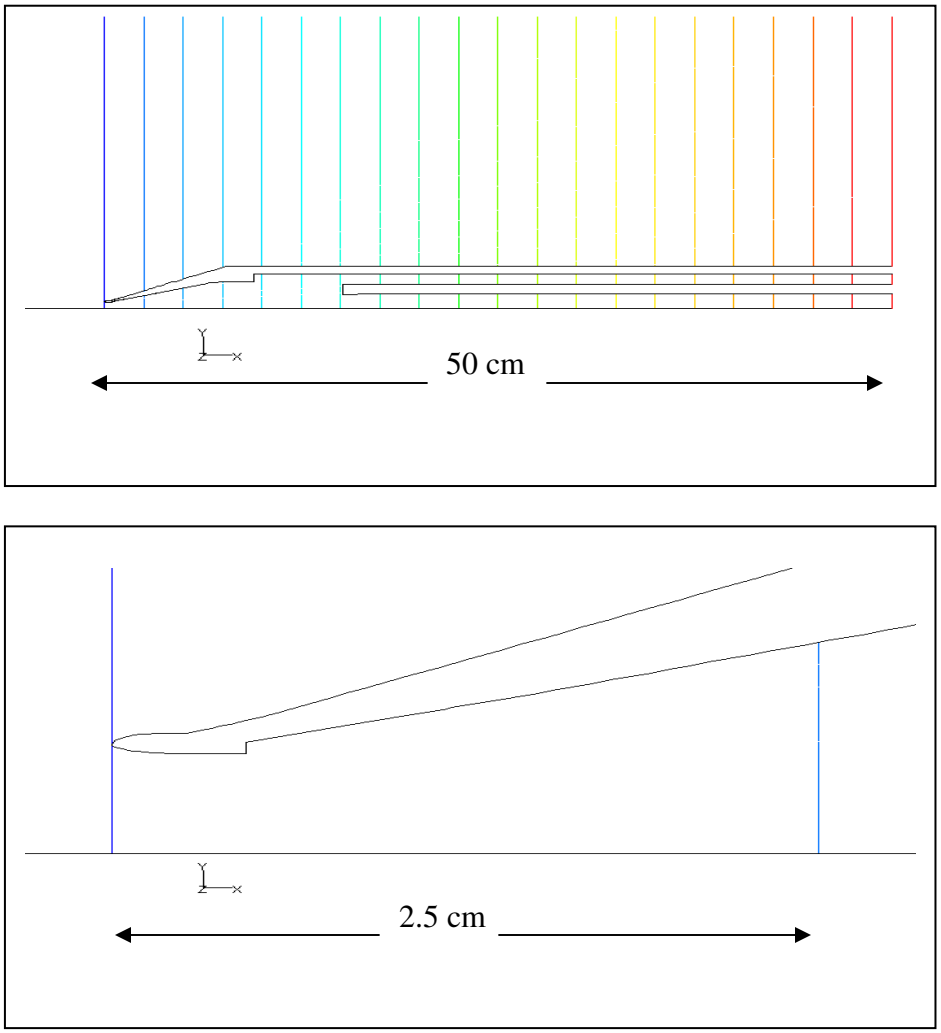

Figure 4.5 LTI used in ACE-Asia experiment, complete view (up), leading edge (down).

The ACE-Asia inlet is analyzed under two ambient pressures of 53,000 and 86,400 Pa which corresponds to altitudes of 5 and 1.3 km from the sea level respectively.

4.4 Modeling Different Conditions

The impact of sampling particles at different altitudes and aircraft speeds on trajectory of particles has been evaluated in proceeding sections.

4.4.1 Effect of Altitude on Particle Trajectories

The two LTI geometries have been tested at five altitudes from 1-8 km to determine the effect of altitude on particle trajectories.

Particles 1-30 μm are injected to the air flow and the particle velocity is plotted as a function of particle size at different altitudes, keeping all the other determining factors constant. Figure 4.6 illustrates the results of sampling air at the same air speed but flying at different altitudes. The two ambient pressures of 86,168 and 74,920 Pa in the graph correspond to the altitudes of 1.3 km and 2.5 km from the sea level respectively. The 1.2 km increase in altitude reduces the ambient pressure by about 15%. As a result, the air inside the diffuser slows at a faster rate and the smaller particles follow the air pattern and therefore, move at a relatively smaller velocity compared to the same size particles moving at a flow with higher velocity.

It should be mentioned that all the above velocity measurements are calculated at a fixed measuring point of 2.16 cm from the diffuser entrance.

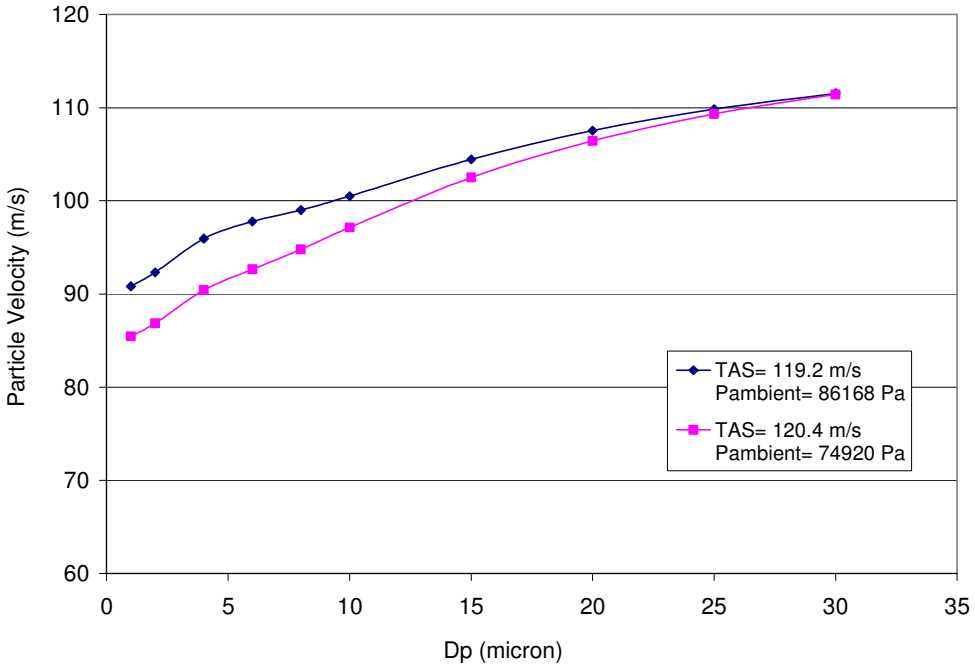

Figure 4.6 Particle velocity as a function of particle size at same aircraft speed, and different altitudes.

4.4.2 Sampling at Different Aircraft Speeds

The aircraft speeds in the range of 113.6 to 154.6 ms^{-1} have been evaluated to determine the effect of true air speed (TAS) on the velocity of particles in the size range of 1-30 µm. Figure 4.7 shows the results of sampling air at the altitude of about 5 km, but from two aircraft with a 20% difference in their speed.

In general, the velocity of the particles is directly proportional to the particle size. Flow velocity is reduced inside the diffuser. The smaller particles follow the streamlines and reduce their speed accordingly. Bigger particles are able to cross the streamlines due to their inertia, and therefore move at a higher speed as compared to the velocity of air. The bigger the particle, the higher would be the velocity gradient between the air and the

particle. It should be mentioned that for any specific particle size, the velocity increases as the aircraft speed increases.

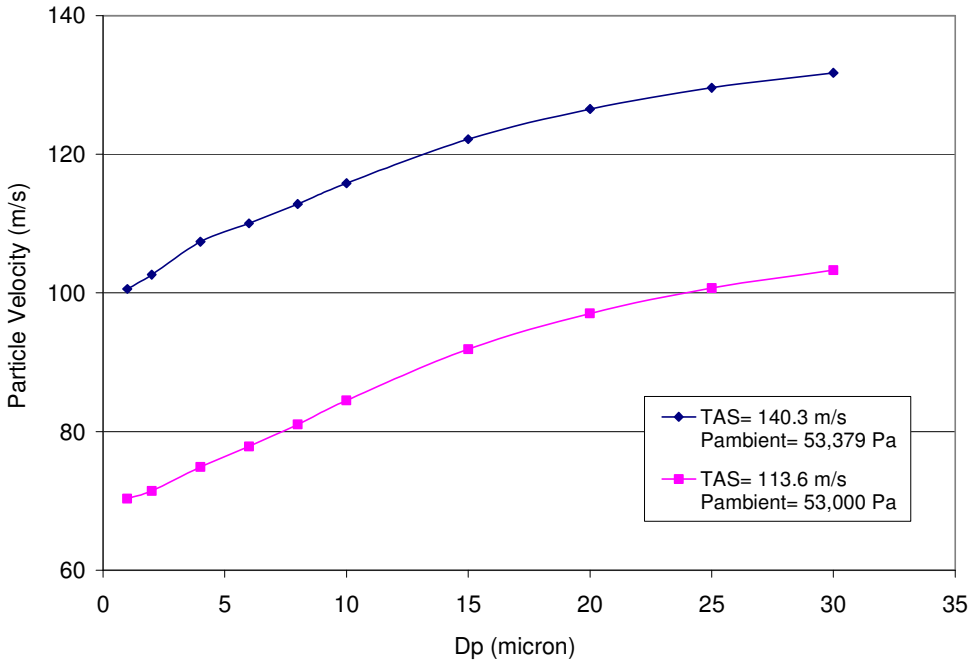

Figure 4.7 The effect of particle size on particles velocity at the same altitude and two different aircraft true air speeds.

4.5 Particle Behavior upon Impact with the Surface of Inlet Leading Edge

When a particle strikes a surface, there is a complex system of plastic and elastic deformation as the surface absorbs the force imparted by the particle. The knowledge of the important energy loss mechanisms is required to quantify the effect of particle behavior upon impact with a surface. The three major energy loss mechanisms are plastic deformation, generation of new surfaces and surface roughness (Tsai et. al, 1990). In the absence of these energy loss mechanisms, the particles would rebound with the same velocity as of the incident velocity of the particles. This is referred to the elastic collision.

In elastic collision the particle's incident velocity is conserved and the coefficient of restitution is equal to 1. Coefficient of restitution is defined as the ratio of the rebound velocity to the incident velocity of particles. Surface roughness is an important aspect of any impaction analysis. The surface of the leading edge of the inlet and the surface of particles striking the leading edge are assumed to be perfectly smooth in this work.

4.5.1 Theory of particle Bounce

Particle bounce has been a subject of considerable interest to aerosol researchers. Particles with inertia greater than a certain value often bounce upon impact with the solid surfaces (Tsai et. al, 1990).

The principles which govern the mechanics of particle bounce are quite complex. If particles are able to deform to absorb the impact force, they will be less likely to bounce. In general, liquids have greater capacity than solids to plastically/elastically deform in order to absorb the impact forces.

There are classically two approaches to describe particle bounce. The first defines a critical velocity V_c, above which bounce will occur, of the form (Cheng and Yeh, 1979; Brown, 1993):

$$V_C = \frac{\beta}{D_p} = \frac{1}{D_p} \frac{(1-e_{Pl}^2)^{1/2}}{e_{Pl}^2} \frac{A}{\pi x^2 (6P_{Pl}\rho_p)^{1/2}} \tag{4.1}$$

β is a constant for a particular impaction surface, D_p the particle diameter, e_{pl} is the coefficient of restitution (for plastic deformation only), A the Hamaker constant, p_{pl} the microscopic yield pressure, ρ_p the particle density and x is the separation distance of the particle mass center and surface. Hamaker constants are given in the literature for a limited number of elements.

The other method involves the kinetic energy, KE_b, required for bounce to occur when a particle collides with a surface (Dahneke 1971):

$$KE_b = \frac{D_P A(1-e^2)}{2xe^2} \tag{4.2}$$

Coefficient of restitution, e, is the ratio of rebound velocity to incident velocity (for both plastic and elastic deformation).

A and e depend only on the material of the particle and the impaction surface. It is reported that these constants must be determined experimentally, as it is very difficult to determine them theoretically (Mullins et. al, 2003).

Also, the spherical particles are much more likely to bounce than irregular particles (Brown 1993). Some experimental results of irregularly shaped fly ash particles (mean diameter 0.14 μm) give the probability of bounce as (Ellenbecker et. al, 1980):

$$P_b = 1 - 0.000224\ (KE)^{-0.233} \tag{4.4}$$

P_b is the probability of bounce and KE is the kinetic energy in Joules.

The kinetic energy of the particle may be distributed in several processes. Part of it may be retained in bouncing particles, or used to create new surfaces during breakup.

4.5.2 Elastic Collision of particles with Inlet Leading Edge

Considering the elastic collision of particles with the inlet leading edge, particles impact the surface of the leading edge at different angles and bounce off the surface in different directions. Since it is an elastic collision, particles will keep all their kinetic energy and move in a new direction with the same incident velocity. The elastic collision changes the direction of particle trajectory inside the diffuser and therefore, the x-y components of their velocity changes.

120 unit density particles distributed over the constant area are injected to ACE-Asia inlet and the particle trajectories are recorded. Table 4.1 shows the overall picture of particle trajectories in 1-100 μm size range.

Table 4.1 Trajectory of 120 unit density particles injected to ACE-Asia inlet, at TAS=113.6 ms^{-1}, ambient pressure= 53,000 Pa, altitude=5 km.

Dp (μm)	# Tracked	# escaped		# Trapped	# Hit leading edge		# Hit the axis	
		Left domain	Entered Core		Left domain	Entered domain	Left domain	Entered domain
1	120	43	5	72	4	4	0	0
2	120	38	5	76	5	8	0	0
3	120	34	5	80	8	11	0	0
4	120	30	6	84	10	13	0	0
5	120	27	6	86	12	16	0	0
6	120	24	11	85	14	17	0	0
7	120	21	19	79	15	18	0	4
8	120	19	18	82	16	19	0	10
9	120	17	15	85	17	18	0	12
10	120	16	15	87	16	17	0	13
11	120	14	16	89	14	18	0	15
12	120	13	16	80	13	18	0	15
13	120	12	19	88	12	18	0	16
14	120	11	24	84	11	18	0	11
15	120	10	20	88	10	19	0	17
16	120	14	23	81	9	19	5	14
17	120	13	24	79	9	18	4	13
18	120	13	29	75	8	19	5	13
19	120	12	35	72	8	18	4	13
20	120	12	39	67	7	19	5	14
21	120	11	46	61	7	19	4	14
22	120	11	54	54	6	19	5	14
23	120	11	64	43	6	19	5	14
25	120	10	90	18	5	19	5	14
27	120	10	97	13	5	19	5	13
28	120	9	97	14	5	19	4	15
29	120	9	98	13	5	19	4	15
30	120	9	98	13	4	19	5	14
31	120	9	98	13	4	19	5	14
32	120	8	98	13	4	19	4	15
33	120	8	98	14	4	19	4	15
34	120	8	98	14	4	19	4	15
35	120	8	98	14	4	19	4	15
40	120	8	99	13	3	19	5	14
45	120	7	99	14	3	19	5	14
50	120	7	100	13	2	20	5	15
55	120	7	100	13	2	19	5	14
60	120	7	100	13	2	19	5	14
65	120	6	100	14	2	19	4	15
70	120	6	100	14	2	19	4	15
75	120	6	100	14	1	20	5	15
80	120	6	100	14	1	20	5	15
85	120	6	101	13	1	20	5	15
90	120	6	101	13	1	20	5	15
95	120	6	101	13	1	20	5	15
100	120	6	100	14	1	20	5	15

As shown in the table, smaller particles are either trapped in the porous diffuser and suctioned out of the flow or follow the diverted air streamlines and leave the calculation domain before entering the diffuser. On the other hand, particles with higher inertia tend to remain in the flow and end up in the sample core flow. Also, the number of particles that hit the leading edge of the inlet and rebounded back to the flow with lower axial velocity increases with particle size. The velocity of particles is recorded by LDV which is located approximately 2 cm from the diffuser entrance, and extended 4 mm from the center of the flow towards the porous diffuser.

The numbers of particles that enter the sensing volume of LDV per second with a velocity within a specified range are recorded by a particle counter. Therefore, each velocity channel will show the number of particles that have entered the sensing volume of LDV with a known velocity that is defined by each channel. These particles may include all the particles that entered the flow without being diverted by hitting the leading edge of the inlet along with all those particles that hit the leading edge and bounced off to enter the flow at a lower velocity.

The trajectory of particles and their path after hitting the leading edge is shown in Figures 4.8 through 4.10, for particle with Dp=1, 5, 10, 20 and 30 micron. Figure 4.8 shows the trajectory of 120 particles all the way through the diverging part of the inlet. As the diameter of particles increases, less particles are removed from the flow through the suction and more particles end up in the core flow, which explains the increase in the mixing ratio of particles as the particle size increases. Figures 4.9 and 4.10 demonstrate a close-up look at the entrance to the inlet, where particles enter the flow either directly or after striking the leading edge of the inlet.

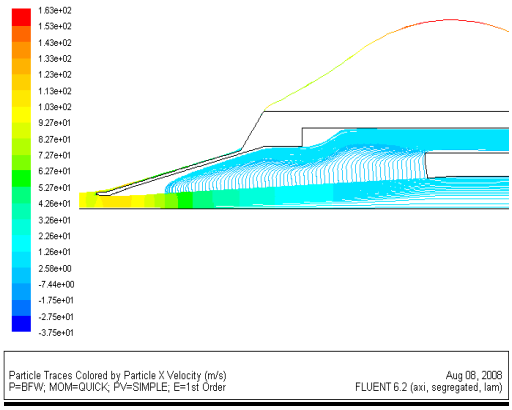

D_p=1 micron

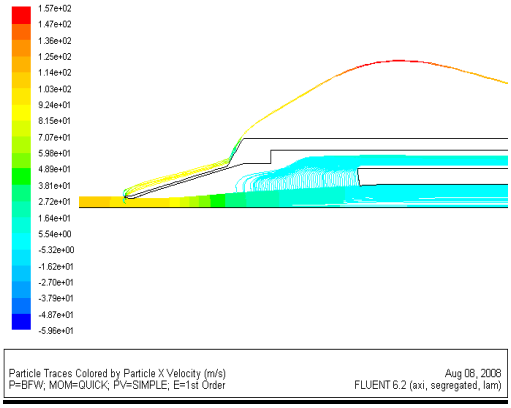

D_p=6 micron

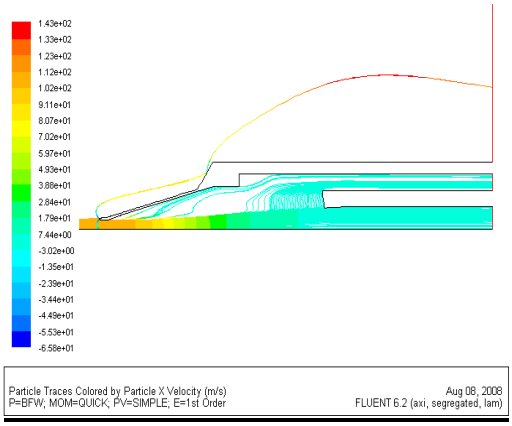

D_p=10 micron

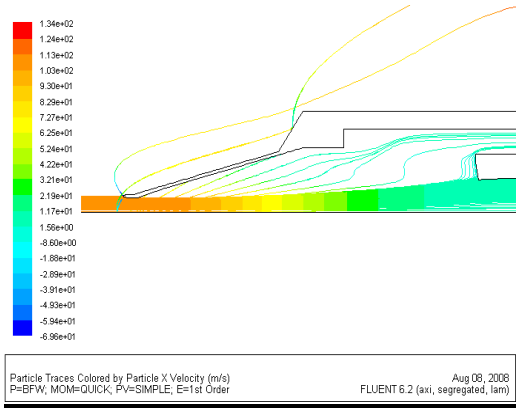

D_p=15 micron

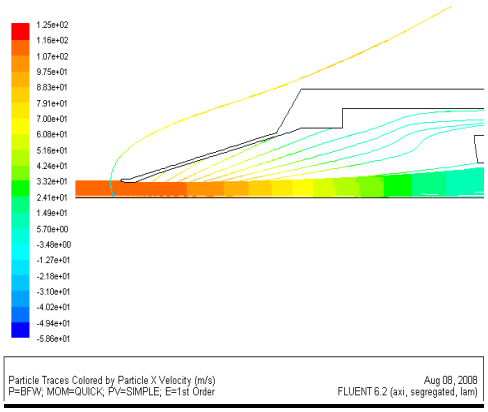

D_p=20 micron

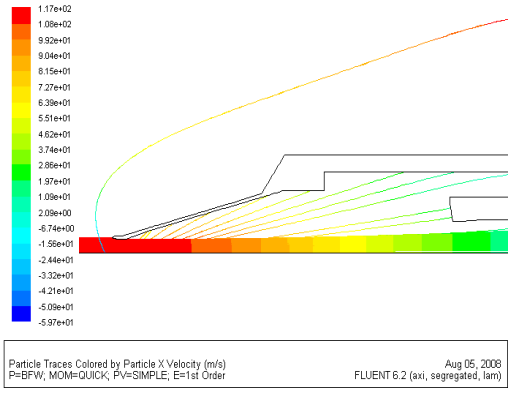

D_p=30 micron

Figure 4.8 Comparison of the overall view of particle trajectories in PELTI inlet for particles in 1-30 µm size range, TAS=115.6 ms^{-1}, P=93,521 Pa.

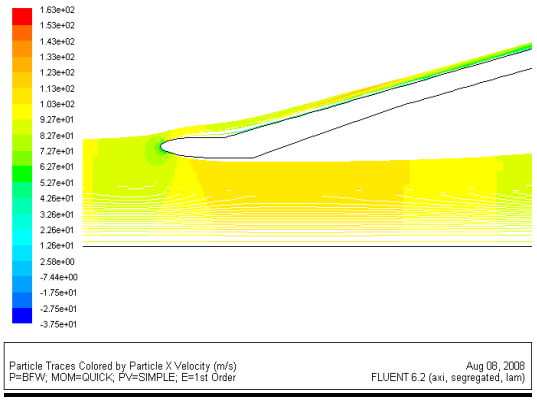

D_p=1 micron

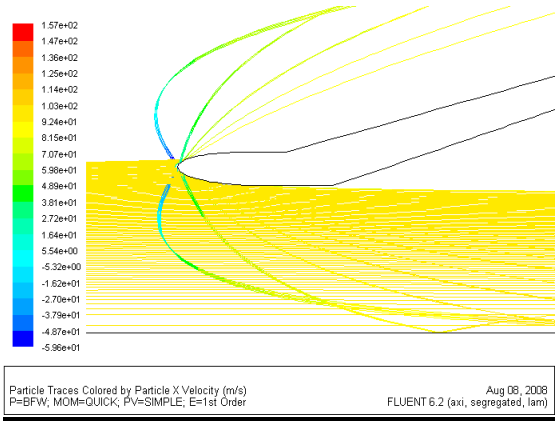

D_p=6 micron

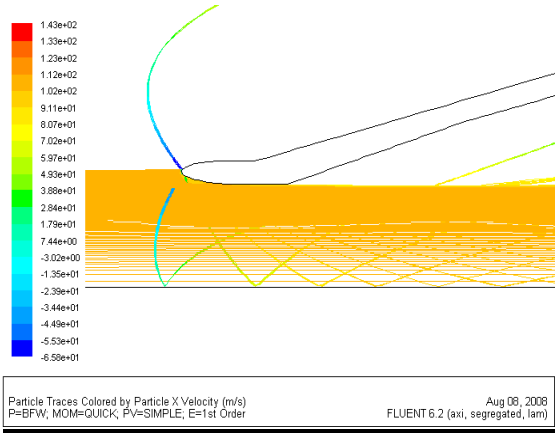

D_p=10 micron

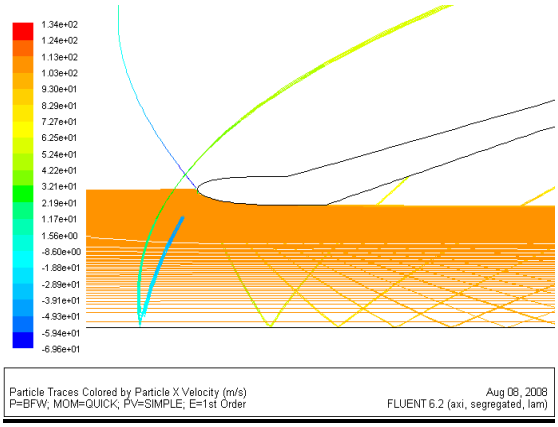

D_p=15 micron

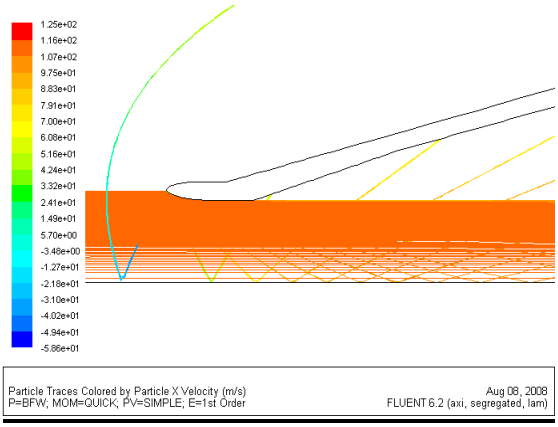

D_p=20 micron

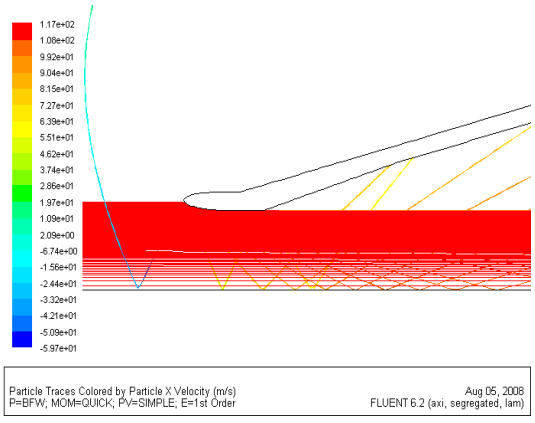

D_p=30 micron

Figure 4.9 Particle bounce after striking the leading edge in PELTI inlet for particles in 1-30 µm size range, TAS=115.6 ms^{-1}, P=93,521 Pa.

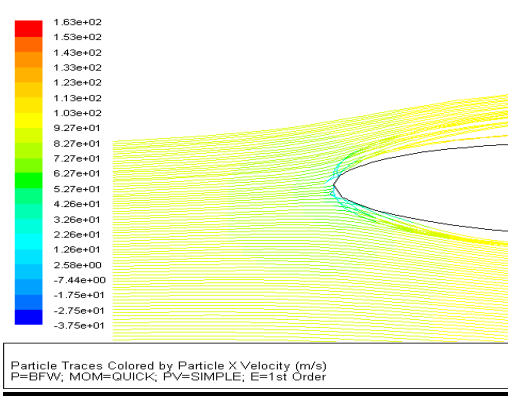

D_p=1 micron

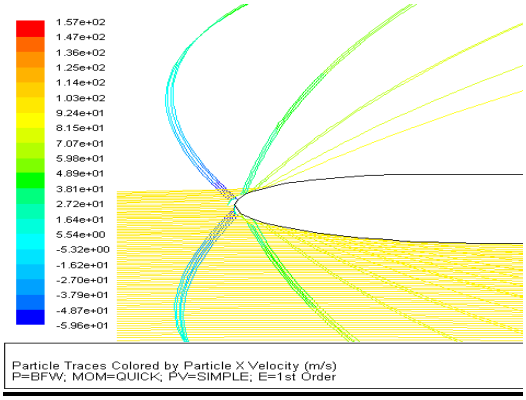

D_p=6 micron

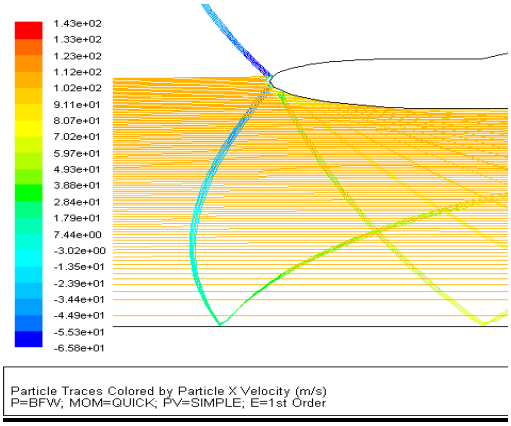

D_p=10 micron

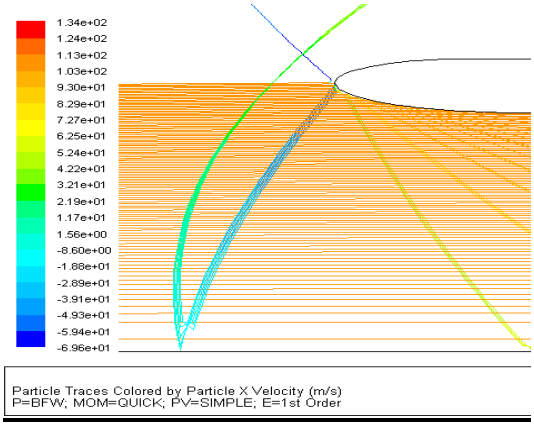

D_p=15 micron

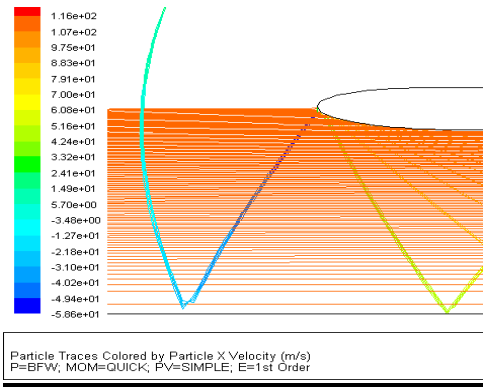

D_p=20 micron

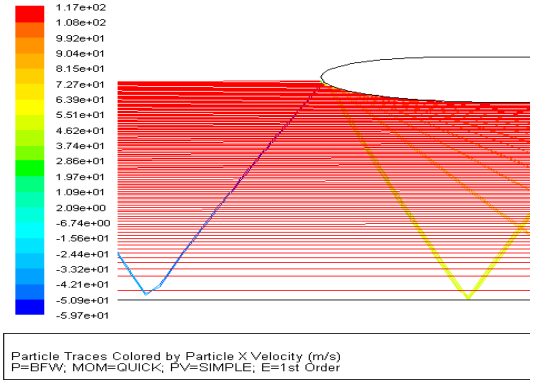

D_p=30 micron

Figure 4.10 Comparison of particle trajectories striking the leading edge in PELTI inlet for particles in 1-30 µm size range, TAS=115.6 ms^{-1}, P=93,521 Pa.

Chapter 5. Airborne Measurement of Aerodynamic Diameter of Coarse particles: Data Analysis

5.1 Introduction

This chapter describes the steps required to obtain the actual size distribution of super-micron particles in the atmosphere from the information provided by the instrument about the velocity of particles arriving at the measurement point inside the diffuser.

Unit density spherical particles are introduced to the pre-calculated flow fields and the particles' velocity is determined using the laser-Doppler velocimetry technique. A particles counter counts the number of particles passing through the viewing volume of LDV at a specific velocity range per second. In the numerical analysis of the instrument in Fluent, the particle velocity and the number of particles entering the sensing volume are determined from particle trajectory calculations. The use of LDV and particle counter refers to the actual proposed instrument. Knowing the volumetric flow rate of air at measuring volume, this information can lead to the calculation of the size distribution of particles (number of particles in unit volume of air in a size range) at the sensing volume. The size distribution of particles in ambient air is then calculated by relating the size distribution of particles at the measurement point to that of the atmosphere.

As discussed in chapter 4, a number of particles hit the leading edge of the inlet before entering the diffuser. Considering an elastic collision between the particles and the inlet leading edge, these particles bounce off the edge of the inlet and enter the diffuser in a different direction with different axial velocity. A fraction of the particles that hit the

inlet leading edge escape the calculation domain and return back to the atmosphere. The total number of particles that collide with the surface of the leading edge and enter the viewing volume of the velocimeter is given in table 4.1 for every particle size.

5.2 Instrument Output

The instrument output is in the form of a matrix that provides the information about the number of particles it detects in each specific velocity range, called the velocity channel. Particles of unknown size, density and shape enter the viewing volume of LDV one at a time and their velocity is calculated based on the frequency of the light scattered from the particles, which is described in detail in chapter 3. The instrument then puts the particle in a specific bin that belongs to all the particles that have arrived at the sensing volume at the same velocity range, regardless of their size, shape, composition or origin. The instrument output matrix I is:

$$I = \begin{bmatrix} I_1 \\ I_2 \\ I_3 \\ \vdots \\ I_m \end{bmatrix}_{mx1} \tag{5.1}$$

m is the number of velocity channels and I_m is the number of particles detected by the instrument in velocity channel m, i.e the number of particles detected with velocity in the range of $V_{LBm} < V < V_{UBm}$, where LBm and UBm are the lower bound and the upper bound of the velocity in the m^{th} velocity channel.

5.3 Determination of Response Matrix

The response matrix is an mxn matrix that is determined through numerical calibration and is provided to the users of the instrument in field experiments. It will be

then used to calculate the actual size distribution of the particles at the measurement point. The response matrix R is:

$$R = \begin{bmatrix} F_{11} & F_{12} & \cdots & F_{1n} \\ F_{21} & F_{22} & \cdots & F_{2n} \\ F_{31} & F_{32} & \cdots & F_{3n} \\ \vdots & & & \\ F_{m1} & F_{m2} & \cdots & F_{mn} \end{bmatrix}_{mxn} \tag{5.2}$$

n is the number of size ranges specified by the instrument, and F_{mn} is the fraction of particles in the n^{th} size range that are measured in the m^{th} velocity range. Therefore the rows in the response matrix represent the different velocity channels whereas the columns represent the different size ranges of the particles.

In order to generate the response matrix, the following information needs to be extracted from the particle trajectory and velocity measurements at the measuring point in the flow.

For every particle in the size range of 1-30 μm diameter:

- N = Total number of particles in a specific size range detected by the sensing element.
- N_{Direct} = Number of "Direct" particles detected by the sensing element, which includes all the particles of the same size, arriving directly through the limiting trajectory of that specific particle size, and therefore traveling at the full velocity corresponding to the expected velocity of that particular size.
- $N_{collision}$ = Number of particles of a specific size, arriving at the measuring volume as a result of collision with the leading edge of the inlet and therefore detected by the sensor with a velocity that is lower than their expected arrival velocity. The

particles of a particular size that have collided the leading edge of the inlet may arrive at the measuring volume with different velocities depending on their trajectory after the collision. Therefore particles of the same size may appear in several different velocity channels, which can be defined as:

- N_{C1} = Number of particles arriving at velocity V_1.
- N_{C2} = Number of particles arriving at velocity V_2.
- N_{Cm}= Number of particles arriving at velocity V_m.

Therefore, $$N_{collision} = N_{C1} + N_{C2} + \ldots + N_{Cm} \quad (5.3)$$

For every velocity channel defined by the instrument, the following information is required:

- I = Total number of particles of different sizes, detected by the instrument at a specific velocity range.
- N'_{Direct} = Number of particles that actually belong to the specific channel in question, based on their size.
- $N'_{Collision}$ = Number of particles that have reached the measuring volume at a specific velocity as a result of colliding with the leading edge of the inlet. In other words, these particles would not have ended up in the viewing volume at this lower velocity, had they not collided with the leading edge of the diffuser. There may be particles of different sizes that show up in the viewing volume at a specific velocity and they may be classified as:

- N_{Dp+1} = Number of particles in one size bigger range that arrive with a velocity corresponding to a particle with one size smaller in size.
- N_{Dp+2} = Number of particles in two sizes bigger range that arrive with a velocity corresponding to a particle with two sizes smaller in size.
- N_{Dp+n} = Number of particles in n sizes bigger range that arrive with a velocity corresponding to a particle with n sizes smaller in size.

The elements of the response matrix, F_{mn}, give the fraction of particles in the n^{th} size range that arrive in the measuring volume with a velocity in the m^{th} velocity range. F_{mn} includes contributions from the particles that pass from the outside of the instrument through the viewing volume without striking the leading edge of the instrument and those which bounce elastically off of the leading edge and enter the viewing volume.

5.4 Determination of Ambient Size Distribution using Response Matrix and the Trajectories of Particles that have Bounced into the Viewing Volume

The first step towards the determination of ambient size distribution is to calculate the actual size distribution of particles at measurement point. Then, the ambient size distribution is determined by applying the relation between the size distribution of particles at the detection point and in the atmosphere.

The instrument output, I_m, and the actual size distribution, A_n, of the particles at the measurement point are related through the response matrix by:

$$\begin{bmatrix} I_1 \\ I_2 \\ I_3 \\ \vdots \\ I_m \end{bmatrix}_{mx1} = \begin{bmatrix} F_{11} & F_{12} & \cdots & F_{1n} \\ F_{21} & F_{22} & \cdots & F_{2n} \\ F_{31} & F_{32} & \cdots & F_{3n} \\ \vdots & & & \\ F_{m1} & F_{m2} & \cdots & F_{mn} \end{bmatrix}_{mxn} \begin{bmatrix} A_1 \\ A_2 \\ A_3 \\ \vdots \\ A_n \end{bmatrix}_{nx1} \tag{5.4}$$

Or, $I = R\,A$

I is the instrument output matrix, R being the response matrix and A the actual size distribution matrix at the sensing volume. n is the number of size ranges and A_n is the actual number of particles detected in the n^{th} size range.

To determine the actual number of particles detected by the instrument, the inverse of the response matrix is multiplied by the instrument response matrix, i.e.

$A = R^{-1}\,I.$

$$\begin{bmatrix} A_1 \\ A_2 \\ A_3 \\ \vdots \\ A_n \end{bmatrix}_{nx1} = \begin{bmatrix} F_{11} & F_{12} & \cdots & F_{1n} \\ F_{21} & F_{22} & \cdots & F_{2n} \\ F_{31} & F_{32} & \cdots & F_{3n} \\ \vdots & & & \\ F_{m1} & F_{m2} & \cdots & F_{mn} \end{bmatrix}^{-1}_{mxn} \begin{bmatrix} I_1 \\ I_2 \\ I_3 \\ \vdots \\ I_m \end{bmatrix}_{mx1} \tag{5.5}$$

The solution of matrix A gives the actual concentration of particles in each size range detected at the measuring point inside the nozzle. In order to determine the ambient concentration of particles in each size range, the actual detected particles in each size range must be related to the ambient concentration through some factor, *f(Dp),* to include the limiting trajectory analysis for the direct particles and the bounced particles.

If all the bounced particles had been removed from the flow before entering the diffuser, then the determination of ambient size distribution would have been straight forward, following the particle limiting trajectory analysis.

5.4.1 Determination of Ambient Size Distribution: Ideal Case-No Bounced Particles in Viewing Volume

Figure 5.1 demonstrates an ideal case in which no bouncing particles enter the viewing volume of the laser-Doppler velocimeter. In this case, the particles that arrive at the viewing volume all originated from inside the imaginary circle of limiting trajectory.

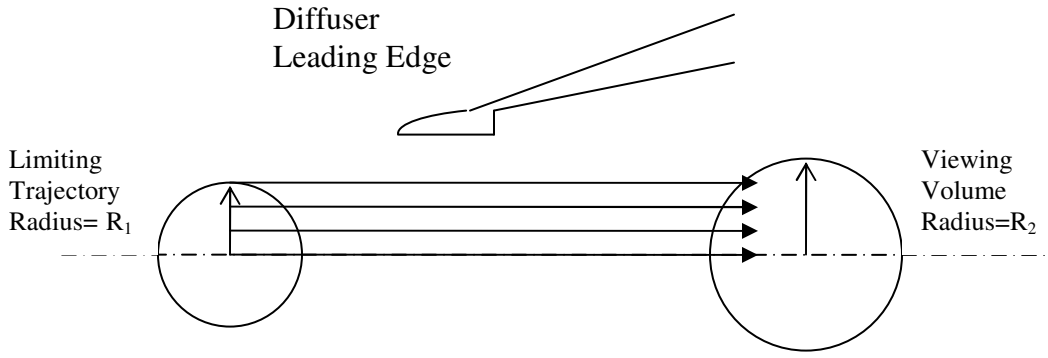

Figure 5.1 Ideal case- no bouncing particles in LDV viewing volume.

The limiting trajectory and viewing volume circles are actually perpendicular to the axis. They are shown parallel to the axis for clarity.

The following set of equations is used to determine the ambient particle concentration in an ideal case, where there are no bounced particles present in the viewing volume of the measuring instrument.

$$Q_1 = (\pi R_1^2) V_{TAS} \tag{5.6}$$

$$Q_2 = (\pi R_2^2) V_{air\ at\ R_2} \tag{5.7}$$

$$N_1 = \frac{N}{Q_1} \tag{5.8}$$

$$N_2 = \frac{N}{Q_2} \tag{5.9}$$

$$EF = \frac{Q_1}{Q_2} \tag{5.10}$$

$$EF = \frac{N_2}{N_1} \tag{5.11}$$

R_1= Radius of the limiting trajectory circle, m

R_2= Radius of the projected area of the viewing volume perpendicular to the flow, m

N_1= Actual aerosol concentration at R_1, #/m^3

N_2= Aerosol concentration at R_2 (LDV location), #/m^3

N= Number of particles /s at R_1= Number of particles at R_2 (in steady state), #/s

Q_1= Volumetric air flow rate upstream at R_1, m^3/s

Q_2= Volumetric air flow rate at R_2 (LDV location), m^3/s

The radius of the limiting trajectory circle, R_1, is not known in the field experiments. The actual aerosol concentration, N_1, is then the only unknown in the above set of equations. The enhancement factor, *EF*, is determined from numerical calibration by using the relationship between the volumetric flow rate of air upstream the inlet and the volumetric flow rate of air at LDV location. Then the known *EF* is used to determine the actual ambient concentration of particles, N_1, from Equation (5.11).

5.4.2 Determination of Ambient Size Distribution using Response Matrix including Bouncing Particles

The determination of ambient particle concentration in real cases, Figure 5.2, where there are some particles that strike the surface of the leading edge, bounce off the surface, change their direction and enter the viewing volume at a different velocity involves the introduction of the response matrix. Once the actual number concentration of particles at detection point is determined using the response matrix, then the same logic of limiting trajectory with an additional function to account for the collided particles is used to determine the ambient size distribution.

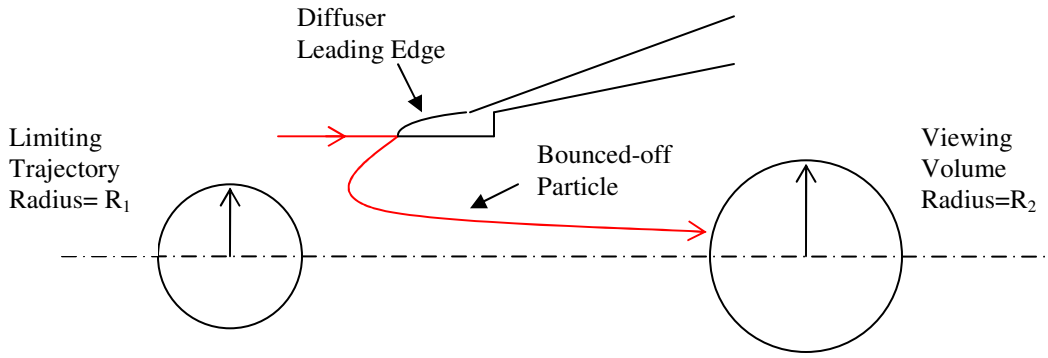

Figure 5.2 Real case- bounced particles in LDV viewing volume.

Knowing the number of particles detected in each size range at the measurement point, the ambient concentration of particles is calculated from Equation (5.12).

$$C(D_p) = \frac{[A(D_p)][1 - f(D_p)]}{TAS * \pi R_1^2} \tag{5.12}$$

C(Dp)= Concentration of particles in atmosphere in each size range.

A(Dp) = Number of Particles detected in each size range at the measurement point per second.

TAS = True Air Speed of aircraft, ms^{-1}.

R_1 = Radius of limiting trajectory circle, known through trajectory calculations.

$f(Dp)$= fraction of particles in viewing volume that are the result of particle collision with leading edge of the inlet, determined from trajectory calculations.

5.5 Case Study: ACE-Asia and PELTI Inlets under Different Flow Conditions

The response matrix is calculated for ACE-Asia and PELTI inlets under seven different flow conditions. 120 evenly distributed particles with D_p= 1-30 μm and ρ_p=1000 Kgm^{-3} are injected to the flow and particle velocity is plotted against the axial flow path of the diffuser. In each case, the particles radial positions are evaluated to determine the number of particles that hit the sensing volume of LDV. The velocity of particles that collide with the leading edge of the inlet is smaller than the velocity of the particles that enter the sensor without colliding with the inlet head. This defines the two sets of particles in each size range as N_{direct} and $N_{collision}$. The response matrix is then created following the steps described in section 5.3.

Table 5.1 summarizes the geometry and flow conditions of seven different cases studied in this work.

Table 5.1 ACE-Asia and PELTI inlets studied under different flow conditions.

Cases	Ambient Pressure (Pa)	Altitude (km)	Aircraft True Air Speed (m/s)	Entrance Air Velocity (m/s)	Sub-isokinetic Ratio	Core Mass Flow Ratio
ACE-Asia	53,000	5.1	113.6	81	0.71	0.07
ACE-Asia	84,600	1.5	113.6	105	0.92	0.27
PELTI	93,521	0.7	115.6	103	0.89	0.20
PELTI	86,168	1.3	119.2	99	0.83	0.196
PELTI	74,920	2.5	120.4	96	0.79	0.176
PELTI	53,379	5	140.3	114	0.81	0.154
PELTI	45,778	6.2	154.6	116	0.75	0.181

The above seven cases cover the range of altitudes from 0.7 km to 6.2 km and the core mass flow ratios from 0.07 to 0.27. The air is slowed down at the inlet entrance and the flow entering the diffuser is sub-isokinetic for all the cases.

Table 5.2 shows the result of particle velocity calculations at the measurement point for all the seven cases studied.

Table 5.2 Particle velocity as a function of particle size at various air speeds and pressures, corresponding to ACE-Asia and PELTI inlets.

Dp (μm)	TAS= 154.6 m/s P= 45,778 Pa	TAS= 113.6 m/s P= 53,000 Pa	TAS= 140.3 m/s P= 53,379 Pa	TAS= 120.4 m/s P= 74,920 Pa	TAS= 113.6 m/s P= 84,600 Pa	TAS= 119.2 m/s P= 86,168 Pa	TAS= 115.6 m/s P= 93,521 Pa
1	103.14	70.34	100.56	85.46	100.01	90.83	94.29
2	105.36	71.44	102.63	86.85	102.00	92.32	96.6
4	110.4	74.88	107.37	90.41	106.42	95.95	100.31
6	114.22	77.85	110.03	92.65	107.91	97.79	101.03
8	118.62	81.01	112.82	94.79	107.72	99	101.73
10	123.14	84.48	115.8	97.15	107.54	100.51	102.91
15	131.93	91.89	122.16	102.5	108.43	104.45	106.06
20	137.76	97.02	126.53	106.43	109.82	107.53	108.39
25	141.71	100.69	129.57	109.32	110.96	109.83	110.01
30	144.41	103.28	131.74	111.43	111.75	111.54	111.15

5.5.1 Determination of Response Matrix: Sample case: ACE-Asia, TAS=113.6 ms^{-1}, P=53,000 Pa.

This section explains the procedure to determine the response matrix from the numerical results of one of the seven cases included in table 5.3. The similar results from the other six cases are given in Appendix F. The particles in the size range of 1-34 μm are injected to the ACE-Asia inlet and particle trajectories are calculated. The velocity of particles is recorded as they hit the sensing volume of LDV. The output of the instrument

is the number of particles that arrive at the viewing volume in a specific velocity range. This information can not simply translate to the knowledge of the particle size, since the particles of different sizes may arrive at the detection point with the same velocity due to the collision with the leading edge of the inlet. In this particular case, 34 velocity channels are defined corresponding to the particle size ranges from 1-34 micron with 1 micron increments. Table 5.1 shows the total number of particles arriving at the measurement point within a velocity range. The 34 velocity channels and the boundary of each channel are also given in the table. The next task is to identify, remove and relocate the particles that have entered the viewing volume at a lower velocity due to the collision with the leading edge of the inlet. This is achieved thru the determination of the response matrix. The response matrix is shown in tables 5.4 and 5.5 in total and fractional forms.

Table 5.3 Instrument output matrix I, number of particles detected in each velocity range.

Velocity Channels	Velocity Range	Matrix I Total # of Particles Detected by the Instrument in each velocity Range	# of particles entering the diffuser without colliding with leading edge in each velocity range	# of Particles hitting sensor after colliding with leading edge, in each velocity range
1	$104.81 \leq Vp < 105.14$	12	12	0
2	$104.46 \leq Vp < 104.81$	12	12	0
3	$104.09 \leq Vp < 104.46$	12	12	0
4	$103.7 \leq Vp < 104.09$	12	12	0
5	$103.28 \leq Vp < 103.7$	12	12	0
6	$102.83 \leq Vp < 103.28$	12	12	0
7	$102.35 \leq Vp < 102.83$	12	12	0
8	$101.84 \leq Vp < 102.35$	12	12	0
9	$101.29 \leq Vp < 101.84$	13	12	1
10	$100.69 \leq Vp < 101.29$	14	12	2
11	$100.06 \leq Vp < 100.69$	13	12	1
12	$99.38 \leq Vp < 100.06$	16	12	4
13	$98.65 \leq Vp < 99.38$	15	12	3
14	$97.86 \leq Vp < 98.65$	17	12	5
15	$97.02 \leq Vp < 97.86$	18	11	7
16	$96.12 \leq Vp < 97.02$	19	11	8
17	$95.15 \leq Vp < 96.12$	17	11	6
18	$94.13 \leq Vp < 95.15$	16	11	5
19	$93.04 \leq Vp < 94.13$	17	11	6
20	$91.89 \leq Vp < 93.04$	17	11	6
21	$90.63 \leq Vp < 91.89$	14	10	4
22	$89.27 \leq Vp < 90.63$	16	11	5
23	$87.78 \leq Vp < 89.27$	16	11	5
24	$86.17 \leq Vp < 87.78$	18	11	7
25	$84.48 \leq Vp < 86.17$	13	10	3
26	$82.74 \leq Vp < 84.48$	18	10	8
27	$81.08 \leq Vp < 82.74$	16	10	6
28	$79.38 \leq Vp < 81.08$	17	10	7
29	$77.85 \leq Vp < 79.38$	18	10	8
30	$76.39 \leq Vp < 77.85$	22	9	13
31	$74.88 \leq Vp < 76.39$	21	9	12
32	$73.17 \leq Vp < 74.88$	13	9	4
33	$71.49 \leq Vp < 73.17$	9	9	0
34	$70.34 \leq Vp < 71.49$	8	8	0

In this study, 120 evenly distributed unit density particles in the size range of 1-34 µm are injected to the diffuser. 34 injection files are created presenting the particles in the size range of interest. Figure 5.3 shows the results of particle trajectories for 10 µm particles inside the viewing volume of LDV. The measurement point of the instrument is located at the center of the diffuser, 2.16 cm from the inlet entrance. It is 4 mm wide, 2 mm of which is modeled in the axisymmetric model of the inlet in Fluent.

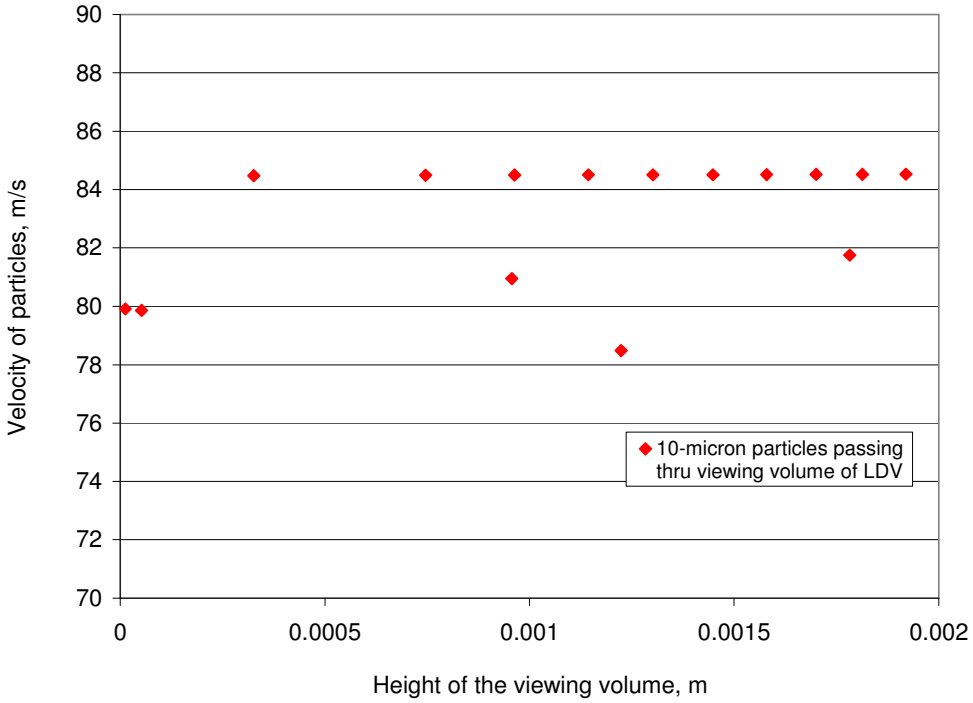

Figure 5.3 Velocity of 10-micron particles inside the viewing volume of LDV.

Out of 120 particles that were entered the calculation domain, only 15 showed up in the sensing volume of the instrument. Among these 15 particles, 10 particles arrived at a velocity of about 84.5 ms^{-1}. These particles were all originated in the limiting trajectory circle and therefore hit the sensor directly and did not collide with the inlet leading edge.

The other 5 particles that arrived at the sensor with a lower velocity (~78.5-~81.9 ms^{-1}) entered the domain after colliding with the leading edge of the inlet. The velocity range of these 5 particles corresponds to the velocity of particles that are one or more sizes smaller than 10 μm. On the other hand, the result of particle trajectory calculations for particles larger than 10 μm revealed that some of those larger particles also collided with the leading edge of the inlet and as a result, arrived the measurement point at a lower velocity, which in fact may show up in the velocity range that corresponds to 10 μm particles. Therefore, in order to determine the actual number of 10 μm particles that arrived at the viewing volume of the instrument, a two step procedure is required: (a) elimination of the larger particles that collided with the inlet leading edge, and addition of 10 μm particles that collided with the leading edge of the inlet. The response matrix fixes both the problems.

The response matrix is a 34x34 matrix. The rows of the matrix correspond to the 34 velocity ranges of the particles as they hit the sensing volume of the instrument and the columns of the matrix correspond to the 34 particle size ranges from 1 to 34 μm. For example, the 10^{th} column of the matrix will have 10 particles in the row with a velocity range that includes 84.5 ms^{-1}, and the other 5 particles each fill the rows that cover the range of their velocities. Table 5.4 shows the first step towards the creation of the response matrix for this specific case. The actual response matrix is in the fractional form, which is shown in Table 5.5.

Table 5.4 Response matrix, number of particles detected by the instrument at each velocity range and each size range (1 of 5).

Velocity Channels	Velocity Range	33 ≤ Dp < 34	32 ≤ Dp < 33	31 ≤ Dp < 32	30 ≤ Dp < 31
1	104.81 ≤ Vp < 105.14	12	0	0	0
2	104.46 ≤ Vp < 104.81	0	12	0	0
3	104.09 ≤ Vp < 104.46	0	0	12	0
4	103.7 ≤ Vp < 104.09	0	0	0	12
5	103.28 ≤ Vp < 103.7	0	0	0	0
6	102.83 ≤ Vp < 103.28	0	0	0	0
7	102.35 ≤ Vp < 102.83	0	0	0	0
8	101.84 ≤ Vp < 102.35	0	0	0	0
9	101.29 ≤ Vp < 101.84	1	0	0	0
10	100.69 ≤ Vp < 101.29	0	1	1	0
11	100.06 ≤ Vp < 100.69	0	0	0	1
12	99.38 ≤ Vp < 100.06	1	1	0	0
13	98.65 ≤ Vp < 99.38	0	0	1	1
14	97.86 ≤ Vp < 98.65	0	0	0	0
15	97.02 ≤ Vp < 97.86	2	2	0	0
16	96.12 ≤ Vp < 97.02	0	0	2	1
17	95.15 ≤ Vp < 96.12	0	0	0	0
18	94.13 ≤ Vp < 95.15	0	0	0	0
19	93.04 ≤ Vp < 94.13	0	0	0	0
20	91.89 ≤ Vp < 93.04	0	0	0	0
21	90.63 ≤ Vp < 91.89	0	0	0	0
22	89.27 ≤ Vp < 90.63	0	0	0	0
23	87.78 ≤ Vp < 89.27	0	0	0	0
24	86.17 ≤ Vp < 87.78	0	0	0	0
25	84.48 ≤ Vp < 86.17	0	0	0	0
26	82.74 ≤ Vp < 84.48	0	0	0	0
27	81.08 ≤ Vp < 82.74	0	0	0	0
28	79.38 ≤ Vp < 81.08	0	0	0	0
29	77.85 ≤ Vp < 79.38	0	0	0	0
30	76.39 ≤ Vp < 77.85	0	0	0	0
31	74.88 ≤ Vp < 76.39	0	0	0	0
32	73.17 ≤ Vp < 74.88	0	0	0	0
33	71.49 ≤ Vp <73.17	0	0	0	0
34	70.34 ≤ Vp < 71.49	0	0	0	0

Table 5.4 Response matrix, number of particles detected by the instrument at each velocity range and each size range (2 of 5).

29 ≤ Dp < 30	28 ≤ Dp < 29	27 ≤ Dp < 28	26 ≤ Dp < 27	25 ≤ Dp < 26	24 ≤ Dp < 25	23 ≤ Dp < 24
0	0	0	0	0	0	0
0	0	0	0	0	0	0
0	0	0	0	0	0	0
0	0	0	0	0	0	0
12	0	0	0	0	0	0
0	12	0	0	0	0	0
0	0	12	0	0	0	0
0	0	0	12	0	0	0
0	0	0	0	12	0	0
0	0	0	0	0	12	0
0	0	0	0	0	0	12
1	1	0	0	0	0	0
0	0	1	0	0	0	0
1	2	0	1	1	0	0
0	0	2	0	0	1	0
1	1	0	1	1	0	1
0	0	1	0	0	1	2
0	0	0	2	1	0	0
0	0	0	0	0	1	1
0	0	0	0	0	0	0
0	0	0	0	0	0	0
0	0	0	0	0	0	0
0	0	0	0	0	0	0
0	0	0	0	0	0	0
0	0	0	0	0	0	0
0	0	0	0	0	0	0
0	0	0	0	0	0	0
0	0	0	0	0	0	0
0	0	0	0	0	0	0
0	0	0	0	0	0	0
0	0	0	0	0	0	0
0	0	0	0	0	0	0
0	0	0	0	0	0	0
0	0	0	0	0	0	0
0	0	0	0	0	0	0
0	0	0	0	0	0	0

Table 5.4 Response matrix, number of particles detected by the instrument at each velocity range and each size range (3 of 5).

22 ≤ Dp < 23	21 ≤ Dp < 22	20 ≤ Dp < 21	19 ≤ Dp < 20	18 ≤ Dp < 19	17 ≤ Dp < 18	16 ≤ Dp < 17
0	0	0	0	0	0	0
0	0	0	0	0	0	0
0	0	0	0	0	0	0
0	0	0	0	0	0	0
0	0	0	0	0	0	0
0	0	0	0	0	0	0
0	0	0	0	0	0	0
0	0	0	0	0	0	0
0	0	0	0	0	0	0
0	0	0	0	0	0	0
0	0	0	0	0	0	0
0	0	0	0	0	0	0
12	0	0	0	0	0	0
0	12	0	0	0	0	0
0	0	12	0	0	0	0
0	0	0	11	0	0	0
0	0	0	0	11	0	0
1	1	0	0	0	11	0
1	0	1	0	0	0	11
0	1	2	1	0	0	0
2	1	0	1	1	1	0
0	0	1	0	1	1	1
0	0	0	2	1	0	1
0	0	0	0	0	2	1
0	0	0	0	0	0	0
0	0	0	0	0	0	0
0	0	0	0	0	0	0
0	0	0	0	0	0	0
0	0	0	0	0	0	0
0	0	0	0	0	0	0
0	0	0	0	0	0	0
0	0	0	0	0	0	0
0	0	0	0	0	0	0
0	0	0	0	0	0	0

Table 5.4 Response matrix, number of particles detected by the instrument at each velocity range and each size range (4 of 5).

15 ≤ Dp < 16	14 ≤ Dp < 15	13 ≤ Dp < 14	12 ≤ Dp < 13	11 ≤ Dp < 12	10 ≤ Dp < 11	9 ≤ Dp < 10	8 ≤ Dp < 9
0	0	0	0	0	0	0	0
0	0	0	0	0	0	0	0
0	0	0	0	0	0	0	0
0	0	0	0	0	0	0	0
0	0	0	0	0	0	0	0
0	0	0	0	0	0	0	0
0	0	0	0	0	0	0	0
0	0	0	0	0	0	0	0
0	0	0	0	0	0	0	0
0	0	0	0	0	0	0	0
0	0	0	0	0	0	0	0
0	0	0	0	0	0	0	0
0	0	0	0	0	0	0	0
0	0	0	0	0	0	0	0
0	0	0	0	0	0	0	0
0	0	0	0	0	0	0	0
0	0	0	0	0	0	0	0
0	0	0	0	0	0	0	0
0	0	0	0	0	0	0	0
11	0	0	0	0	0	0	0
0	11	0	0	0	0	0	0
0	0	10	0	0	0	0	0
1	0	0	11	0	0	0	0
1	1	0	0	11	0	0	0
2	2	2	1	0	11	0	0
0	1	1	1	0	0	10	0
0	2	2	1	2	1	0	10
0	0	0	2	2	1	1	0
0	0	0	0	0	2	3	2
0	0	0	0	0	2	1	3
0	0	0	0	0	0	0	2
0	0	0	0	0	0	0	0
0	0	0	0	0	0	0	0
0	0	0	0	0	0	0	0
0	0	0	0	0	0	0	0

Table 5.4 Response matrix, number of particles detected by the instrument at each velocity range and each size range (5 of 5).

$7 \leq Dp < 8$	$6 \leq Dp < 7$	$5 \leq Dp < 6$	$4 \leq Dp < 5$	$3 \leq Dp < 4$	$2 \leq Dp \leq 3$	$1 \leq Dp \leq 2$	$0 < Dp \leq 1$
0	0	0	0	0	0	0	0
0	0	0	0	0	0	0	0
0	0	0	0	0	0	0	0
0	0	0	0	0	0	0	0
0	0	0	0	0	0	0	0
0	0	0	0	0	0	0	0
0	0	0	0	0	0	0	0
0	0	0	0	0	0	0	0
0	0	0	0	0	0	0	0
0	0	0	0	0	0	0	0
0	0	0	0	0	0	0	0
0	0	0	0	0	0	0	0
0	0	0	0	0	0	0	0
0	0	0	0	0	0	0	0
0	0	0	0	0	0	0	0
0	0	0	0	0	0	0	0
0	0	0	0	0	0	0	0
0	0	0	0	0	0	0	0
0	0	0	0	0	0	0	0
0	0	0	0	0	0	0	0
0	0	0	0	0	0	0	0
0	0	0	0	0	0	0	0
0	0	0	0	0	0	0	0
0	0	0	0	0	0	0	0
0	0	0	0	0	0	0	0
0	0	0	0	0	0	0	0
0	0	0	0	0	0	0	0
0	0	0	0	0	0	0	0
0	0	0	0	0	0	0	0
0	0	0	0	0	0	0	0
10	0	0	0	0	0	0	0
0	10	0	0	0	0	0	0
2	0	10	0	0	0	0	0
4	5	2	9	0	0	0	0
0	7	5	0	9	0	0	0
4	0	0	0	0	9	0	0
0	0	0	0	0	0	9	0
0	0	0	0	0	0	0	8

Table 5.5 Response matrix, R, in fractional form (1 of 5).

Velocity Channels	Velocity Range	33 ≤ Dp < 34	32 ≤ Dp < 33	31 ≤ Dp < 32	30 ≤ Dp < 31
1	104.81 ≤ Vp < 105.14	0.75	0	0	0
2	104.46 ≤ Vp < 104.81	0	0.75	0	0
3	104.09 ≤ Vp < 104.46	0	0	0.75	0
4	103.7 ≤ Vp < 104.09	0	0	0	0.8
5	103.28 ≤ Vp < 103.7	0	0	0	0
6	102.83 ≤ Vp < 103.28	0	0	0	0
7	102.35 ≤ Vp < 102.83	0	0	0	0
8	101.84 ≤ Vp < 102.35	0	0	0	0
9	101.29 ≤ Vp < 101.84	0.063	0	0	0
10	100.69 ≤ Vp < 101.29	0	0.063	0.063	0
11	100.06 ≤ Vp < 100.69	0	0	0	0.067
12	99.38 ≤ Vp < 100.06	0.063	0.063	0	0
13	98.65 ≤ Vp < 99.38	0	0	0.063	0.067
14	97.86 ≤ Vp < 98.65	0	0	0	0
15	97.02 ≤ Vp < 97.86	0.125	0.125	0	0
16	96.12 ≤ Vp < 97.02	0	0	0.125	0.067
17	95.15 ≤ Vp < 96.12	0	0	0	0
18	94.13 ≤ Vp < 95.15	0	0	0	0
19	93.04 ≤ Vp < 94.13	0	0	0	0
20	91.89 ≤ Vp < 93.04	0	0	0	0
21	90.63 ≤ Vp < 91.89	0	0	0	0
22	89.27 ≤ Vp < 90.63	0	0	0	0
23	87.78 ≤ Vp < 89.27	0	0	0	0
24	86.17 ≤ Vp < 87.78	0	0	0	0
25	84.48 ≤ Vp < 86.17	0	0	0	0
26	82.74 ≤ Vp < 84.48	0	0	0	0
27	81.08 ≤ Vp < 82.74	0	0	0	0
28	79.38 ≤ Vp < 81.08	0	0	0	0
29	77.85 ≤ Vp < 79.38	0	0	0	0
30	76.39 ≤ Vp < 77.85	0	0	0	0
31	74.88 ≤ Vp < 76.39	0	0	0	0
32	73.17 ≤ Vp < 74.88	0	0	0	0
33	71.49 ≤ Vp <73.17	0	0	0	0
34	70.34 ≤ Vp < 71.49	0	0	0	0

Table 5.5 Response matrix, R, in fractional form (2 of 5).

29 ≤ Dp < 30	28 ≤ Dp < 29	27 ≤ Dp < 28	26 ≤ Dp < 27	25 ≤ Dp < 26	24 ≤ Dp < 25	23 ≤ Dp < 24
0	0	0	0	0	0	0
0	0	0	0	0	0	0
0	0	0	0	0	0	0
0	0	0	0	0	0	0
0.8	0	0	0	0	0	0
0	0.75	0	0	0	0	0
0	0	0.75	0	0	0	0
0	0	0	0.75	0	0	0
0	0	0	0	0.8	0	0
0	0	0	0	0	0.8	0
0	0	0	0	0	0	0.75
0.067	0.063	0	0	0	0	0
0	0	0.063	0	0	0	0
0.067	0.125	0	0.063	0.067	0	0
0	0	0.125	0	0	0.067	0
0.067	0.063	0	0.063	0.067	0	0.063
0	0	0.063	0	0	0.067	0.125
0	0	0	0.125	0.067	0	0
0	0	0	0	0	0.067	0.063
0	0	0	0	0	0	0
0	0	0	0	0	0	0
0	0	0	0	0	0	0
0	0	0	0	0	0	0
0	0	0	0	0	0	0
0	0	0	0	0	0	0
0	0	0	0	0	0	0
0	0	0	0	0	0	0
0	0	0	0	0	0	0
0	0	0	0	0	0	0
0	0	0	0	0	0	0
0	0	0	0	0	0	0
0	0	0	0	0	0	0
0	0	0	0	0	0	0
0	0	0	0	0	0	0
0	0	0	0	0	0	0
0	0	0	0	0	0	0

Table 5.5 Response matrix, R, in fractional form (3 of 5).

22 ≤ Dp < 23	21 ≤ Dp < 22	20 ≤ Dp < 21	19 ≤ Dp < 20	18 ≤ Dp < 19	17 ≤ Dp < 18	16 ≤ Dp < 17
0	0	0	0	0	0	0
0	0	0	0	0	0	0
0	0	0	0	0	0	0
0	0	0	0	0	0	0
0	0	0	0	0	0	0
0	0	0	0	0	0	0
0	0	0	0	0	0	0
0	0	0	0	0	0	0
0	0	0	0	0	0	0
0	0	0	0	0	0	0
0	0	0	0	0	0	0
0.75	0	0	0	0	0	0
0	0.8	0	0	0	0	0
0	0	0.75	0	0	0	0
0	0	0	0.733	0	0	0
0	0	0	0	0.786	0	0
0.063	0.067	0	0	0	0.733	0
0.063	0	0.063	0	0	0	0.786
0	0.067	0.125	0.067	0	0	0
0.125	0.067	0	0.067	0.071	0.067	0
0	0	0.063	0	0.071	0.067	0.071
0	0	0	0.133	0.071	0	0.071
0	0	0	0	0	0.133	0.071
0	0	0	0	0	0	0
0	0	0	0	0	0	0
0	0	0	0	0	0	0
0	0	0	0	0	0	0
0	0	0	0	0	0	0
0	0	0	0	0	0	0
0	0	0	0	0	0	0
0	0	0	0	0	0	0
0	0	0	0	0	0	0
0	0	0	0	0	0	0
0	0	0	0	0	0	0

Table 5.5 Response matrix, R, in fractional form (4 of 5).

15 ≤ Dp < 16	14 ≤ Dp < 15	13 ≤ Dp < 14	12 ≤ Dp < 13	11 ≤ Dp < 12	10 ≤ Dp < 11	9 ≤ Dp < 10	8 ≤ Dp < 9
0	0	0	0	0	0	0	0
0	0	0	0	0	0	0	0
0	0	0	0	0	0	0	0
0	0	0	0	0	0	0	0
0	0	0	0	0	0	0	0
0	0	0	0	0	0	0	0
0	0	0	0	0	0	0	0
0	0	0	0	0	0	0	0
0	0	0	0	0	0	0	0
0	0	0	0	0	0	0	0
0	0	0	0	0	0	0	0
0	0	0	0	0	0	0	0
0	0	0	0	0	0	0	0
0	0	0	0	0	0	0	0
0	0	0	0	0	0	0	0
0	0	0	0	0	0	0	0
0	0	0	0	0	0	0	0
0	0	0	0	0	0	0	0
0	0	0	0	0	0	0	0
0.733	0	0	0	0	0	0	0
0	0.647	0	0	0	0	0	0
0	0	0.067	0	0	0	0	0
0.067	0	0	0.6875	0	0	0	0
0.067	0.059	0	0	0.733	0	0	0
0.133	0.118	0.133	0.063	0	0.647	0	0
0	0.059	0.067	0.063	0	0	0.067	0
0	0.118	0.133	0.063	0.133	0.059	0	0.588
0	0	0	0.125	0.133	0.059	0.067	0
0	0	0	0	0	0.118	0.2	0.118
0	0	0	0	0	0.118	0.067	0.118
0	0	0	0	0	0	0	0.118
0	0	0	0	0	0	0	0
0	0	0	0	0	0	0	0
0	0	0	0	0	0	0	0
0	0	0	0	0	0	0	0

Table 5.5 Response matrix, R, in fractional form (5 of 5).

$7 \leq Dp < 8$	$6 \leq Dp < 7$	$5 \leq Dp < 6$	$4 \leq Dp < 5$	$3 \leq Dp < 4$	$2 \leq Dp \leq 3$	$1 \leq Dp \leq 2$	$0 < Dp \leq 1$
0	0	0	0	0	0	0	0
0	0	0	0	0	0	0	0
0	0	0	0	0	0	0	0
0	0	0	0	0	0	0	0
0	0	0	0	0	0	0	0
0	0	0	0	0	0	0	0
0	0	0	0	0	0	0	0
0	0	0	0	0	0	0	0
0	0	0	0	0	0	0	0
0	0	0	0	0	0	0	0
0	0	0	0	0	0	0	0
0	0	0	0	0	0	0	0
0	0	0	0	0	0	0	0
0	0	0	0	0	0	0	0
0	0	0	0	0	0	0	0
0	0	0	0	0	0	0	0
0	0	0	0	0	0	0	0
0	0	0	0	0	0	0	0
0	0	0	0	0	0	0	0
0	0	0	0	0	0	0	0
0	0	0	0	0	0	0	0
0	0	0	0	0	0	0	0
0	0	0	0	0	0	0	0
0	0	0	0	0	0	0	0
0	0	0	0	0	0	0	0
0	0	0	0	0	0	0	0
0	0	0	0	0	0	0	0
0	0	0	0	0	0	0	0
0	0	0	0	0	0	0	0
0	0	0	0	0	0	0	0
0	0	0	0	0	0	0	0
0	0	0	0	0	0	0	0
0.5	0	0	0	0	0	0	0
0	0.455	0	0	0	0	0	0
0.1	0	0.588	0	0	0	0	0
0.2	0.227	0.118	1	0	0	0	0
0	0.318	0.294	0	1	0	0	0
0.2	0	0	0	0	1	0	0
0	0	0	0	0	0	1	0
0	0	0	0	0	0	0	1

5.5.2 Determination of Ambient Particle Size distribution using the Response Matrix

The determination of ambient size distribution of particles is achieved in two steps: (i) calculation of the actual number of particles in each size range at the detection point and (ii) determination of the relation between the detected particles at the measurement point and the particles in the atmosphere. Equation (5.5) gives matrix A, which is the number of particles at detection point for each size range (step i). The inverted response matrix, R^{-1} is multiplied by the instrument output matrix, I to determine matrix A.

The relation between the ambient aerosol size distribution and what is actually detected by the instrument is given by Equation (5.12). *f(Dp)* is the fraction of particles in the viewing volume that are the result of particle collision with the leading edge of the inlet. It is a function of particle size which is provided to the user of the instrument. In the example of 10 μm particle given earlier, *f(Dp)*=0.3. The radius of limiting trajectory circle is also available through the calculations of particle trajectories.

Table 5.6 shows R^{-1}, the inverse of the response matrix, R for the case under study. The matrix multiplication of matrix I into matrix R^{-1} gives matrix A. This is shown in Table 5.7.

Table 5.6 Inverse of response matrix, R^{-1} (1 of 4).

1.333	0	0	0	0	0	0	0
0	1.333	0	0	0	0	0	0
0	0	1.333	0	0	0	0	0
0	0	0	1.25	0	0	0	0
0	0	0	0	1.25	0	0	0
0	0	0	0	0	1.333	0	0
0	0	0	0	0	0	1.333	0
0	0	0	0	0	0	0	1.333
-0.1	0	0	0	0	0	0	0
0	-0.104	-0.104	0	0	0	0	0
0	0	0	-0.111	0	0	0	0
-0.11	-0.111	0	0	-0.11	-0.11	0	0
0	0	-0.104	-0.104	0	0	-0.1	0
0.009	0	0	0	-0.11	-0.22	0	-0.11
-0.23	-0.218	0.009	0	0	0	-0.23	0
0.009	0	-0.212	-0.097	-0.11	-0.11	0	-0.11
0.009	0.019	0.019	0.028	0.009	0.009	-0.1	0
0.017	0.009	0	0	0.018	0.027	0	-0.2
0.019	0.029	0.018	0.019	0.019	0.038	0.03	0.019
0.043	0.042	0.031	0.019	0.032	0.032	0.045	0.012
-0	-0.003	0.021	0.008	0.019	0.028	0.01	0.044
0.04	0.038	0.018	0.008	0.007	0.005	0.041	0.03
-0.01	-0.01	-0.008	-0.008	-0.01	-0.01	0.013	0.017
-0.01	-0.017	-0.015	-0.01	-0.01	-0.02	-0.02	-0.02
-0.01	-0.007	-0.007	-0.003	-0.01	-0.01	-0.01	-0.01
-0.01	-0.008	-0.01	-0.003	-0.01	-0.01	-0.02	-0.02
-0	-0.004	1E-04	0.002	0.003	0.005	-0.01	-0.01
0.009	0.009	0.009	0.005	0.008	0.01	0.013	0.013
0.007	0.007	0.007	0.003	0.006	0.007	0.012	0.011
-0	-0.001	-0.002	-0.001	-0	-0	-0	-0
-0	-0.005	-0.005	-0.002	-0	-0.01	-0.01	-0.01
1E-03	8E-04	-2E-05	-3E-04	-0	-0	0.002	0.002
0	0	0	0	0	0	0	0
0	0	0	0	0	0	0	0

Table 5.6 Inverse of response matrix, R^{-1} (2 of 4).

0	0	0	0	0	0	0	0
0	0	0	0	0	0	0	0
0	0	0	0	0	0	0	0
0	0	0	0	0	0	0	0
0	0	0	0	0	0	0	0
0	0	0	0	0	0	0	0
0	0	0	0	0	0	0	0
0	0	0	0	0	0	0	0
1.25	0	0	0	0	0	0	0
0	1.25	0	0	0	0	0	0
0	0	1.333	0	0	0	0	0
0	0	0	1.333	0	0	0	0
0	0	0	0	1.25	0	0	0
-0.111	0	0	0	0	1.333	0	0
0	-0.114	0	0	0	0	1.364	0
-0.106	0	-0.11	0	0	0	0	1.273
0	-0.114	-0.23	-0.11	-0.114	0	0	0
-0.097	0	0	-0.11	0	-0.11	0	0
0.019	-0.103	-0.11	0	-0.114	-0.23	-0.12	0
0.012	0.023	0.035	-0.25	-0.117	0	-0.14	-0.14
0.032	0.011	0.034	0.023	0.011	-0.11	0	-0.136
0.019	0.032	0.022	0.011	0.011	0.033	-0.25	-0.132
0.007	0.028	0.049	0.051	0.04	0.031	0.023	0.011
-0.015	0.012	0.008	0.039	0.041	0.067	0.075	0.066
-0.006	-0.006	-0.01	0.018	0.008	0.008	0.036	0.038
-0.012	-0.018	-0.03	0.027	0.006	0.009	0.042	0.064
-0.004	-0.016	-0.02	-0.02	-0.019	-0.03	0.043	0.017
0.009	0.004	0.009	-0.03	-0.016	-0.02	-0.05	-0.051
0.008	0.007	0.011	-0.01	-0.008	-0.01	-0.04	-0.04
-9E-04	0.004	0.004	0.009	0.008	0.011	0.001	0.005
-0.005	-0.003	-0.01	0.012	0.007	0.011	0.026	0.028
8E-04	0.003	0.004	0.005	0.004	0.005	-0.01	-0.003
0	0	0	0	0	0	0	0
0	0	0	0	0	0	0	0

Table 5.6 Inverse of response matrix, R^{-1} (3 of 4).

0	0	0	0	0	0	0	0
0	0	0	0	0	0	0	0
0	0	0	0	0	0	0	0
0	0	0	0	0	0	0	0
0	0	0	0	0	0	0	0
0	0	0	0	0	0	0	0
0	0	0	0	0	0	0	0
0	0	0	0	0	0	0	0
0	0	0	0	0	0	0	0
0	0	0	0	0	0	0	0
0	0	0	0	0	0	0	0
0	0	0	0	0	0	0	0
0	0	0	0	0	0	0	0
0	0	0	0	0	0	0	0
0	0	0	0	0	0	0	0
0	0	0	0	0	0	0	0
1.364	0	0	0	0	0	0	0
0	1.273	0	0	0	0	0	0
0	0	1.364	0	0	0	0	0
-0.14	0	0	1.545	0	0	0	0
-0.136	-0.136	0	0	1.5	0	0	0
0	-0.132	-0.13	0	0	1.455	0	0
-0.237	-0.124	-0.12	-0.124	0	0	1.364	0
0.054	0.041	-0.27	-0.281	-0.309	-0.14	0	1.545
0.026	0.026	0.012	-0.136	-0.15	-0.136	0	0
0.107	0.069	0.069	-0.253	-0.309	-0.14	-0.309	-0.15
0.053	0.058	0.096	0.084	0.056	-0.329	-0.364	-0.18
-0.053	-0.04	0.046	0.198	0.226	0.133	0.08	-0.36
-0.055	-0.042	0.015	0.133	0.162	0.142	0.155	-0.23
-0.005	-0.006	-0.04	-0.048	-0.045	0.035	0.073	0.164
0.033	0.025	-0.02	-0.102	-0.12	-0.084	-0.071	0.183
-0.011	-0.012	-0.02	-0.017	-0.011	0.066	0.073	0.036
0	0	0	0	0	0	0	0
0	0	0	0	0	0	0	0

Table 5.6 Inverse of response matrix, R^{-1} (4 of 4).

0	0	0	0	0	0	0	0	0	0
0	0	0	0	0	0	0	0	0	0
0	0	0	0	0	0	0	0	0	0
0	0	0	0	0	0	0	0	0	0
0	0	0	0	0	0	0	0	0	0
0	0	0	0	0	0	0	0	0	0
0	0	0	0	0	0	0	0	0	0
0	0	0	0	0	0	0	0	0	0
0	0	0	0	0	0	0	0	0	0
0	0	0	0	0	0	0	0	0	0
0	0	0	0	0	0	0	0	0	0
0	0	0	0	0	0	0	0	0	0
0	0	0	0	0	0	0	0	0	0
0	0	0	0	0	0	0	0	0	0
0	0	0	0	0	0	0	0	0	0
0	0	0	0	0	0	0	0	0	0
0	0	0	0	0	0	0	0	0	0
0	0	0	0	0	0	0	0	0	0
0	0	0	0	0	0	0	0	0	0
0	0	0	0	0	0	0	0	0	0
0	0	0	0	0	0	0	0	0	0
0	0	0	0	0	0	0	0	0	0
0	0	0	0	0	0	0	0	0	0
0	0	0	0	0	0	0	0	0	0
1.5	0	0	0	0	0	0	0	0	0
0	1.7	0	0	0	0	0	0	0	0
-0.2	0	2	0	0	0	0	0	0	0
-0.66	-0.44	0	2.2	0	0	0	0	0	0
-0.136	-0.51	-0.34	0	1.7	0	0	0	0	0
0.206	-0.04	-0.36	-0.5	-0.2	1	0	0	0	0
0.25	0.29	0.1	-0.7	-0.5	0	1	0	0	0
0.04	0	-0.4	0	0	0	0	1	0	0
0	0	0	0	0	0	0	0	1	0
0	0	0	0	0	0	0	0	0	1

Table 5.7 Calculation of matrix A, actual particle concentration at detection point in each size range from matrix I, instrument output in each size range.

Velocity Range	Matrix I Instrument Output in each velocity range
$104.81 \leq Vp < 105.14$	12
$104.46 \leq Vp < 104.81$	12
$104.09 \leq Vp < 104.46$	12
$103.7 \leq Vp < 104.09$	12
$103.28 \leq Vp < 103.7$	12
$102.83 \leq Vp < 103.28$	12
$102.35 \leq Vp < 102.83$	12
$101.84 \leq Vp < 102.35$	12
$101.29 \leq Vp < 101.84$	13
$100.69 \leq Vp < 101.29$	14
$100.06 \leq Vp < 100.69$	13
$99.38 \leq Vp < 100.06$	16
$98.65 \leq Vp < 99.38$	15
$97.86 \leq Vp < 98.65$	17
$97.02 \leq Vp < 97.86$	18
$96.12 \leq Vp < 97.02$	19
$95.15 \leq Vp < 96.12$	17
$94.13 \leq Vp < 95.15$	16
$93.04 \leq Vp < 94.13$	17
$91.89 \leq Vp < 93.04$	17
$90.63 \leq Vp < 91.89$	14
$89.27 \leq Vp < 90.63$	16
$87.78 \leq Vp < 89.27$	16
$86.17 \leq Vp < 87.78$	18
$84.48 \leq Vp < 86.17$	13
$82.74 \leq Vp < 84.48$	18
$81.08 \leq Vp < 82.74$	16
$79.38 \leq Vp < 81.08$	17
$77.85 \leq Vp < 79.38$	18
$76.39 \leq Vp < 77.85$	22
$74.88 \leq Vp < 76.39$	21
$73.17 \leq Vp < 74.88$	13
$71.49 \leq Vp < 73.17$	9
$70.34 \leq Vp < 71.49$	8

Size Range	Matrix A Actual number of particles detected by the instrument in each size range at sensor location
$33 \leq Dp < 34$	16
$32 \leq Dp < 33$	16
$31 \leq Dp < 32$	16
$30 \leq Dp < 31$	15
$29 \leq Dp < 30$	15
$28 \leq Dp < 29$	16
$27 \leq Dp < 28$	16
$26 \leq Dp < 27$	16
$25 \leq Dp < 26$	15
$24 \leq Dp < 25$	15
$23 \leq Dp < 24$	16
$22 \leq Dp < 23$	16
$21 \leq Dp < 22$	15
$20 \leq Dp < 21$	16
$19 \leq Dp < 20$	15
$18 \leq Dp < 19$	14
$17 \leq Dp < 18$	15
$16 \leq Dp < 17$	14
$15 \leq Dp < 16$	15
$14 \leq Dp < 15$	17
$13 \leq Dp < 14$	15
$12 \leq Dp < 13$	16
$11 \leq Dp < 12$	15
$10 \leq Dp < 11$	17
$9 \leq Dp < 10$	15
$8 \leq Dp < 9$	17
$7 \leq Dp < 8$	20
$6 \leq Dp < 7$	22
$5 \leq Dp < 6$	17
$4 \leq Dp < 5$	9
$3 \leq Dp < 4$	9
$2 \leq Dp \leq 3$	9
$1 \leq Dp \leq 2$	9
$0 < Dp \leq 1$	8

Knowing the true air speed of the aircraft and the geometry of the inlet, the ambient size distribution of the injected particles can be calculated. The radius of the diffuser at the entrance of the inlet is 0.005588 m, which corresponds to an area of 9.81×10^{-5} m^2. With the air speed of 113.6 ms^{-1}, the amount of air entering the nozzle or volumetric flow rate of air at diffuser entrance would be 1.1×10^{-2} $m^3 s^{-1}$, or 11 liters per second.

The 120 injected particles are distributed evenly in a circle of radius 0.0061. Therefore the area of injection circle would be 11.7×10^{-5} m^2. This means that each particle enters the inlet with 5.53×10^{-5} m^3/s of air. ($113.6 \times 11.7 \times 10^{-5} \times 0.5/120 = 5.53 \times 10^{-5}$). In other words, every 55.3 cc of air that passes through the diffuser entrance per second contains one particle. The injected particle concentration would then be equal to 1/55.3 or 0.018 particles per cc or about 18 particles per liter.

Table 5.8 shows the results of size distribution calculations for ACE-Asia inlet flying at 113.6 m/s at an ambient pressure of 53,000 Pa.

Comparison of the last two columns of Table 5.8 shows a close agreement between the calculations of ambient particle concentration from Equation (5.12) and the concentration of the injected particles.

Table 5.8 Determination of ambient aerosol size distribution using Equation (5.12) and comparison with known size distribution of injected particles.

Particle Size Range	N_1 Direct Particles	N_2 Collision Particles	A(Dp) Total Particles at Sensor	F(Dp)= N2/(N1+N2)	R_1 Limiting Trajectory Radius (m)	Concentration Equation (5.12) (# / m^3)	Concentration Injected Particles (# / m^3)
$33 \leq Dp < 34$	12	4	16	0.25	0.00194	17868.16	17946.90
$32 \leq Dp < 33$	12	4	16	0.25	0.00194	17868.16	17946.90
$31 \leq Dp < 32$	12	4	16	0.25	0.00194	17868.16	17946.90
$30 \leq Dp < 31$	12	3	15	0.20	0.00194	17868.16	17946.90
$29 \leq Dp < 30$	12	3	15	0.20	0.00193	18053.81	17946.90
$28 \leq Dp < 29$	12	4	16	0.25	0.00193	18053.81	17946.90
$27 \leq Dp < 28$	12	4	16	0.25	0.00193	18053.81	17946.90
$26 \leq Dp < 27$	12	4	16	0.25	0.00193	18053.81	17946.90
$25 \leq Dp < 26$	12	3	15	0.20	0.00192	18242.36	17946.90
$24 \leq Dp < 25$	12	3	15	0.20	0.00192	18242.36	17946.90
$23 \leq Dp < 24$	12	4	16	0.25	0.00191	18433.88	17946.90
$22 \leq Dp < 23$	12	4	16	0.25	0.00191	18433.88	17946.90
$21 \leq Dp < 22$	12	3	15	0.20	0.0019	18628.43	17946.90
$20 \leq Dp < 21$	12	4	16	0.25	0.0019	18628.43	17946.90
$19 \leq Dp < 20$	11	4	15	0.27	0.00189	17257.24	17946.90
$18 \leq Dp < 19$	11	3	14	0.21	0.00189	17257.24	17946.90
$17 \leq Dp < 18$	11	4	15	0.27	0.00188	17441.31	17946.90
$16 \leq Dp < 17$	11	3	14	0.21	0.00187	17628.35	17946.90
$15 \leq Dp < 16$	11	4	15	0.27	0.00186	17818.41	17946.90
$14 \leq Dp < 15$	11	6	17	0.35	0.00185	18011.56	17946.90
$13 \leq Dp < 14$	10	5	15	0.33	0.00184	16552.61	17946.90
$12 \leq Dp < 13$	11	5	16	0.31	0.00183	18407.41	17946.90
$11 \leq Dp < 12$	11	4	15	0.27	0.00182	18610.24	17946.90
$10 \leq Dp < 11$	11	6	17	0.35	0.00181	18816.45	17946.90
$9 \leq Dp < 10$	10	5	15	0.33	0.00179	17490.25	17946.90
$8 \leq Dp < 9$	10	7	17	0.41	0.00176	18091.59	17946.90
$7 \leq Dp < 8$	10	10	20	0.50	0.00176	18091.59	17946.90
$6 \leq Dp < 7$	10	12	22	0.55	0.00174	18509.88	17946.90
$5 \leq Dp < 6$	10	7	17	0.41	0.00173	18724.49	17946.90
$4 \leq Dp < 5$	9	0	9	0.00	0.00171	17168.13	17946.90
$3 \leq Dp < 4$	9	0	9	0.00	0.0017	17513.82	17946.90
$2 \leq Dp \leq 3$	9	0	9	0.00	0.00167	18106.40	17946.90
$1 \leq Dp \leq 2$	9	0	9	0.00	0.00164	18683.99	17946.90
$0 < Dp \leq 1$	8	0	8	0.00	0.00163	16977.96	17946.90

5.5.3 Determination of Size Measurement Resolution

The size measurement resolution is calculated for each particle size range. The results of these calculations are reflected in tables 5.3 through 5.9. In each case, the velocity of particles is plotted as a function of particle size and a polynomial equation is fit to the curve. The slope of the curve is calculated from dV/dDp. A velocity resolution of 0.2% was provided by the manufacturer of the velocimeter that is commercially available. The velocity measurement resolution is then determined as 0.2% of the calculated velocity for each particle size. The size measurement resolution is then calculated by dividing the velocity measurement resolution into the slope of the velocity vs. Dp curve.

$$\frac{dV}{dD_p} = \frac{Velocity\ \ measurement\ \ resolution}{Size\ \ measurement\ \ resolution} \tag{5.13}$$

Based on the data in tables 5.9-5.15 and the corresponding graphs following the tables for each specific case, the following points are concluded:

- PELTI diffuser functions better than ACE-Asia diffuser below 1.5 km altitude.
- Below 700 m, PELTI diffuser performance is marginal for particles smaller than 10 μm (based on slope of the velocity vs. Dp curve).
- There is adequate resolution to measure particles in the 1 to 30 μm range over the normal range of TAS for altitudes greater than ~1 km.

.

Table 5.9 Determination of size measurement resolution, PELTI, TAS=154.6 m/s, P=45,778 Pa.

Dp (μm)	Velocity (m/s)	dV/dDp	Velocity Measurement Resolution (m/s)	Size Measurement Resolution (μm)	Velocity Measurement Resolution (%)	Size Measurement Resolution (%)
1	103.14	2.6035	0.206	0.079	0.2	7.923
2	105.36	2.5227	0.211	0.084	0.2	4.176
4	110.4	2.3611	0.221	0.094	0.2	2.338
6	114.22	2.1995	0.228	0.104	0.2	1.731
8	118.62	2.0379	0.237	0.116	0.2	1.455
10	123.14	1.8763	0.246	0.131	0.2	1.313
15	131.93	1.4723	0.264	0.179	0.2	1.195
20	137.76	1.0683	0.276	0.258	0.2	1.290
25	141.71	0.6643	0.283	0.427	0.2	1.707
30	144.41	0.2603	0.289	1.110	0.2	3.699

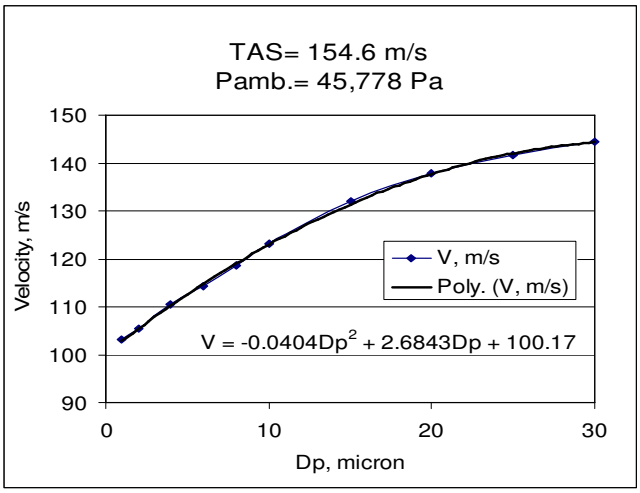

Figure 5.4 Vp as a function of Dp for PELTI, TAS=154.6 m/s, P=45,778 Pa.

Table 5.10 Determination of size measurement resolution, ACE-Asia, TAS=113.6 m/s, P=53,000 Pa.

Dp (μm)	Velocity (m/s)	dV/dDp	Velocity Measurement Resolution (m/s)	Size Measurement Resolution (μm)	Velocity Measurement Resolution (%)	Size Measurement Resolution (%)
1	70.34	1.9015	0.141	0.074	0.2	7.398
2	71.44	1.8511	0.143	0.077	0.2	3.859
4	74.88	1.7503	0.150	0.086	0.2	2.139
6	77.85	1.6495	0.156	0.094	0.2	1.573
8	81.01	1.5487	0.162	0.105	0.2	1.308
10	84.48	1.4479	0.169	0.117	0.2	1.167
15	91.89	1.1959	0.184	0.154	0.2	1.025
20	97.02	0.9439	0.194	0.206	0.2	1.028
25	100.69	0.6919	0.201	0.291	0.2	1.164
30	103.28	0.4399	0.207	0.470	0.2	1.565

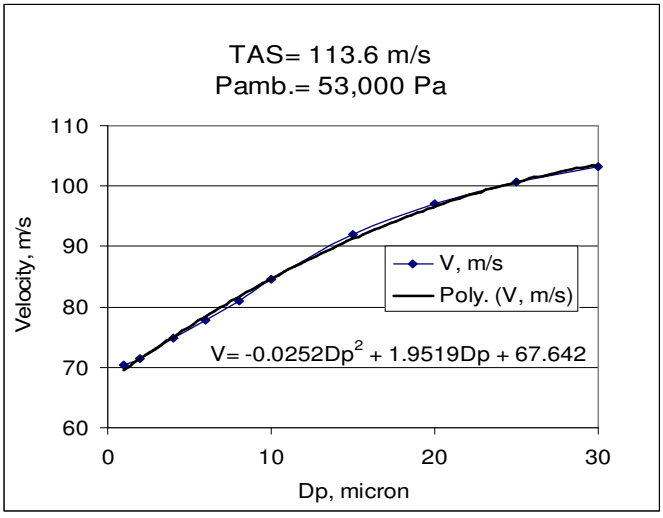

Figure 5.5 Vp as a function of Dp for ACE-Asia, TAS=113.6 m/s, P=53,000 Pa.

.Table 5.11 Determination of size measurement resolution, PELTI, TAS=140.3 m/s, P=53,379 Pa.

Dp (μm)	Velocity (m/s)	dV/dDp	Velocity Measurement Resolution (m/s)	Size Measurement Resolution (μm)	Velocity Measurement Resolution (%)	Size Measurement Resolution (%)
1	100.56	1.924	0.201	0.105	0.2	10.453
2	102.63	1.8638	0.205	0.110	0.2	5.506
4	107.37	1.7434	0.215	0.123	0.2	3.079
6	110.03	1.623	0.220	0.136	0.2	2.260
8	112.82	1.5026	0.226	0.150	0.2	1.877
10	115.8	1.3822	0.232	0.168	0.2	1.676
15	122.16	1.0812	0.244	0.226	0.2	1.506
20	126.53	0.7802	0.253	0.324	0.2	1.622
25	129.57	0.4792	0.259	0.541	0.2	2.163
30	131.74	0.1782	0.263	1.479	0.2	4.929

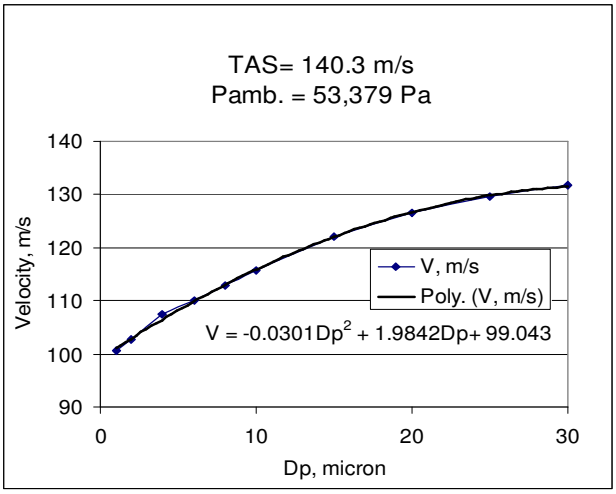

Figure 5.6 Vp as a function of Dp for PELTI, TAS=140.3 m/s, P=53,379 Pa.

Table 5.12 Determination of size measurement resolution, PELTI, TAS=120.4 m/s, P=74,920 Pa.

Dp (μm)	Velocity (m/s)	dV/dDp	Velocity Measurement Resolution (m/s)	Size Measurement Resolution (μm)	Velocity Measurement Resolution (%)	Size Measurement Resolution (%)
1	85.46	1.4894	0.171	0.115	0.2	11.476
2	86.85	1.448	0.174	0.120	0.2	5.998
4	90.41	1.3652	0.181	0.132	0.2	3.311
6	92.65	1.2824	0.185	0.144	0.2	2.408
8	94.79	1.1996	0.190	0.158	0.2	1.975
10	97.15	1.1168	0.194	0.174	0.2	1.740
15	102.5	0.9098	0.205	0.225	0.2	1.502
20	106.43	0.7028	0.213	0.303	0.2	1.514
25	109.32	0.4958	0.219	0.441	0.2	1.764
30	111.43	0.2888	0.223	0.772	0.2	2.572

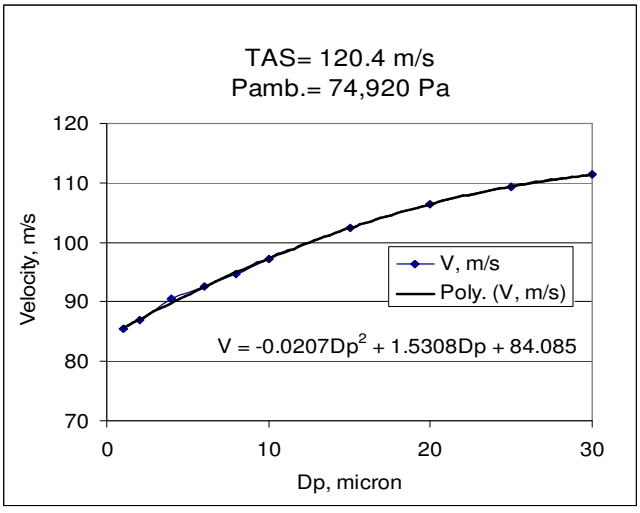

Figure 5.7 Vp as a function of Dp for PELTI, TAS=120.4 m/s, P=74,920 Pa.

.

Table 5.13 Determination of size measurement resolution, ACE-Asia, TAS=113.6 m/s, P=84,600 Pa.

Dp (μm)	Velocity (m/s)	dV/dDp	Velocity Measurement Resolution (m/s)	Size Measurement Resolution (μm)	Velocity Measurement Resolution (%)	Size Measurement Resolution (%)
1	100.01	2.6217	0.200	0.076	0.2	7.629
2	102.00	2.0726	0.204	0.098	0.2	4.921
4	106.42	1.1982	0.213	0.178	0.2	4.441
6	107.91	0.5902	0.216	0.366	0.2	6.095
8	107.72	0.2102	0.215	1.025	0.2	12.812
10	107.54	0.0198	0.215	10.863	0.2	108.626
15	108.43	0.1213	0.217	1.788	0.2	11.919
20	109.82	0.5678	0.220	0.387	0.2	1.934
25	110.96	0.7593	0.222	0.292	0.2	1.169
30	111.75	0.0958	0.224	2.333	0.2	7.777

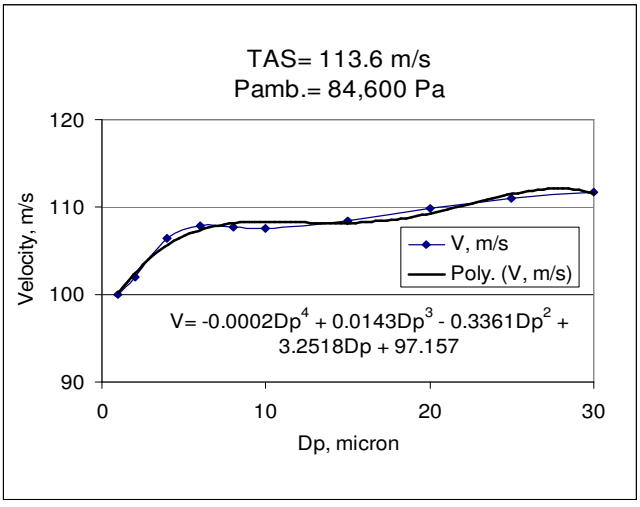

Figure 5.8 Vp as a function of Dp for ACE-Asia, TAS=113.6 m/s, P=84,600 Pa.

Table 5.14 Determination of size measurement resolution, PELTI, TAS=119.2 m/s, P=86,168 Pa.

Dp (μm)	Velocity (m/s)	dV/dDp	Velocity Measurement Resolution (m/s)	Size Measurement Resolution (μm)	Velocity Measurement Resolution (%)	Size Measurement Resolution (%)
1	90.83	1.1792	0.182	0.154	0.2	15.405
2	92.32	1.1448	0.185	0.161	0.2	8.064
4	95.95	1.076	0.192	0.178	0.2	4.459
6	97.79	1.0072	0.196	0.194	0.2	3.236
8	99	0.9384	0.198	0.211	0.2	2.637
10	100.51	0.8696	0.201	0.231	0.2	2.312
15	104.45	0.6976	0.209	0.299	0.2	1.996
20	107.53	0.5256	0.215	0.409	0.2	2.046
25	109.83	0.3536	0.220	0.621	0.2	2.485
30	111.54	0.1816	0.223	1.228	0.2	4.095

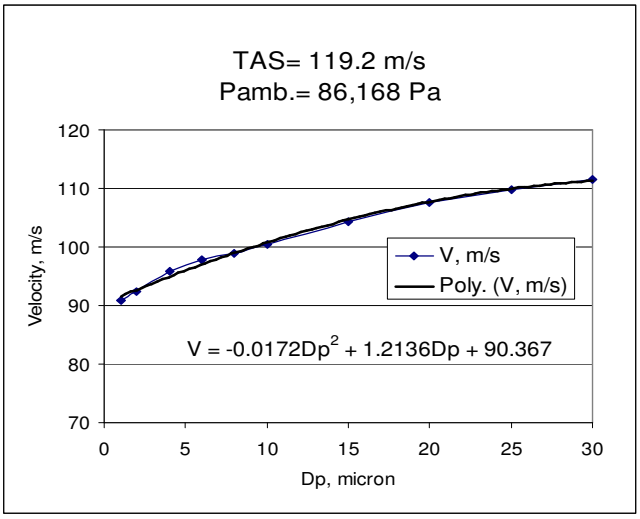

Figure 5.9 Vp as a function of Dp for PELTI, TAS=119.2 m/s, P=86,168 Pa.

Table 5.15 Determination of size measurement resolution, PELTI, TAS=115.6 m/s, P=93,521 Pa.

Dp (μm)	Velocity (m/s)	dV/dDp	Velocity Measurement Resolution (m/s)	Size Measurement Resolution (μm)	Velocity Measurement Resolution (%)	Size Measurement Resolution (%)
1	94.29	1.2682	0.189	0.149	0.2	14.870
2	96.6	1.183	0.193	0.163	0.2	8.166
4	100.31	1.0234	0.201	0.196	0.2	4.901
6	101.03	0.8782	0.202	0.230	0.2	3.835
8	101.73	0.7474	0.203	0.272	0.2	3.403
10	102.91	0.631	0.206	0.326	0.2	3.262
15	106.06	0.403	0.212	0.526	0.2	3.509
20	108.39	0.265	0.217	0.818	0.2	4.090
25	110.01	0.217	0.220	1.014	0.2	4.056
30	111.15	0.259	0.222	0.858	0.2	2.861

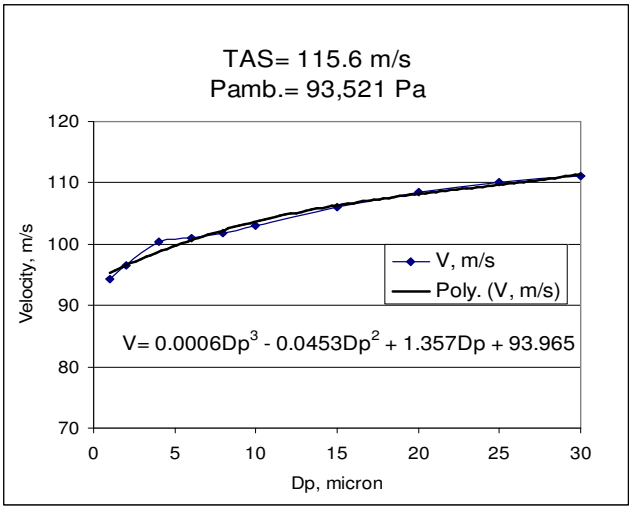

Figure 5.10 Vp as a function of Dp for PELTI, TAS=115.6 m/s, P=93,521 Pa.

Chapter 6. Enhancement Factors for the LTI Used in ACE Asia: A new Geometry

6.1 Introduction

The low turbulence aerosol inlet (LTI), Figure 6.1, was developed at the University of Denver. It primarily consists of a porous, conical diffuser followed by a 65° bend. The LTI is used on aircraft to sample particles from the atmosphere and transport those sampled particles to measuring instruments for further analysis of particle properties.

The axis of the diffuser points into the airflow around the aircraft in flight. The LTI reduces the velocity of the sampled air from the true airspeed of the aircraft to a few meters a second over a distance of 14 cm. This slowing is done in laminar flow due to the suction of nearly 80% of the flow through the porous diffuser (Wilson et al., 2004). Maintaining laminar flow in this region reduces turbulent deposition of super-micron particles on the wall of the inlet. (Huebert et.al, 2004). This is the principle contribution of the LTI. Since the turbulent deposition of particles is unquantifiable, the LTI permits the quantitative sampling of super-micron particles from aircraft.

Because of particle inertia and the bending of streamlines resulting from the flow in and through the diffuser, the LTI enhances the mixing ratio (number of particles per unit mass of air) of large particles in the process of sampling, slowing and transport. The enhancement factor is a function of particle size and density and permits the mixing ratio measured in the aircraft to be related accurately to the ambient mixing ratio.

The enhancement factor, EF is defined as:

$$EF = \frac{Mixing\ ratio\ of\ particles\ at\ exit}{Mixing\ ratio\ of\ particles\ at\ entrance} \tag{6.1}$$

$$EF = \frac{\#\ of\ Particles\ per\ unit\ mass\ of\ air\ at\ exit}{\#\ of\ Particles\ per\ unit\ mass\ of\ air\ at\ entrance} \tag{6.2}$$

It is very important for the sampled air to be a good representative of the ambient air in the atmosphere, in order to gain an accurate knowledge of the atmosphere.

The aerosol sample that enters the instrument can differ from the aerosol in the free stream due to the consequences of particle inertia and the bending of sampled streamlines, turbulence generated in sampling and slowing the flow or heating that occurs while slowing the air (Wilson and Seebaugh, 2001). All of the sampling instruments alter the characteristics of the aerosol particles in the process of slowing the flow and changing the thermodynamic properties of the air as well as the particles. Therefore, the need to quantify these changes is an essential part of the sampling. The thermodynamic changes are not addressed here since they require the chemical information concerning the particles.

This chapter deals with the determination of the enhancement factor in ACE-Asia inlet. ACE-Asia refers to Aerosol Characterization Experiment in Asian Pacific region, 2000. The details of the low turbulence inlet geometry and its function are explained in Chapter 3. LTI reduces the ambient air velocity from about 100 ms^{-1} to 4-5 ms^{-1} in a relatively short distance by boundary layer suction. The air velocity reduction is accompanied by a laminar flow status, which eliminates the effect of particle loss by turbulence deposition of particles to the walls of the diffuser. The calculation of laminar

flow and particle trajectories in computational fluid dynamics is much more accurate and reliable than the turbulence modeling. The flow in the diffuser is modeled using Fluent. Figure 6.1 shows the LTI used in ACE-Asia.

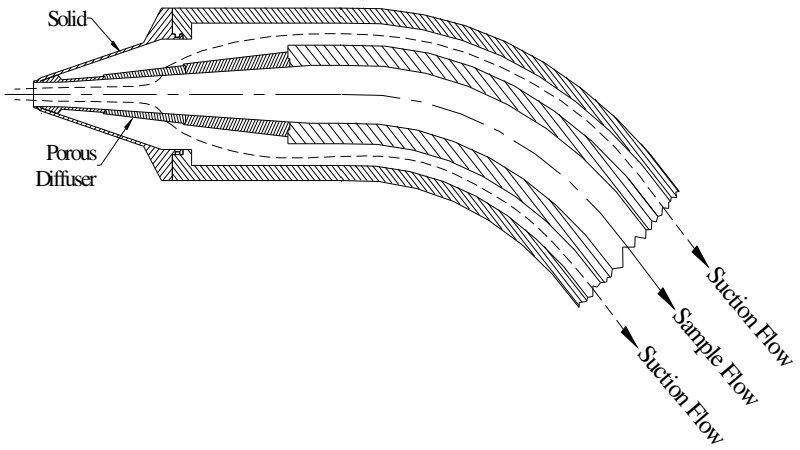

Figure 6.1 Schematic diagram of LTI used in ACE-Asia (Wilson et. al, 2004).

Two different models, one considering the flow of air inside the diffuser, and the other one considering the flow of air inside the diffuser as well as the external flow of air around the inlet are generated in Fluent. These two models are referred to internal and total flows respectively. The results of the enhancement factor determination in internal and total flows show a close agreement (Figure 6.7), which justifies the use of internal flow in further calculations to minimize the computational resources.

The enhancement factor of the particles is calculated in two different approaches, the limiting trajectory method and the direct injection method. The former method used the flow of air inside and around the diffuser (total flow), while the later method used the flow of air inside the diffuser (internal flow).

Particles of two different densities (ρ= 1,550 kgm^{-3} and ρ= 1,000 kgm^{-3}) in the size range of 1-15 μm, are injected to the flow through the leading edge of the inlet.

The determination of the enhancement factor using the method of limiting trajectory is carried by injecting a single particle from a distance 40 cm from the entrance to the inlet, while the determination of enhancement factor using the method of direct injection is achieved by injecting 999 equally spaced particles right at the inlet entrance.

The users of LTI can use the results of enhancement factor calculations to determine the actual ambient aerosol mixing ratio from the mixing ratio that they have measured with their instruments.

6.2 Determination of Enhancement Factor in LTI using Total Flow Simulation

The limiting trajectory approach is used to determine the enhancement factor of the particles in total flow. The flow field inside and around the inlet is determined by solving the equations of continuity and momentum for compressible steady flow conditions. The particles are then injected to the flow one at a time at a distance 0.4 m from the entrance to the inlet. This distance is about the farthest the ambient air around the inlet is modeled.

The limiting trajectory method determines the enhancement of particles by assigning one limiting trajectory tube of a specific radius to each particle size. The limiting trajectory tube is an imaginary tube of air if the space, whose aerosol particles end up in the sample flow at the exit of the instrument. Knowing the radius of this imaginary circle and knowing the velocity of air entering this tube, the total amount of air carrying the sample flow particles is calculated. This is referred to mass flow rate at the entrance to the inlet. The same logic can be used to determine the amount of air exiting

the instrument carrying all the particles of the sample flow. Knowing the geometry of the inlet and the velocity of air at the exit point, the mass flow rate at the exit of the diffuser is determined. Since the same number of particles that were present in the limiting trajectory tube end up in the exit flow, the ratio of the mass flow rate at the exit to the mass flow rate at the entrance determines the enhancement factor for a specific particle size. Figure 6.2 illustrates the idea of the limiting trajectory method in a simple sketch.

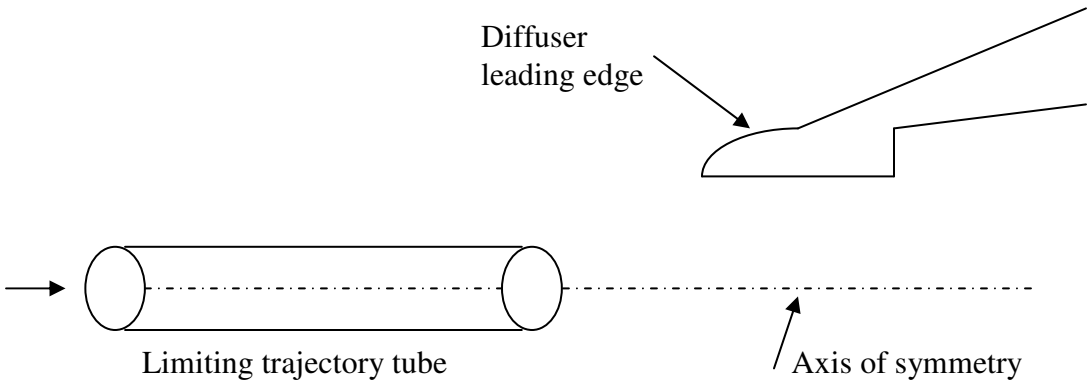

Figure 6.2 Illustration of limiting trajectory technique for determination of enhancement factor.

To determine the radius of the limiting trajectory tube the following procedure is implemented: Starting from the centerline of the inlet and working towards the inlet internal wall, one particle from each size range is injected to the flow and the trajectory of that single particle is recorded in a file. The injection point of the same particle is changed in small increments and the trajectory of that particle is recorded for all of the single injections. Each particle can either pass through the exit of the diffuser or trap somewhere along the path. The y-coordinates of the injection point of the last particle that enters the sample flow through the exit of the inlet is the radius of the limiting

trajectory tube. The mass flow rate of air through the limiting trajectory tube and at the exit of the inlet is given by:

$$\dot{m}_{entrance} = \rho_a v_a A_L \tag{6.3}$$

$$\dot{m}_{exit} = \rho_e v_e A_c \tag{6.4}$$

$\dot{m}_{entrance}$ refers to the mass flow rate through the limiting trajectory tube, ρ_a is the ambient air density, v_a the ambient air velocity and A_L is the cross sectional area of the limiting trajectory tube. The exit terms in equation (6.4) refers to the same variables at the exit of the inlet, also known as the core flow. A_c is the area of the core flow at the exit of the diffuser. The mass flow rate at the core exit is calculated by Fluent. It can be altered by changing the amount of air removed through the suction outlet.

In general, the enhancement factor can be calculated from Equation (6.1). However, since the number of particles passing through the limiting trajectory tube is equal to the number of the particles in the sample flow, Equation (6.1) can be simplified to Equation (6.5), which defines the enhancement factor of the particles as the ratio of mass flow rate inside the limiting trajectory tube to the mass flow rate at the core exit:

$$EF = \frac{\dot{m}_{entrance}}{\dot{m}_{exit}} \tag{6.5}$$

The enhancement factor is a function of particle diameter, particle density, flow conditions and inlet geometry. All these variables are reflected in the Stokes number of the particles given by:

$$Stk = \frac{\rho_p V D_p^{\,2} C_c}{9 \mu d} \tag{6.6}$$

ρ_p is the particle density, V is the velocity of air at straight section of the throat, D_p the particle diameter, C_c is the slip correction factor, μ is the air viscosity at straight section of the throat and d the inlet throat diameter.

In the determination of Stokes number, the temperature and pressure dependence of slip correction factor and temperature dependence of viscosity of air are considered, but in Fluent calculations the viscosity of air is assumed to be constant all over the domain.

Five total cases have been analyzed in this section. The inlet geometry, ambient air properties, aircraft speed, particle density and the flight altitude are the same for all the cases, but the mass flow rate of air passing through the core exit is altered (from 0.099 to 0.297). The aircraft true air speed = 113.6 ms^{-1}, ambient pressure = 53,000 Pa, corresponding to flight altitude of ~ 5 km and the particle density = 1,000 kgm^{-3}.

The results of Fluent calculations and particle trajectories to determine the enhancement factor as a function of Stokes number in total flow models are summarized in Tables 6.1 through 6.5.

Table 6.1 Determination of EF for "Total Case" ACE-Asia, LTI_v2_5_coreratio_0.1.cas
TAS=113.6 ms^{-1}, P=53,000 Pa, ρ= 1,000 kgm^{-3}, core mass flow ratio= 0.099

Particle Size (Micron)	Slip Correction Factor (Cc)	Stokes Number	Radius of Limiting Trajectory Circle (mm)	Mass Flow Rate at Entrance (kg/s)	Mass Flow Rate at Exit (kg/s)	Enhancement Factor (EF)
1	1.28	0.08	1.69	0.0007	0.0008	0.98
2	1.14	0.30	1.72	0.0008	0.0008	1.02
3	1.09	0.64	1.78	0.0008	0.0008	1.09
4	1.07	1.12	1.85	0.0009	0.0008	1.18
5	1.06	1.72	1.96	0.0010	0.0008	1.32
6	1.05	2.46	2.04	0.0011	0.0008	1.43
7	1.04	3.33	2.12	0.0012	0.0008	1.55
8	1.04	4.33	2.22	0.0013	0.0008	1.69
9	1.03	5.45	2.32	0.0014	0.0008	1.85
10	1.03	6.71	2.41	0.0015	0.0008	2.00
11	1.03	8.10	2.51	0.0016	0.0008	2.17
12	1.02	9.62	2.61	0.0018	0.0008	2.34
13	1.02	11.27	2.75	0.0019	0.0008	2.59
14	1.02	13.06	2.93	0.0022	0.0008	2.95
15	1.02	14.97	3.12	0.0025	0.0008	3.34

Table 6.2 Determination of EF for "Total Case" ACE-Asia, LTI_v2_5_coreratio_0.13.cas TAS=113.6 ms^{-1}, P=53,000 Pa, ρ= 1,000 kgm^{-3}, core mass flow ratio= 0.131

Particle Size (Micron)	Slip Correction Factor (Cc)	Stokes Number	Radius of Limiting Trajectory Circle (mm)	Mass Flow Rate at Entrance (kg/s)	Mass Flow Rate at Exit (kg/s)	Enhancement Factor (EF)
1	1.28	0.08	1.96	0.0010	0.0010	1.01
2	1.14	0.29	2.00	0.0010	0.0010	1.05
3	1.09	0.63	2.05	0.0011	0.0010	1.11
4	1.07	1.10	2.12	0.0012	0.0010	1.18
5	1.06	1.69	2.19	0.0012	0.0010	1.26
6	1.05	2.41	2.27	0.0013	0.0010	1.36
7	1.04	3.27	2.36	0.0014	0.0010	1.46
8	1.03	4.24	2.44	0.0015	0.0010	1.56
9	1.03	5.35	2.50	0.0016	0.0010	1.65
10	1.03	6.59	2.63	0.0018	0.0010	1.82
11	1.03	7.95	2.77	0.0020	0.0010	2.03
12	1.02	9.44	2.94	0.0022	0.0010	2.28
13	1.02	11.06	3.11	0.0025	0.0010	2.54
14	1.02	12.81	3.27	0.0028	0.0010	2.82
15	1.02	14.69	3.44	0.0031	0.0010	3.11

Table 6.3 Determination of EF for "Total Case" ACE-Asia, LTI_v2_5.cas.
TAS=113.6 ms^{-1}, P=53,000 Pa, ρ= 1,000 kgm^{-3}, core mass flow ratio= 0.167

Particle Size (Micron)	Slip Correction Factor (Cc)	Stokes Number	Radius of Limiting Trajectory Circle (mm)	Mass Flow Rate at Entrance (kg/s)	Mass Flow Rate at Exit (kg/s)	Enhancement Factor (EF)
1	1.28	0.07	2.04	0.0011	0.0011	0.97
2	1.14	0.26	2.08	0.0011	0.0011	1.00
3	1.09	0.56	2.13	0.0012	0.0011	1.05
4	1.07	0.97	2.19	0.0012	0.0011	1.11
5	1.06	1.49	2.24	0.0013	0.0011	1.16
6	1.05	2.13	2.31	0.0014	0.0011	1.23
7	1.04	2.88	2.41	0.0015	0.0011	1.34
8	1.03	3.74	2.51	0.0016	0.0011	1.46
9	1.03	4.72	2.63	0.0018	0.0011	1.60
10	1.03	5.81	2.78	0.0020	0.0011	1.79
11	1.03	7.01	2.93	0.0022	0.0011	1.99
12	1.02	8.33	3.09	0.0025	0.0011	2.21
13	1.02	9.75	3.20	0.0026	0.0011	2.38
14	1.02	11.30	3.35	0.0029	0.0011	2.60
15	1.02	12.95	3.51	0.0032	0.0011	2.85

Table 6.4 Determination of EF for "Total Case" ACE-Asia, Total_1691_7624.cas. TAS=113.6 ms^{-1}, P=53,000 Pa, ρ= 1,000 kgm^{-3}, core mass flow ratio= 0.182

Particle Size (Micron)	Slip Correction Factor (Cc)	Stokes Number	Radius of Limiting Trajectory Circle (mm)	Mass Flow Rate at Entrance (kg/s)	Mass Flow Rate at Exit (kg/s)	Enhancement Factor (EF)
1	1.29	0.11	2.55	0.0017	0.0017	0.98
2	1.14	0.38	2.67	0.0018	0.0017	1.07
3	1.10	0.83	2.73	0.0019	0.0017	1.12
4	1.07	1.44	2.84	0.0021	0.0017	1.21
5	1.06	2.22	2.96	0.0022	0.0017	1.31
6	1.05	3.17	3.08	0.0024	0.0017	1.42
7	1.04	4.29	3.21	0.0026	0.0017	1.55
8	1.04	5.57	3.35	0.0029	0.0017	1.69
9	1.03	7.02	3.50	0.0031	0.0017	1.84
10	1.03	8.64	3.66	0.0034	0.0017	2.01
11	1.03	10.43	3.82	0.0037	0.0017	2.19
12	1.02	12.39	3.99	0.0041	0.0017	2.39
13	1.02	14.51	4.17	0.0044	0.0017	2.61
14	1.02	16.81	4.39	0.0049	0.0017	2.90
15	1.02	19.27	4.59	0.0054	0.0017	3.17

Table 6.5 Determination of EF for "Total Case" ACE-Asia, LTI_v2_3.cas.
TAS=113.6 ms^{-1}, P=53,000 Pa, ρ= 1,000 kgm^{-3}, core mass flow ratio= 0.297

Particle Size (Micron)	Slip Correction Factor (Cc)	Stokes Number	Radius of Limiting Trajectory Circle (mm)	Mass Flow Rate at Entrance (kg/s)	Mass Flow Rate at Exit (kg/s)	Enhancement Factor (EF)
1	1.28	0.08	2.98	0.0023	0.0023	1.00
2	1.14	0.30	3.03	0.0024	0.0023	1.04
3	1.09	0.65	3.10	0.0025	0.0023	1.09
4	1.07	1.13	3.19	0.0026	0.0023	1.15
5	1.06	1.75	3.26	0.0027	0.0023	1.20
6	1.05	2.49	3.34	0.0029	0.0023	1.26
7	1.04	3.37	3.43	0.0030	0.0023	1.33
8	1.04	4.38	3.60	0.0033	0.0023	1.46
9	1.03	5.53	3.77	0.0037	0.0023	1.61
10	1.03	6.80	3.89	0.0039	0.0023	1.71
11	1.03	8.21	3.99	0.0041	0.0023	1.80
12	1.02	9.75	4.17	0.0045	0.0023	1.97
13	1.02	11.43	4.45	0.0051	0.0023	2.23
14	1.02	13.23	4.51	0.0052	0.0023	2.29
15	1.02	15.17	4.61	0.0055	0.0023	2.40

Figure 6.3 shows the enhancement factor as a function of Stokes number for unit density super-micron particles in 1-15 μm diameter range for total cases with core mass flow ratios in the range of 0.099-0.297.

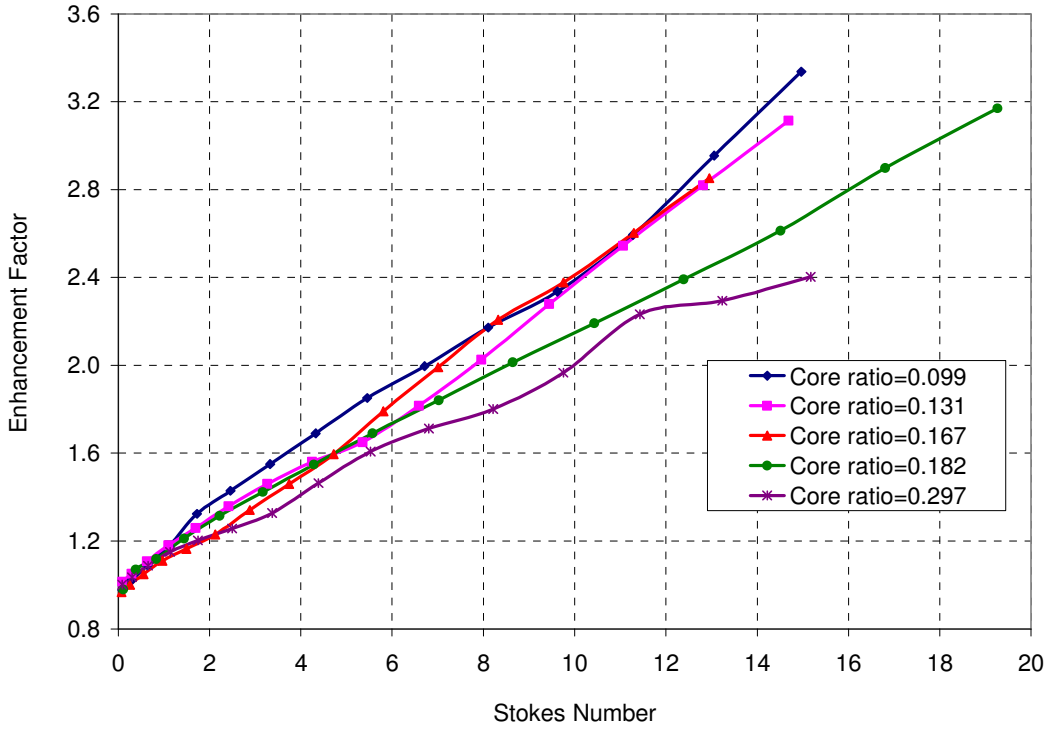

Figure 6.3 Enhancement factor as a function of Stokes number for ACE-Asia, total cases, TAS=113.6 ms^{-1}, P=53,000 Pa, ρ= 1,000 kgm^{-3}, core mass flow ratio range 0.099-0.297.

The core mass flow ratio of 0.099 and 0.297 corresponds to the suction flow rates of 90% and 70% respectively. As it is obvious from the graph, the enhancement factor decreases as the core mass flow ratio increases for the same stokes number.

The range of core mass flow ratios calculated in this study (0.099-0.297) covers the range of core mass flow ratios in actual cruise C-130 flights (0.18 to 0.26).

6.3 Determination of Enhancement Factor in LTI using Internal Flow Simulation

In this section, the enhancement factor of the particles is determined by calculating the particle trajectories in internal flow models. The flow inside the inlet is modeled in Fluent. The internal flow modeling reduces the computational resources required to run the model considerably. In order to calculate the particle enhancement factor using the internal flow simulations, the direct injection method is applied. In this method, 999 unit density particles in the range of 1-15 μm are injected to the flow at the inlet entrance all at once. The radial distribution of particles is uniform across the entrance.

The particle trajectories are calculated by Fluent and the numbers of particles that show up in the sample flow through the core exit are determined for each particle size. The larger particles can stay in the domain for a longer period of time and therefore have a higher chance to be present in the sample flow.

The number of particles per unit mass of air exiting the rear of the diffuser defines the mixing ratio of particles at the exit. The number of particles per unit mass of air at the entrance determines the mixing ratio of particles at entrance.

The mixing ratio of particles at the exit is divided by the mixing ratio of particles at entrance to determine the enhancement factor of particles by the direct injection method.

Six internal cases have been analyzed in this section. In each case, the mixing ratio is calculated at inlet entrance and core exit. Particles in the range of 1-15 microns are injected to the flow and the number of particles that escaped the domain through the core outlet is recorded in each case. Fluent calculates the air mass flow rate at the

entrance and exit of the inlet. Knowing the number of particles at entrance and exit, the mixing ratio of particles at each of these two locations are calculated (Equations 6.1 and 6.2)

The inlet geometry, ambient air properties, aircraft speed, particle density and the flight altitude are the same for all the cases, but the mass flow rate of air passing through the core exit is altered (from 0.04 to 0.32). The aircraft true air speed = 113.6 ms^{-1}, ambient pressure = 53,000 Pa, corresponding to flight altitude of ~ 5 km and the particle density = 1,000 kgm^{-3}.

The results of Fluent calculations and particle trajectories to determine the enhancement factor as a function of Stokes number in internal flow models are summarized in Tables 6.6 through 6.11.

Table 6.6 Determination of EF for "Internal Case" ACE-Asia, 400_9415.cas. TAS=113.6 ms^{-1}, P=53,000 Pa, ρ= 1,000 kgm^{-3}, core mass flow ratio= 0.04, number of particles injected=999, mass flow rate at entrance=0.0098 kg/s, mass flow rate at exit =0.0004 kg/s (Fluent results).

Particle Size (Micron)	Stokes Number	# of Particles in Core Flow	Mass Flow Rate at Entrance (kg/s)	Mass Flow Rate at Exit (kg/s)	Mixing Ratio of Particles at Entrance	Mixing Ratio of Particles at Exit	Enhancement Factor (EF)
1	0.09	42	0.0098	0.0004	101,783	105,000	1.03
2	0.32	43	0.0098	0.0004	101,783	107,500	1.06
3	0.70	47	0.0098	0.0004	101,783	117,500	1.15
4	1.22	51	0.0098	0.0004	101,783	127,500	1.25
5	1.89	56	0.0098	0.0004	101,783	140,000	1.38
6	2.69	62	0.0098	0.0004	101,783	155,000	1.52
7	3.65	69	0.0098	0.0004	101,783	172,500	1.69
8	4.74	77	0.0098	0.0004	101,783	192,500	1.89
9	5.98	87	0.0098	0.0004	101,783	217,500	2.14
10	7.36	99	0.0098	0.0004	101,783	247,500	2.43
15	16.44	194	0.0098	0.0004	101,783	485,000	4.77

The mixing ratio of particles at entrance is the total number of particles that are injected to the flow divided by the mass flow rate of air at entrance. The mixing ratio of particles at exit is the number of particles that are sampled in the core flow divided by the mass flow rate of air at core exit. Enhancement factor is the mixing ratio of particles at exit divided by the mixing ratio of particles at entrance.

Table 6.7 Determination of EF for "Internal Case" ACE-Asia, 864_6786.cas. TAS=113.6 ms^{-1}, P=53,000 Pa, ρ= 1,000 kgm^{-3}, core mass flow ratio= 0.11, number of particles injected=999, mass flow rate at entrance=0.0077 kg/s, mass flow rate at exit =0.0009 kg/s (Fluent results).

Particle Size (Micron)	Stokes Number	# of Particles in Core Flow	Mass Flow Rate at Entrance (kg/s)	Mass Flow Rate at Exit (kg/s)	Mixing Ratio of Particles at Entrance	Mixing Ratio of Particles at Exit	Enhancement Factor (EF)
1	0.11	115	0.0077	0.0009	130,588	133,102	1.02
2	0.38	120	0.0077	0.0009	130,588	138,889	1.06
3	0.80	128	0.0077	0.0009	130,588	148,148	1.13
4	1.39	138	0.0077	0.0009	130,588	159,722	1.22
5	2.15	152	0.0077	0.0009	130,588	175,926	1.35
6	3.06	167	0.0077	0.0009	130,588	193,287	1.48
7	4.13	186	0.0077	0.0009	130,588	215,278	1.65
8	5.36	208	0.0077	0.0009	130,588	240,741	1.84
9	6.76	234	0.0077	0.0009	130,588	270,833	2.07
10	8.31	262	0.0077	0.0009	130,588	303,241	2.32
15	18.51	485	0.0077	0.0009	130,588	561,343	4.30

Table 6.8 Determination of EF for "Internal Case" ACE-Asia, 1881_9060.cas. TAS=113.6 ms^{-1}, P=53,000 Pa, ρ= 1,000 kgm^{-3}, core mass flow ratio= 0.17, number of particles injected=999, mass flow rate at entrance=0.0109 kg/s, mass flow rate at exit =0.0019 kg/s (Fluent results).

Particle Size (Micron)	Stokes Number	# of Particles in Core Flow	Mass Flow Rate at Entrance (kg/s)	Mass Flow Rate at Exit (kg/s)	Mixing Ratio of Particles at Entrance	Mixing Ratio of Particles at Exit	Enhancement Factor (EF)
1	0.08	174	0.0109	0.0019	91,308	92,504	1.01
2	0.29	182	0.0109	0.0019	91,308	96,757	1.06
3	0.62	191	0.0109	0.0019	91,308	101,542	1.11
4	1.09	202	0.0109	0.0019	91,308	107,390	1.18
5	1.69	218	0.0109	0.0019	91,308	115,896	1.27
6	2.42	236	0.0109	0.0019	91,308	125,465	1.37
7	3.27	256	0.0109	0.0019	91,308	136,098	1.49
8	4.26	280	0.0109	0.0019	91,308	148,857	1.63
9	5.38	305	0.0109	0.0019	91,308	162,148	1.78
10	6.62	333	0.0109	0.0019	91,308	177,033	1.94
15	14.80	528	0.0109	0.0019	91,308	280,702	3.07

Table 6.9 Determination of EF for "Internal Case" ACE-Asia, 2129_7686.cas. TAS=113.6 ms^{-1}, P=53,000 Pa, ρ= 1,000 kgm^{-3}, core mass flow ratio= 0.22, number of particles injected=999, mass flow rate at entrance=0.0098 kg/s, mass flow rate at exit =0.0021 kg/s (Fluent results).

Particle Size (Micron)	Stokes Number	# of Particles in Core Flow	Mass Flow Rate at Entrance (kg/s)	Mass Flow Rate at Exit (kg/s)	Mixing Ratio of Particles at Entrance	Mixing Ratio of Particles at Exit	Enhancement Factor (EF)
1	0.10	222	0.0098	0.0021	101,783	104,274	1.02
2	0.35	232	0.0098	0.0021	101,783	108,971	1.07
3	0.75	244	0.0098	0.0021	101,783	114,608	1.13
4	1.31	261	0.0098	0.0021	101,783	122,593	1.20
5	2.02	280	0.0098	0.0021	101,783	131,517	1.29
6	2.89	304	0.0098	0.0021	101,783	142,790	1.40
7	3.91	333	0.0098	0.0021	101,783	156,411	1.54
8	5.08	365	0.0098	0.0021	101,783	171,442	1.68
9	6.41	400	0.0098	0.0021	101,783	187,882	1.85
10	7.89	438	0.0098	0.0021	101,783	205,730	2.02
15	17.59	704	0.0098	0.0021	101,783	330,672	3.25

Table 6.10 Determination of EF for "Internal Case" ACE-Asia, 2435_6659.cas. TAS=113.6 ms^{-1}, P=53,000 Pa, ρ= 1,000 kgm^{-3}, core mass flow ratio= 0.27, number of particles injected=999, mass flow rate at entrance=0.0091 kg/s, mass flow rate at exit =0.0024 kg/s (Fluent results).

Particle Size (Micron)	Stokes Number	# of Particles in Core Flow	Mass Flow Rate at Entrance (kg/s)	Mass Flow Rate at Exit (kg/s)	Mixing Ratio of Particles at Entrance	Mixing Ratio of Particles at Exit	Enhancement Factor (EF)
1	0.11	272	0.0091	0.0024	109,853	111,704	1.02
2	0.38	281	0.0091	0.0024	109,853	115,400	1.05
3	0.81	298	0.0091	0.0024	109,853	122,382	1.11
4	1.41	320	0.0091	0.0024	109,853	131,417	1.20
5	2.17	345	0.0091	0.0024	109,853	141,684	1.29
6	3.10	376	0.0091	0.0024	109,853	154,415	1.41
7	4.19	410	0.0091	0.0024	109,853	168,378	1.53
8	5.45	449	0.0091	0.0024	109,853	184,394	1.68
9	6.87	491	0.0091	0.0024	109,853	201,643	1.84
10	8.46	538	0.0091	0.0024	109,853	220,945	2.01
15	18.84	860	0.0091	0.0024	109,853	353,183	3.22

Table 6.11 Determination of EF for "Internal Case" ACE-Asia, 4239_8816.cas. TAS=113.6 ms^{-1}, P=53,000 Pa, ρ= 1,000 kgm^{-3}, core mass flow ratio= 0.32, number of particles injected=999, mass flow rate at entrance=0.0131 kg/s, mass flow rate at exit =0.0042 kg/s (Fluent results).

Particle Size (Micron)	Stokes Number	# of Particles in Core Flow	Mass Flow Rate at Entrance (kg/s)	Mass Flow Rate at Exit (kg/s)	Mixing Ratio of Particles at Entrance	Mixing Ratio of Particles at Exit	Enhancement Factor (EF)
1	0.07	332	0.0131	0.0042	76,522	78,320	1.02
2	0.27	342	0.0131	0.0042	76,522	80,679	1.05
3	0.59	358	0.0131	0.0042	76,522	84,454	1.10
4	1.04	376	0.0131	0.0042	76,522	88,700	1.16
5	1.61	398	0.0131	0.0042	76,522	93,890	1.23
6	2.30	423	0.0131	0.0042	76,522	99,788	1.30
7	3.12	452	0.0131	0.0042	76,522	106,629	1.39
8	4.06	484	0.0131	0.0042	76,522	114,178	1.49
9	5.13	516	0.0131	0.0042	76,522	121,727	1.59
10	6.32	552	0.0131	0.0042	76,522	130,219	1.70
15	14.15	784	0.0131	0.0042	76,522	184,949	2.42

Figure 6.4 shows the enhancement factor as a function of Stokes number for unit density super-micron particles in 1-15 μm diameter range for internal cases with core mass flow ratios in the range of 0.04-0.32.

The core mass flow ratio of 0.04 and 0.32 corresponds to the suction flow rates of 96% and 68% respectively. As it is obvious from the graph, the enhancement factor decreases as the core mass flow ratio increases for the same stokes number.

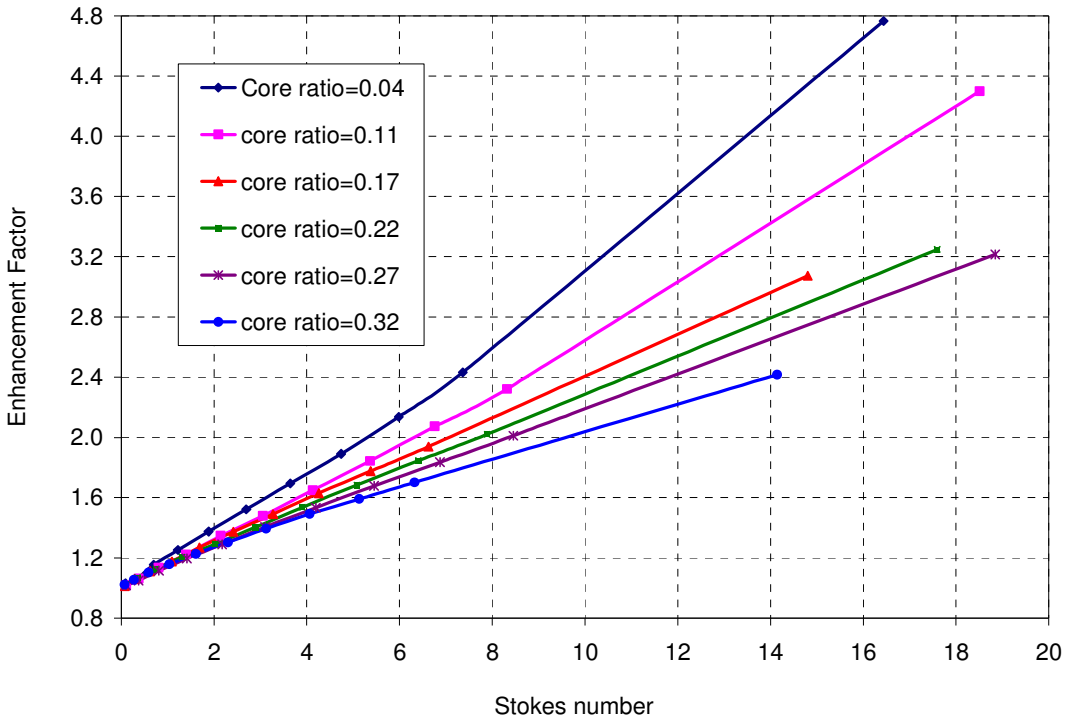

Figure 6.4 Enhancement factor as a function of Stokes number for ACE-Asia, internal cases, TAS=113.6 ms^{-1}, P=53,000 Pa, ρ= 1,000 kgm^{-3}, core mass flow ratio range 0.04-0.32.

6.4 Effect of Particle Density on Particle Enhancement in ACE-Asia LTI

In order to evaluate the effect of particle density on the enhancement of particles, the internal flow calculations discussed in section 6.3 have been repeated with particles of ρ=1,550 kgm^{-3}. The flow conditions, inlet geometry and core mass flow ratios are kept the same, so the only variable that has changed is the density of the injected particles, which is about 50% higher compared to the unit density particles that were tested before. Figure 6.5 shows the enhancement factor as a function of Stokes number for super-micron particles with density of 1,550 kgm^{-3} in 1-15 μm diameter range for internal cases with core mass flow ratios in the range of 0.04-0.32.

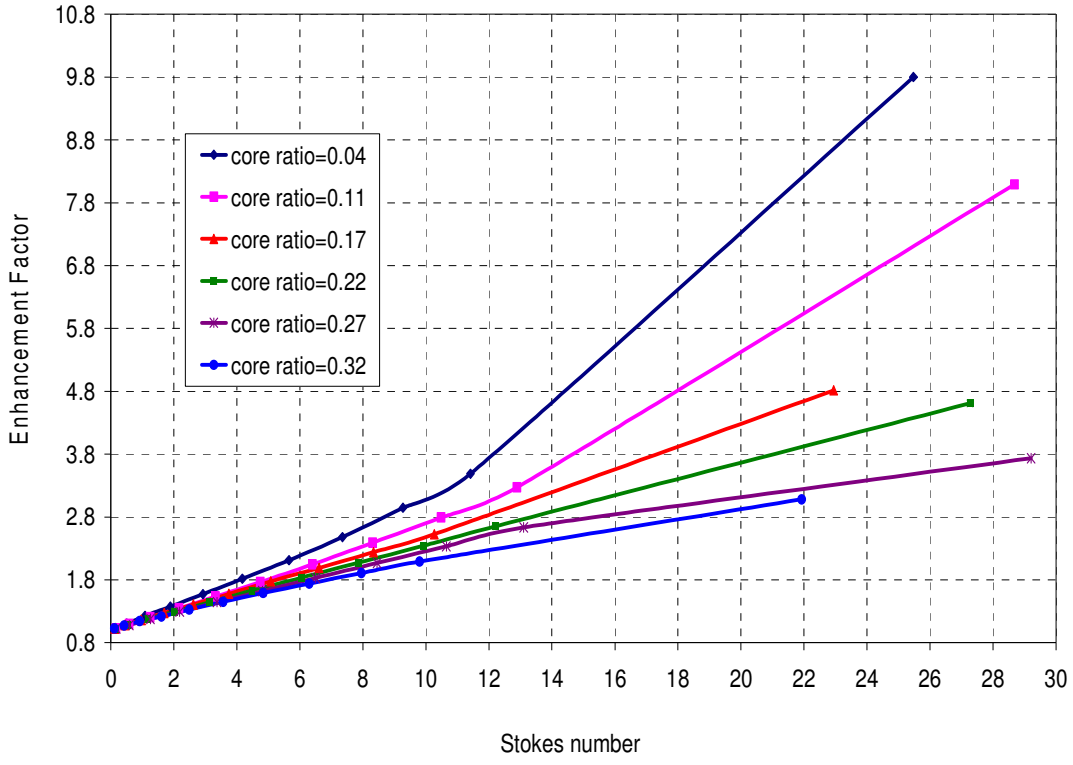

Figure 6.5 Enhancement factor as a function of Stokes number for ACE-Asia, internal cases, TAS=113.6 ms^{-1}, P=53,000 Pa, ρ= 1,550 kgm^{-3}, core mass flow ratio range 0.04-0.32.

The effect of particle density on enhancement factor of super-micron particles is illustrated in Figure 6.5. The slope of the enhancement factor curves in Figures 6.3 and 6.4 is calculated for all of the twelve internal cases, six cases with unit density particles and the other six cases with particle density =1,550 kgm^{-3}. Table 6.12 summarizes the results of slope calculations for the internal cases.

Table 6.12 Slope of the enhancement factor curves for six internal cases and two particle densities (ρ=1,550 kgm^{-3} and ρ=1,000 kgm^{-3}).

Internal Cases	Core Mass Flow Ratio	Slope (m) ρ=1,550 kgm^{-3}	Slope (m) ρ=1,000 kgm^{-3}
400_9415.cas	0.040	0.214	0.19
864_6786.cas	0.110	0.174	0.158
1881_9060.cas	0.170	0.147	0.141
2129_7686.cas	0.220	0.134	0.127
2435_6659.cas	0.270	0.124	0.119
4239_8816.cas	0.320	0.109	0.108

Figure 6.5 shows the slope of the enhancement factor curve as a function of core mass flow ratio for two different particle densities (ρ=1,550 kgm^{-3} and ρ=1,000 kgm^{-3}). The close agreement between the slopes of the enhancement factor curves suggests that the particle density does not play an important role in determination of enhancement factor core mass flow ratios in the range of 0.18-0.26, which is the actual mass flow rate for the field experiments with C-130 aircraft.

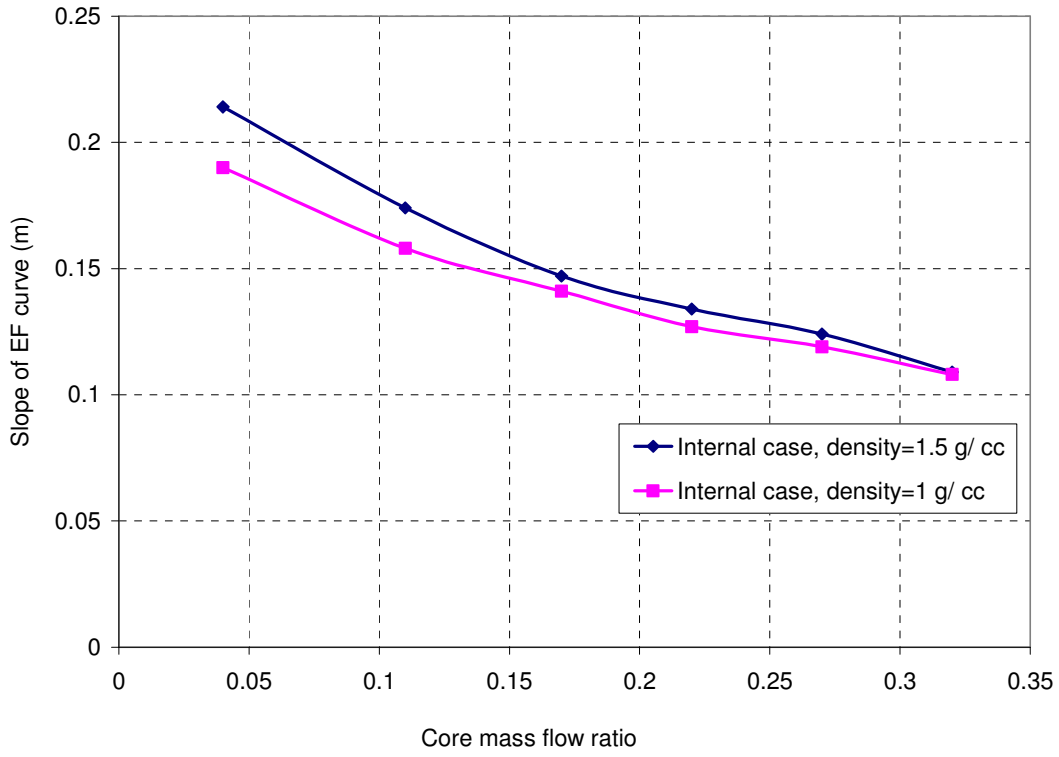

Figure 6.6 Slope of enhancement factor curve as a function of core mass flow ratio for particles of different densities (ρ=1,550 kgm^{-3} and ρ=1,000 kgm^{-3}).

In general, the variation of core mass flow rate changes the slope of the enhancement factor curve. As the core mass flow ratio increases, the slope of the curve decreases. This result can also be concluded from Figures 6.2 through 6.5.

In other words, the lower the suction pressure at the exit of the inlet, the more air is removed from the flow through the porous medium and the less air passes through the core. This corresponds to the lower core mass flow ratio, which means less air passes through the core exit. Lower the mass flow rate at the core exit, higher the enhancement factor of the same size particles. The core mass flow ratio is referred to the ratio of mass flow rate at core exit to the total mass flow rate, i.e. suction flow and core flow together.

6.4 Comparison between the Total and Internal Flow Calculations in Fluent and its Effect on Enhancement Factor of Particles

The calculation of enhancement factor in total flow was described in detail in section 6.2. The slope of the enhancement factor curves resulting from the total flow calculations for unit density particles is given in Table 6.13.

Table 6.13 Slope of the enhancement factor curves for five total cases with particle density (ρ=1,000 kgm^{-3}).

Total Cases	Core Mass Flow Ratio	Slope (m) ρ=1,000 kgm^{-3}
LTI_V2_5_coreratio_0.1cas	0.099	0.1482
LTI_V2_5_coreratio_0.13cas	0.131	0.1394
LTI_V2_5.cas	0.167	0.147
Total_1691_7624	0.182	0.1103
LTI_V2_3.cas	0.297	0.0963

The comparison between the slope of the enhancement curve as a function of core mass flow rate for unit density particles in total and internal flow models in Fluent is shown in Figure 6.7. The close agreement in the results of enhancement factor calculation in total and internal flow justifies the use of internal flow simulations for future applications to minimize the computational resources.

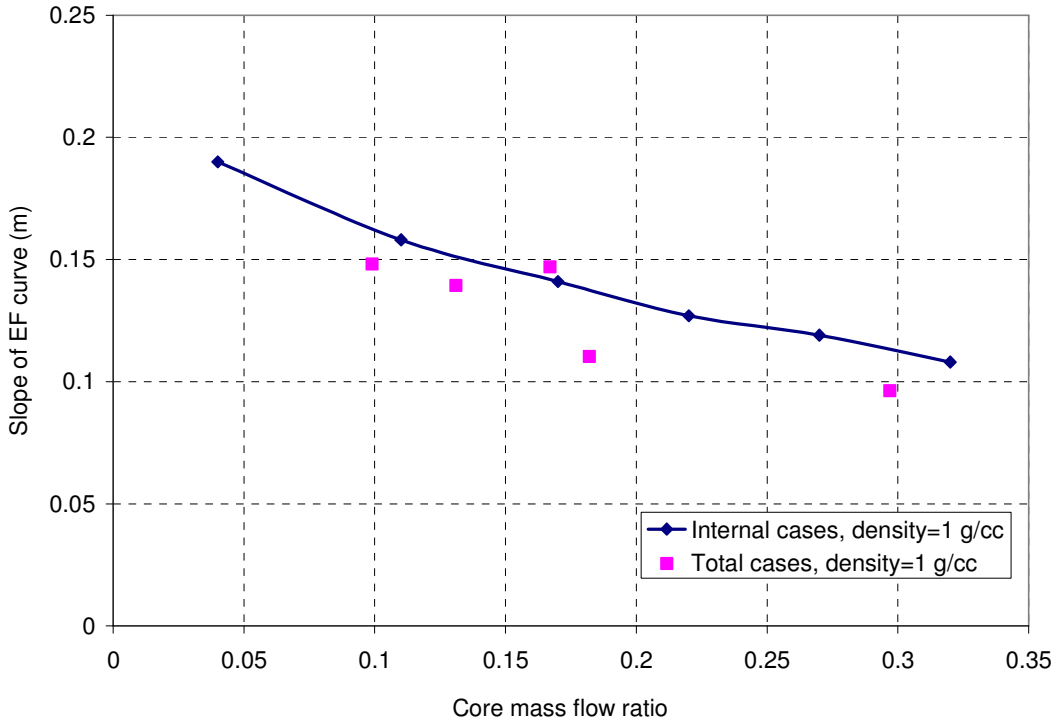

Figure 6.7 Slope of enhancement factor curve as a function of core mass flow ratio for unit density particles, comparison between internal and total flows.

In summary, the study of enhancement factor of the particles resulted in the following conclusions:

- Super-micron particles are enhanced in the diffuser of the low turbulence inlet used in ACE-Asia. The enhancement factor of the particles is a function of particle size. Larger particles enhance several times more than the smaller particles.
- Particle density does not play a role in determination of enhancement factor for particles in the size range of 1-15 μm.

- The effect of core mass flow ratio in determination of enhancement factor is significant. The enhancement factor decreases as the core mass flow rate increases.
- The calculation of enhancement factor based on the core mass flow ratios in the range of 0.04 -0.32 covers the core mass flow ratio for cruise conditions in C-130 aircraft, which is in the range of 0.18-0.26.
- The core mass flow ratio is provided to the users of the instrument, and that is all they need to calculate the ambient mixing ratio of aerosol particles knowing the enhancement factor.
- There is not a significant difference in the enhancement factor calculations using the total cases and internal cases, which justifies the use of internal flow calculations to save time and computational resources.

Chapter 7. Particle Losses in Transport through a Bend

7.1 Introduction

. This chapter investigates the particle deposition to the walls of bends during transport. The particle loss during transport through bends and curves of sampling instruments is a major concern in delivering a representative sample of ambient aerosol to the measuring instruments. The representative sampling refers to the conditions in which the aerosol characteristics such as particle mass and number concentration and size distribution remain unchanged between the point at which the aerosol is sampled and the instrument performing the measurement. It is, however, difficult to prevent changes from occurring during aerosol sampling and transport. Particles, because of their inertia, do not always enter the sampling inlet representatively. They can be lost from the sample flow by contact with the walls of the sampling system. Any changes should be assessed quantitatively so that measurements may be corrected (Brockmann, 2001).

Particle deposition efficiency in bends is calculated using a 3-D model in Fluent. Deposition efficiency is defined as the ratio of the number of particles that are lost in the bend to the total number of particles that have entered the bend. The effect of gravity on particle deposition to the bends is also quantified. The deposition efficiency of particles in ACE-Asia inlet is determined without the consideration of gravity, while the deposition efficiency of particles in NOAA inlet is determined under the condition of applied gravity. ACE-Asia inlet is used in the field program known as: Aerosol Characterization Experiments in Asian Pacific Region. NOAA is the National Oceanic

and Atmospheric Administration. Particles in the size range of 1-20 μm are injected to the flow and the particle trajectories are calculated. The parameters that affect the particle deposition efficiency in bends are flow Reynolds number, particle Stokes number, curvature ratio of the bend, Dean number, and the inlet velocity profile. Dean number is the ratio of Re to the square root of curvature ratio. At a fixed Re and inlet diameter, as the radius of curvature increases, the curvature ratio increases and as a result the Dean number decreases. Smaller Dean number corresponds to less particle deposition for the same Stokes number.

The effect of particle density on deposition efficiency has been analyzed by calculating the deposition efficiency of particles with different densities (ρ=890 kgm^{-3} and ρ=1550 kgm^{-3}). The densities of a few selected aerosols are given in table 7.1 (Seinfeld, 1986):

Table 7.1 Bulk densities for selected aerosol chemical species.

Chemical Species	Density, kgm^{-3}
Water	1,000
Ammonium	1,760
Soot	2,000
Silica	2,660
Model Aerosol	1,700

The effects of flow Reynolds number and radius of curvature of the bend on deposition efficiency of the particles have also been addressed in this Chapter.

7.2 Deposition of Particles in Bend of ACE-Asia Inlet without Gravity

ACE-Asia inlet samples the super-micron particles and transports them to the measuring instruments inside the aircraft. It is basically a conical diffuser with entrance diameter of 1.116 cm, followed by a bend. The deposition efficiency of the particles in ACE-Asia bend is calculated in this section. Gravity is not applied in these calculations.

The bend in the ACE-Asia inlet has a 65.38° curve with a radius of curvature of 0.608 m and an inner diameter of 0.0256 m giving a curvature ratio of 47.5. It has a 0.0774 m straight portion prior to the bend. The extension after the bend is 0.267 m. The velocity inlet profile is not fully developed since there is not enough entrance length provided for a fully developed velocity profile (refer to section 2.6.2). For laminar flows, the ratio of entrance length to tube diameter should be approximately equal to 6% of the flow Reynolds number to ensure the fully developed flow in the tube, in this case about 420 D or 10.76 m.

Air leaves the diffuser at a speed of 4 m/s. The tube cross-sectional area is 5.147 E-04 m^2, giving a flow rate of 2.0589 E-03 m^3/s or about 124 liter per minute (lpm).

7.2.1 Effect of Particle Density on Deposition Efficiency of Particles in ACE-Asia Inlet: No Gravity Applied

In this section, the deposition efficiency of particles is calculated without the consideration of effect of gravity on particle trajectories. In order to evaluate the effect of particle density on deposition efficiency, the particles of two different densities are injected to the bend entrance and the particle trajectories are calculated. The particle densities are 890 kgm^{-3} and 1,550 kgm^{-3}. In all the calculations of this Chapter, 104 particles that are equally spaced are injected to the flow. The deposition efficiency is

them calculated as the ratio of the number of particles that are deposited into the walls of the inlet (determined from particle trajectories) to the total number of particles that have entered the inlet (in this study, 104 particles).

The results of Fluent calculations of deposition efficiency of particles with two different in a 65 ° bend are summarized in Table 7.2.

Figure 7.1 shows the comparison between the deposition efficiency of particles with different densities for ACE-Asia inlet, with flow Reynolds number, Re=7010.

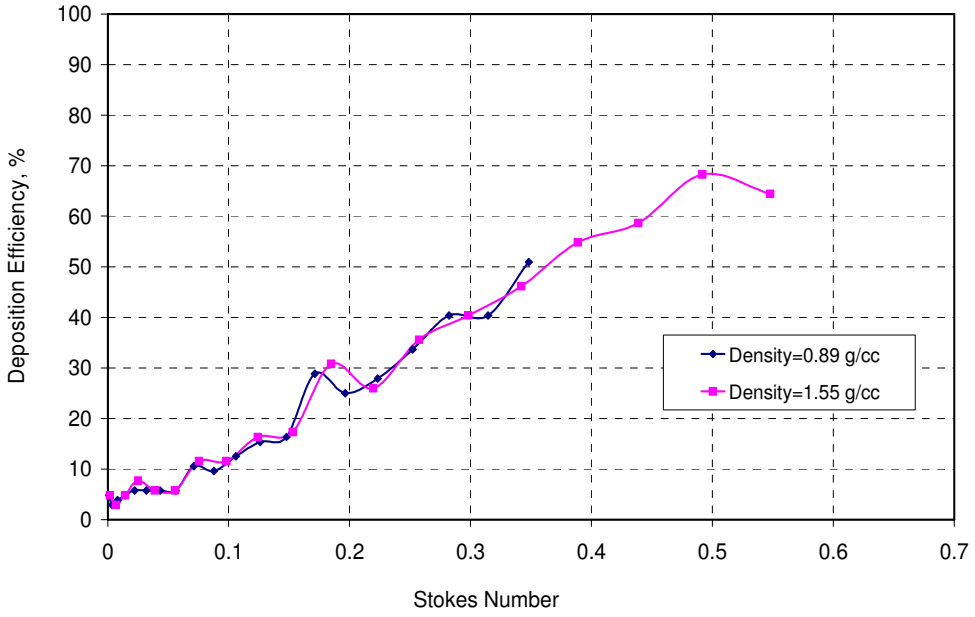

Figure 7.1 Deposition efficiency as a function of Stokes number in ACE-Asia inlet for particles of different densities (ρ=890 kgm^{-3} and ρ=1550 kgm^{-3}), No gravity applied, 65° bend and Re=7010.

Table 7.2 Determination of deposition efficiency of particles in ACE-Asia inlet for particles of different densities (ρ=890 kgm^{-3} and ρ=1550 kgm^{-3}), No gravity applied, 65° bend and Re=7010.

Particle Size (μm)	Stokes Number (ρ=0.89g/cc)	# of Particles Deposited to Inlet Walls (ρ=0.89g/cc)	Deposition Efficiency (%) (ρ=0.89g/cc)	Stokes Number (ρ=1.55g/cc)	# of Particles Deposited to Inlet Walls (ρ=1.55 g/cc)	Deposition Efficiency (%) (ρ=1.55 g/cc)
1	0.001	5	4.81	0.002	5	4.81
2	0.004	3	2.88	0.007	3	2.88
3	0.008	4	3.85	0.014	5	4.81
4	0.014	5	4.81	0.025	8	7.69
5	0.022	6	5.77	0.039	6	5.77
6	0.032	6	5.77	0.056	6	5.77
7	0.043	6	5.77	0.075	12	11.54
8	0.056	6	5.77	0.098	12	11.54
9	0.071	11	10.58	0.124	17	16.35
10	0.088	10	9.62	0.153	18	17.31
11	0.106	13	12.50	0.185	32	30.77
12	0.126	16	15.38	0.220	27	25.96
13	0.148	17	16.35	0.257	37	35.58
14	0.171	30	28.85	0.298	42	40.38
15	0.196	26	25.00	0.342	48	46.15
16	0.223	29	27.88	0.389	57	54.81
17	0.252	35	33.65	0.439	61	58.65
18	0.282	42	40.38	0.492	71	68.27
19	0.315	42	40.38	0.548	67	64.42
20	0.348	53	50.96	0.606	75	72.12

The effect of particle density on deposition of particles has also been investigated for 90° bends. The particles with the same densities mentioned above are injected to 90° bends with lower Reynolds number and the deposition efficiencies are calculated.

The results of Fluent calculations of deposition efficiency of particles with two different in a 90 ° bend are summarized in Table 7.3.

Figure 7.2 shows the deposition efficiency of particles as a function of Stokes number for particles with different densities (ρ=890 kgm^{-3} and ρ=1550 kgm^{-3}), in a 90° bend with flow Reynolds number, Re=1000.

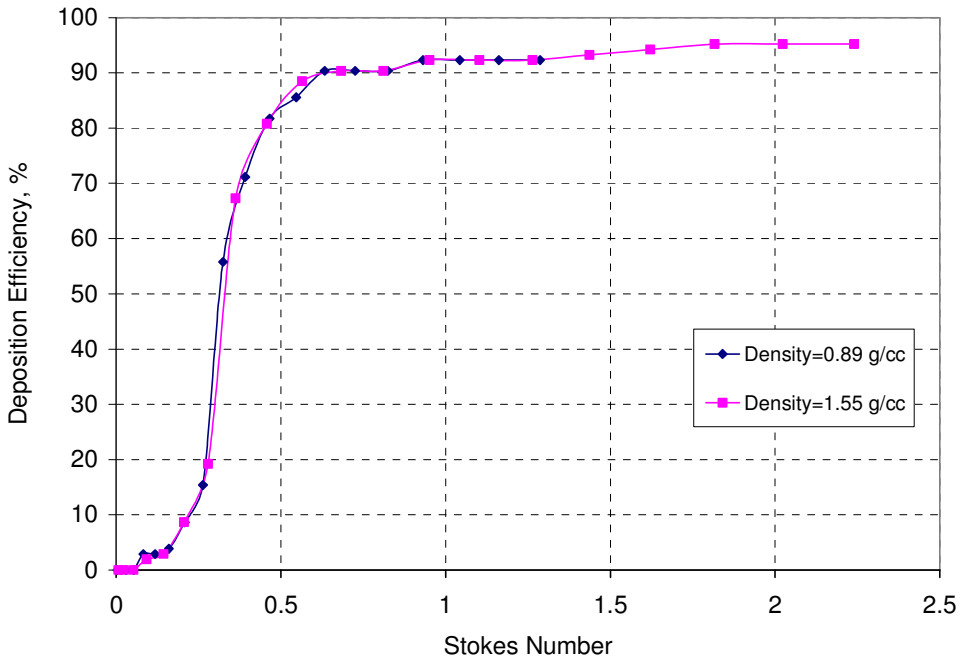

Figure 7.2 Deposition efficiency as a function of Stokes number in ACE-Asia inlet for particles of different densities (ρ=890 kgm^{-3} and ρ=1550 kgm^{-3}), No gravity applied, 90° bend and Re=1000.

Table 7.3 Determination of deposition efficiency of particles in ACE-Asia inlet for particles of different densities (ρ=890 kgm^{-3} and ρ=1550 kgm^{-3}), No gravity applied, 90° bend and Re=1000.

Particle Size (μm)	Stokes Number (ρ=0.89g/cc)	# of Particles Deposited to Inlet Walls (ρ=0.89g/cc)	Deposition Efficiency (%) (ρ=0.89g/cc)	Stokes Number (ρ=1.55g/cc)	# of Particles Deposited to Inlet Walls (ρ=1.55 g/cc)	Deposition Efficiency (%) (ρ=1.55 g/cc)
1	0.004	0	0	0.006	0	0
2	0.014	0	0	0.024	0	0
3	0.030	0	0	0.053	0	0
4	0.053	0	0	0.093	2	1.92
5	0.082	3	2.88	0.143	3	2.88
6	0.118	3	2.88	0.205	9	8.65
7	0.160	4	3.85	0.279	20	19.23
8	0.208	9	8.65	0.363	70	67.31
9	0.263	16	15.38	0.458	84	80.77
10	0.324	58	55.77	0.565	92	88.46
11	0.392	74	71.15	0.682	94	90.38
12	0.466	85	81.73	0.811	94	90.38
13	0.546	89	85.58	0.951	96	92.31
14	0.633	94	90.38	1.102	96	92.31
15	0.726	94	90.38	1.264	96	92.31
16	0.825	94	90.38	1.437	97	93.27
17	0.931	96	92.31	1.622	98	94.23
18	1.043	96	92.31	1.817	99	95.19
19	1.162	96	92.31	2.024	99	95.19
20	1.286	96	92.31	2.240	99	95.19

As it is clear from Figures 7.1 and 7.2, the density of particles plays no significant role in deposition efficiency of particles in the size range of 1-20 μm. This result is expected, since the deposition efficiency is plotted against Stokes number, which has the density term in it. Therefore, the deposition efficiency is actually plotted against the aerodynamic diameter of the particles.

7.2.2 Effect of Total Angle of Bend on Particle Deposition Efficiency

In order to determine the effect of angle of bend on particle deposition efficiency, a new geometry was created with all the ACE-Asia inlet features except for the bend which had a 90° curve instead of a 65° curve. The Ace-Asia inlet was modeled in Fluent with a 90° bend keeping the geometry and all other flow parameters the same. The 90° bend has a smaller radius of curvature than a 65° bend, which in turn results in a smaller curvature ratio assuming the same tube diameter. The smaller the curvature ratio, the larger the Dean number. As mentioned earlier, an increase in Dean number results in higher deposition efficiency. As expected, the deposition efficiency of 65° bend was lower than that of a 90° bend. However, the pattern of the deposition efficiency curve remains the same, suggesting the pattern deposition in turbulence flows, Figure 7.3.

The polynomial fit to the results of Fluent calculations for Ace-Asia inlet with Re=7010 and bend angle=65° is shown if Figure 7.4.

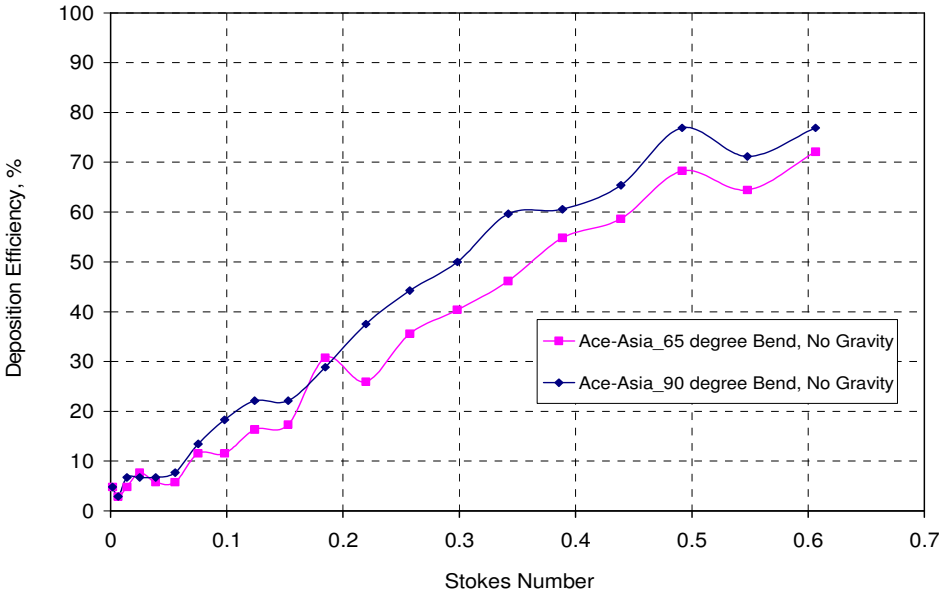

Figure 7.3 Deposition efficiency as a function of Stokes number in ACE-Asia inlet for particles with density (ρ=1550 kgm^{-3}), No gravity applied, comparison between deposition efficiencies in 65° and 90° bend, Re=7010.

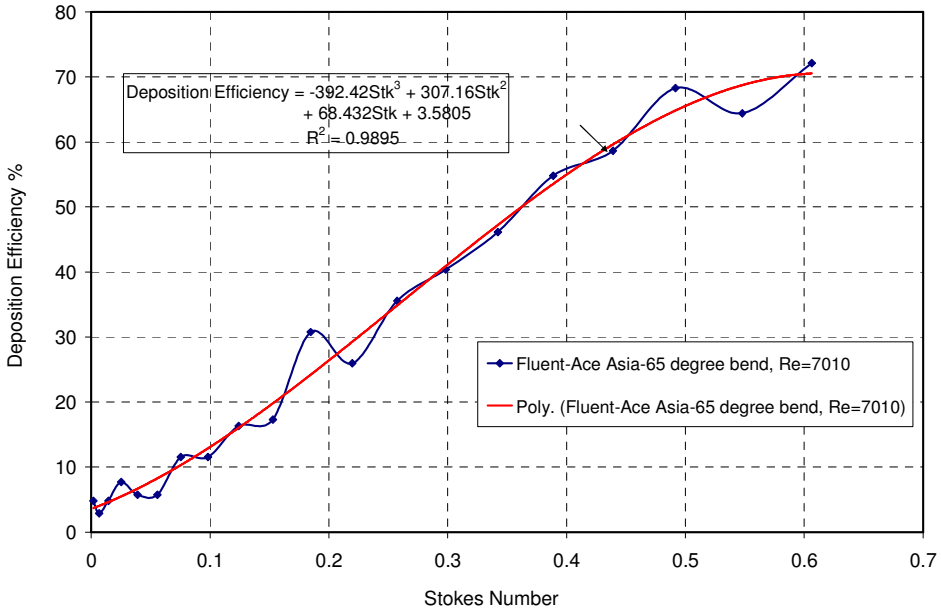

Figure 7.4 The polynomial fit to the deposition curve for Ace-Asia inlet, Re=7010, (ρ=1550 kgm^{-3}), No gravity applied, 65° bend.

7.2.3 Effect of Flow Reynolds Number on Deposition Efficiency of Particles

The effect of Reynolds number on particle deposition in Ace-Asia inlet is shown in figure 7.5 by comparing Fluent calculations for Re=7010, Re=6000 and Re=3000.

Assuming a flow Reynolds number of 6000 in the inlet, the velocity of flow becomes 3.42 m/s. A reduction in Re, reduces the Dean number and increases the penetration of particles through the bend. The reduction of Re to 3000 requires a reduction in velocity of air to 1.71 ms^{-1}.

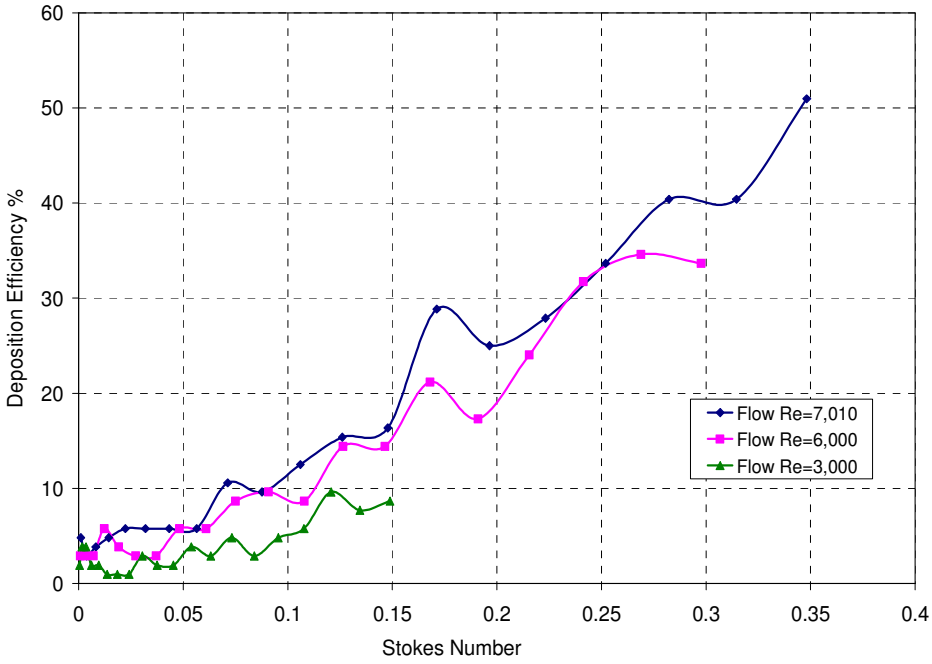

Figure 7.5 Effect of flow Reynolds number on deposition efficiency of particles as a function of Stokes number in Ace-Asia inlet, No gravity applied, ρ=890 kgm^{-3}, 65° bend.

As seen in Figure 7.5, the deposition efficiency of particles is not greatly affected by changes in the flow Reynolds number as high as 100% or more.

7.3 Deposition of Particles in Bend of NOAA Inlet with Application of Gravity

In this section, the application of gravity and its effect on particle deposition efficiency is investigated. The particles in the size range of 1-20 μm are injected to the flow. The flow in the bend is solved with applied gravity. The results of particle trajectories with gravity are then compared to the particle deposition in the bend without the consideration of force of gravity.

7.3.1 LTI Bend Geometry used in NOAA

A 65° bend is modeled in Gambit software in 3-D. The bend is approximately 0.71 m long and the diameter of the tube is 0.0256m. Two straight sections are added to the bend, 0.077 m extension prior to the bend, and a 0.267 m extension after the bend. The bend and the straight sections are about 1.06 m long. The radius of curvature of the bend is 0.608 m, with a curvature ratio of 47.5. The curvature ratio is referred to the ratio of radius of curvature to the tube radius.

Equations 7.1 through 7.3 define the Dean number, Reynolds number and curvature ratio respectively.

$$Dean\ \ Number = \frac{Flow\,\mathrm{Re}}{\sqrt{Curvature\ Ratio}} = \frac{\mathrm{Re}}{\sqrt{R_0}} \tag{7.1}$$

$$Flow\,\mathrm{Re}\,ynolds\,Number = \frac{\rho_g V_g D_{flow\ geometry}}{\mu} \tag{7.2}$$

$$Curvature\ \ Ratio = \frac{Radius\ of\ \ Curvature\ of\ \ Bend}{Tube\ Radius},\ R_0 = \frac{R_b}{a_{tube}} \tag{7.3}$$

The bend is modeled in Fluent as a whole tube, not half of the tube, to be able to include the effect of gravity in flow calculations and particle trajectories. The particle

trajectories are different for the two halves of the model due to the fact that gravity is applied in flow calculations.

The volume of the bend is meshed with 623,700 volume meshes and 625,294 nodes. The nodes on the edges of the bend are 1.5 mm apart. This is the optimum mesh size, since the finer mesh does not change the flow solution. The aspect ratio of meshes on the entrance surface of the tube varies from 0.1 at the center of the tube to about 5.5 close to the walls. The accurate solution of the flow in center of the tube is essential since the sample air is selected from the center of the tube for further analysis.

The laminar flow of air at a speed of about 4 m/s is entered the bend. The gravity of 9.81 ms^{-2} in –Z direction is applied to the flow. The flow Reynolds number in the bend is 7010, and the Dean number is 1070. Dean number is the ratio of flow Reynolds number to the square root of curvature ratio.

There are different views about the extent of Dean number to which the flow in bend can be considered laminar. The flow in bends differs that in a straight pipe mainly through exhibiting a secondary flow in planes normal to the main flow. Centrifugal forces act at right angles to the main direction of the flow, so that the profile of axial velocity is distorted and the point at which the velocity has its peak is shifted to the outside. The flow is more stable than straight tubes because of the stabilizing effect produced by the curvature.

Theoretically, flow in a bend is considered laminar at least for small and intermediate Dean numbers, De ≤ 370 (Pui et.al, 1987; McFarland et.al, 1997), which corresponds to a Reynolds number of 1170 for a curvature ratio of 10. However, the secondary flow in a bend causes the overall flow to be more stable. The critical Re can be

as large as 7800 for a curvature ratio of 7 (Soh and Berger, 1984). This corresponds to a Dean number as high as 2948. According to Pui et.al, the critical Re for a curvature ratio of 31.9 is 5000, which corresponds to a Dean number of 885.

7.3.2 Effect of Gravity on Particle Deposition Efficiency in NOAA LTI

To evaluate the effect of gravity on particle deposition, 208 evenly distributed particles in the size range of 1-20 μm are injected to the bend. The surface of entrance to the bend is in Y-Z plane, and the injection files created consist of the coordinate of particles in Y and Z direction, keeping X-coordinate of the particles constant.

The flow in the bend is solved in Fluent with and without considering the force of gravity. The evenly distributed unit density particles, in the range of 1-20 microns, are then injected to the flow through the bend entrance surface, which is a circle positioned in Y-Z plane. The particle trajectories and the bend deposition efficiencies are then calculated in each case. The results of all 20 injections are summarized in Tables 7.4 (without gravity) and 7.5 (with gravity).

Table 7.4 Bend deposition efficiency, LTI used in NOAA, ρ=1,000 kgm^{-3}, 65° bend, without gravity.

Dp (μm)	Slip correction (Cc)	Stokes Number	# of Particles injected	# of Particles escaped	# of Particles trapped	Deposition Efficiency
1	1.17	0.001	208	196	10	4.81
2	1.09	0.004	208	196	10	4.81
3	1.06	0.009	208	195	11	5.29
4	1.04	0.016	208	194	8	3.85
5	1.03	0.024	208	193	12	5.77
6	1.03	0.035	208	188	16	7.69
7	1.02	0.047	208	185	18	8.65
8	1.02	0.062	208	185	17	8.17
9	1.02	0.078	208	182	25	12.02
10	1.02	0.096	208	180	26	12.50
11	1.02	0.116	208	182	23	11.06
12	1.01	0.137	208	185	20	9.62
13	1.01	0.161	208	180	28	13.46
14	1.01	0.187	208	181	26	12.50
15	1.01	0.214	208	174	34	16.35
16	1.01	0.243	208	162	44	21.15
17	1.01	0.275	208	163	42	20.19
18	1.01	0.308	208	148	59	28.37
19	1.01	0.343	208	147	61	29.33
20	1.01	0.379	208	151	57	27.40

Table 7.5 Bend deposition efficiency, LTI used in NOAA, ρ=1,000 kgm^{-3}, 65° bend, with gravity.

Dp (μm)	Slip correction (Cc)	Stokes Number	# of Particles injected	# of Particles escaped	# of Particles trapped	Deposition Efficiency
1	1.17	0.001	208	195	7	3.37
2	1.09	0.004	208	198	7	3.37
3	1.06	0.009	208	195	11	5.29
4	1.04	0.016	208	195	12	5.77
5	1.03	0.024	208	193	15	7.21
6	1.03	0.035	208	188	20	9.62
7	1.02	0.047	208	189	19	9.13
8	1.02	0.062	208	186	22	10.58
9	1.02	0.078	208	182	26	12.50
10	1.02	0.096	208	179	29	13.94
11	1.02	0.116	208	174	34	16.35
12	1.01	0.137	208	166	42	20.19
13	1.01	0.161	208	164	44	21.15
14	1.01	0.187	208	157	51	24.52
15	1.01	0.214	208	152	56	26.92
16	1.01	0.243	208	148	60	28.85
17	1.01	0.275	208	135	73	35.10
18	1.01	0.308	208	129	79	37.98
19	1.01	0.343	208	126	82	39.42
20	1.01	0.379	208	121	87	41.83

The Stokes number is determined using the following formula:

$$Stk = \frac{\rho V D_p^{\,2} C_c}{9 \mu d} \tag{7.4}$$

Where, ρ = particle density, 1000 kg/m³

V = velocity of air at bend entrance, 4 m/s

D_p = particle diameter, m

C_c = Slip correction factor

μ = Air viscosity, kg/m.s

d = Bend entrance diameter, 0.0256m

The Slip correction factor is determined from:

$$Cc = Kn(1.257 + (0.4e^{(-1.1/Kn)}) + 1) \tag{7.5}$$

$$K_n = \frac{2\lambda}{D_p} \tag{7.6}$$

$$\lambda = 0.00002333 \frac{T}{P} \tag{7.7}$$

The viscosity of air is calculated using the following formula:

$$\mu = \frac{1.458E-06T^{1.5}}{110.4+T} \tag{7.8}$$

In the determination of Stokes number, the temperature and pressure dependence of slip correction factor and temperature dependence of viscosity of air are considered, but in Fluent calculations the viscosity of air is assumed to be constant all over the domain.

Figure 7.6 shows the bend deposition efficiency of 1-20 micron unit density particles vs. the Stokes number.

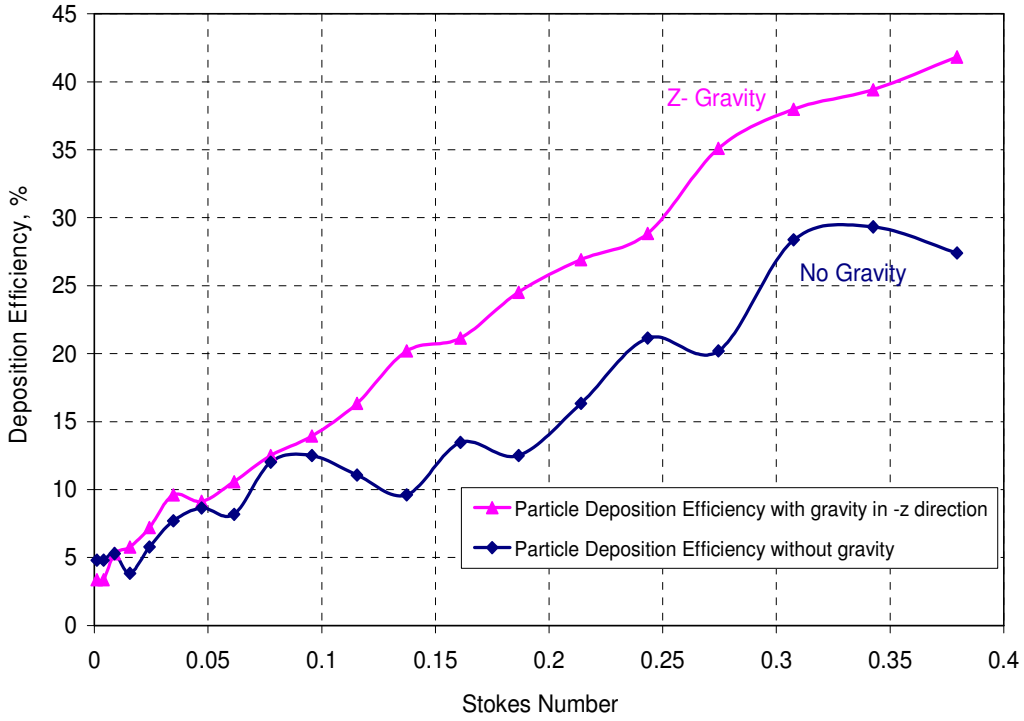

Fig 7.6 Comparison of particle deposition with gravity and without force of gravity.

The particle deposition efficiency is roughly 20 % higher under the application of gravity, for particles bigger than 10 micron.

Gravity plays an important role in particle deposition for particles greater than 10 micron**.**

The particles distribution at exit of calculation domain is determined for particle sizes 1, 5, 10, 15 and 20 µm. The particles are not evenly distributed at exit. Therefore the sampled air may not represent the correct mixing ratio, suggesting the requirement of more mixing.

7.3.2 Distribution of Particles at the Exit of the Bend under Gravity

The particles coordinates at outflow surface have been recorded for particles with diameters 1, 5, 10, 15 and 20 microns. The bigger the particle, the less is the number of particles at exit from the bend. Smaller particles tend to follow the flow, while the bigger ones follow their own patterns due to higher drag forces and inertia.

Figures 7.7 through 7.11 show the distribution of particles at exit from the flow calculation domain.

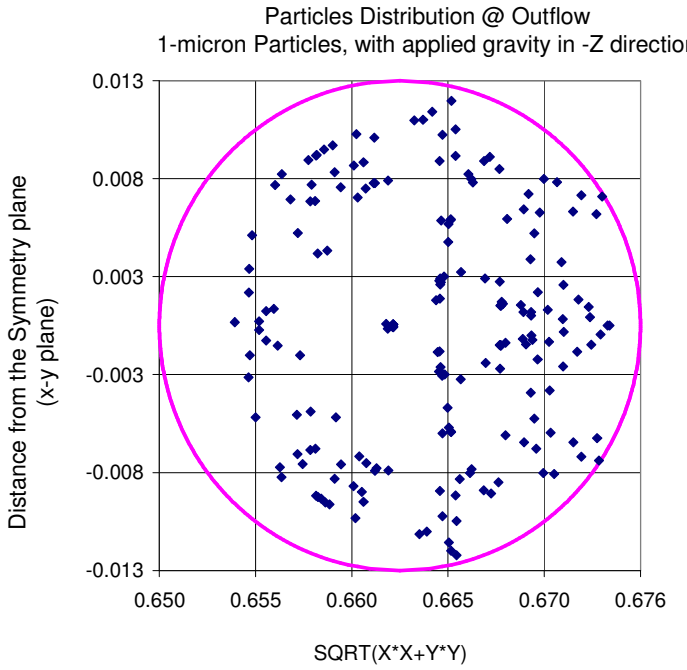

Fig 7.7 Particles distribution @ Outflow, 1-micron, with gravity in -Z direction.

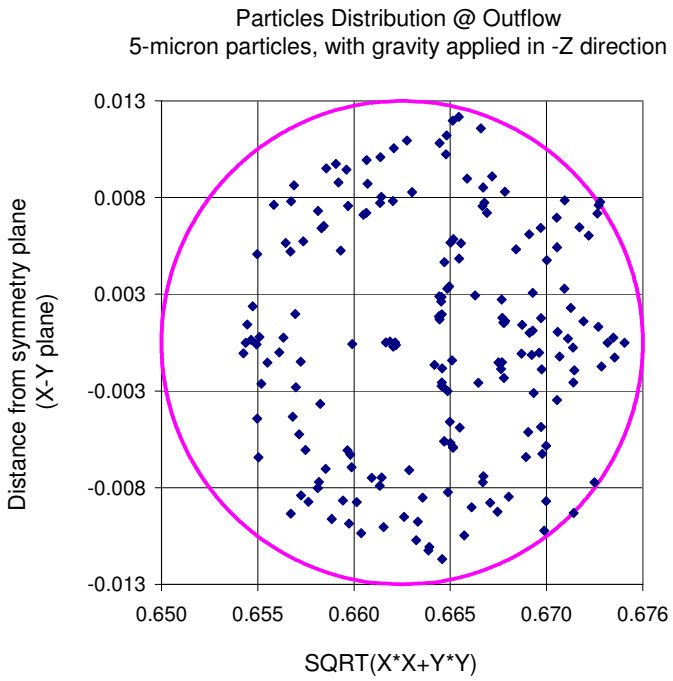

Fig 7.8 Particles distribution @ Outflow, 5-micron, with gravity in -Z direction.

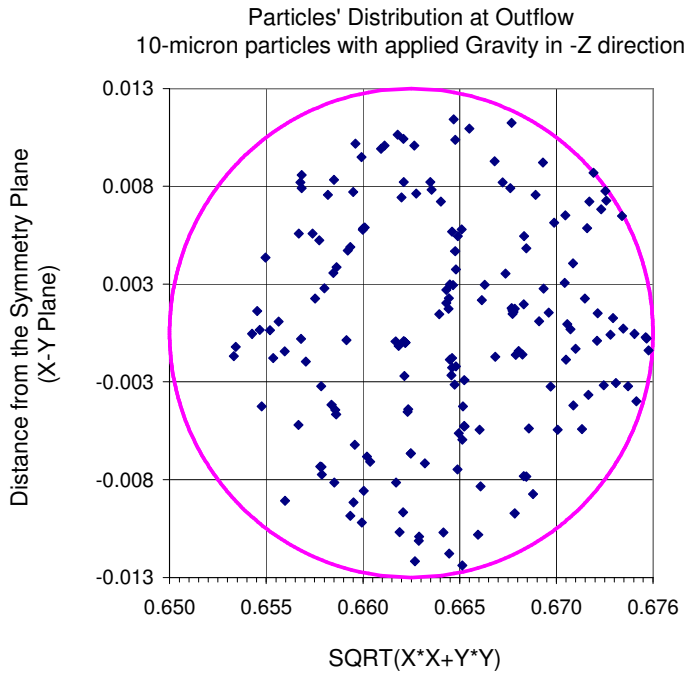

Fig 7.9 Particles distribution @ Outflow, 10-micron, with gravity in -Z direction.

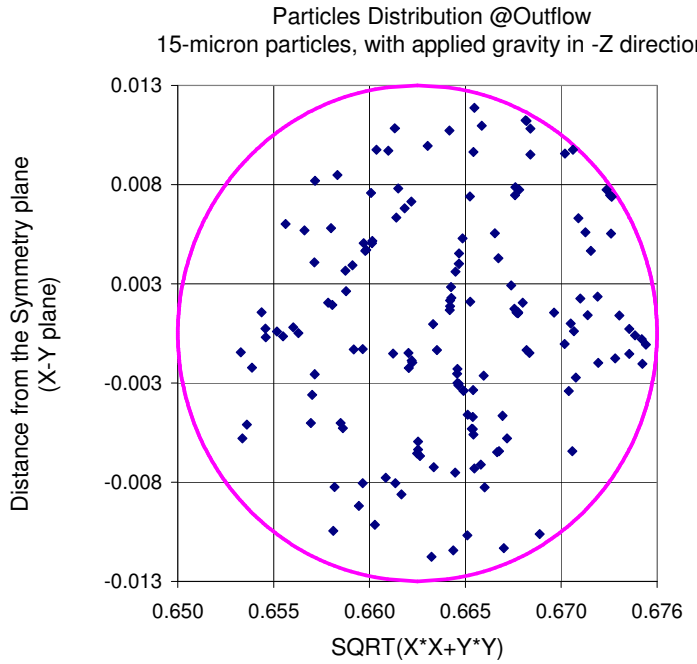

Fig 7.10 Particles distribution @ Outflow, 15-micron, with gravity in -Z direction.

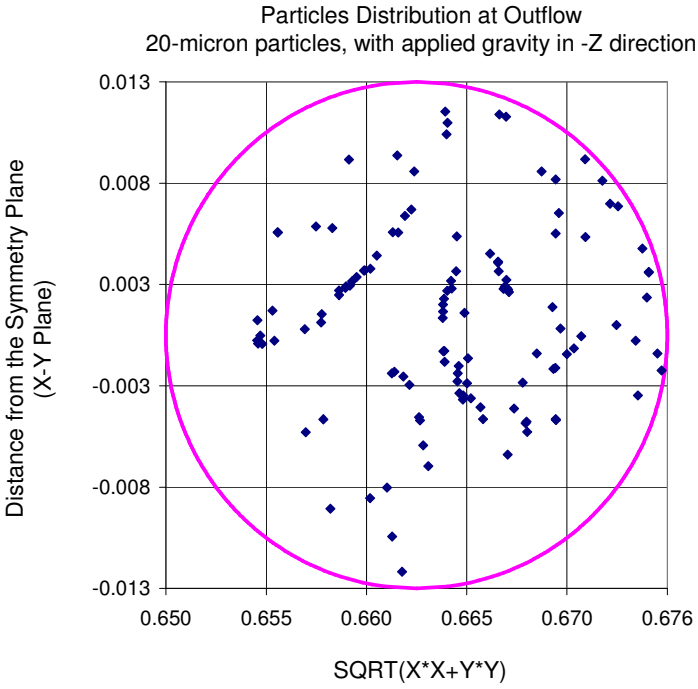

Fig 7.11 Particles distribution @ Outflow, 20-micron, with gravity in -Z direction.

7.3.3 Original Distribution of particles Removed by Deposition

The initial coordinate of injected particles that did not make it to the bend exit is determined by comparing the injection files and the outflow files for particle sizes 1, 5, 10, 15 and 20 microns.

Figures 7.12 through 7.16 show the entrance coordinate of particles that were removed from the flow by deposition to the bend walls.

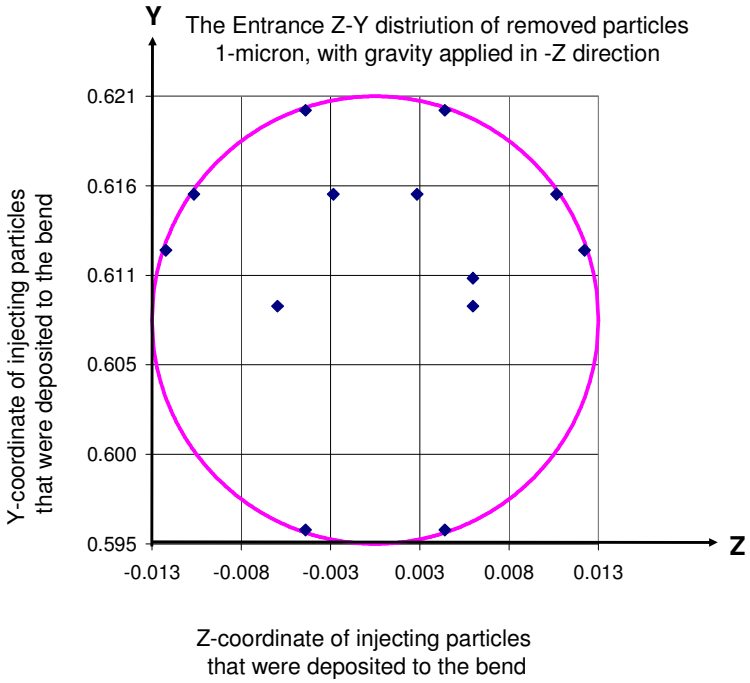

Fig 7.12 The coordinate of particles at entrance for1-micron, unit density injections, removed from the flow.

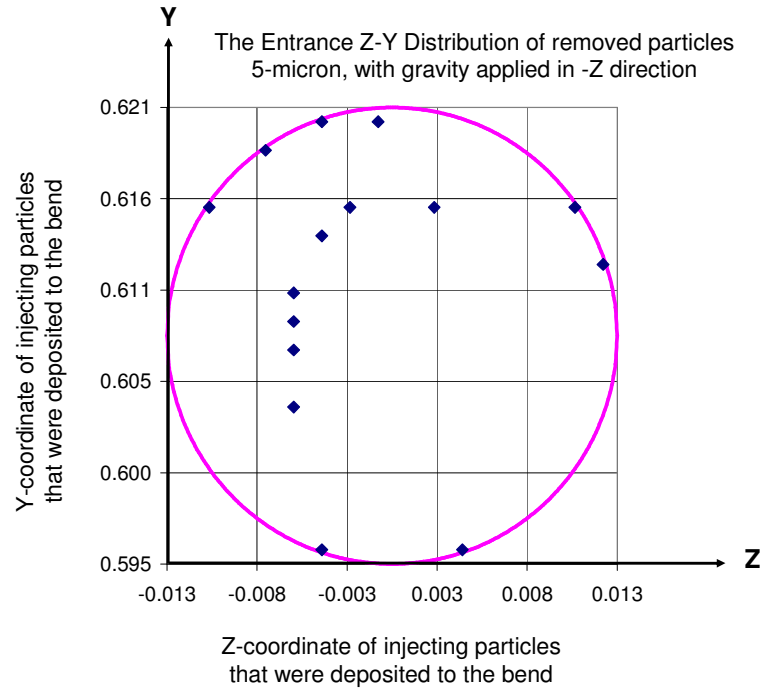

Fig 7.13 The coordinate of particles at entrance for5-micron, unit density injections, removed from the flow.

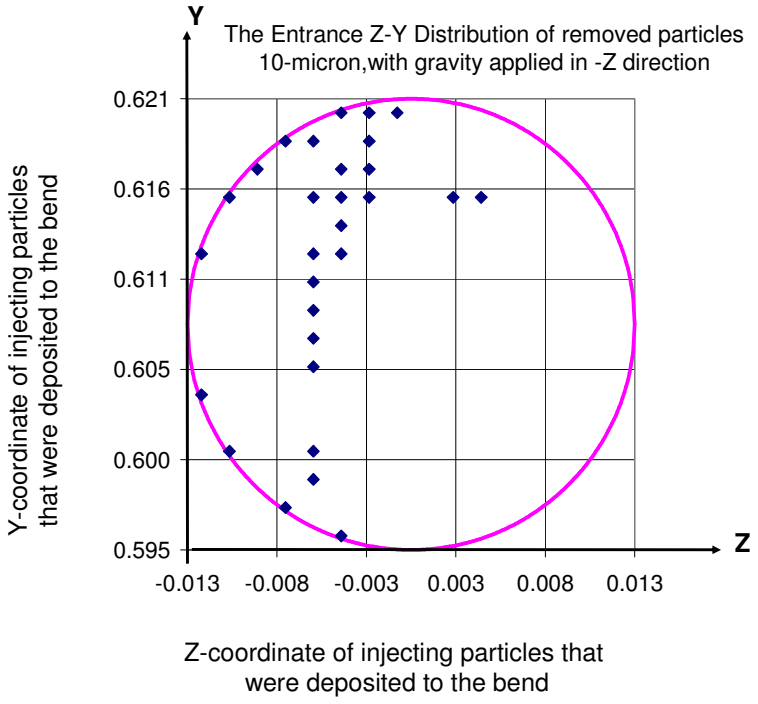

Fig 7.14 The coordinate of particles at entrance for10-micron, unit density injections, removed from the flow.

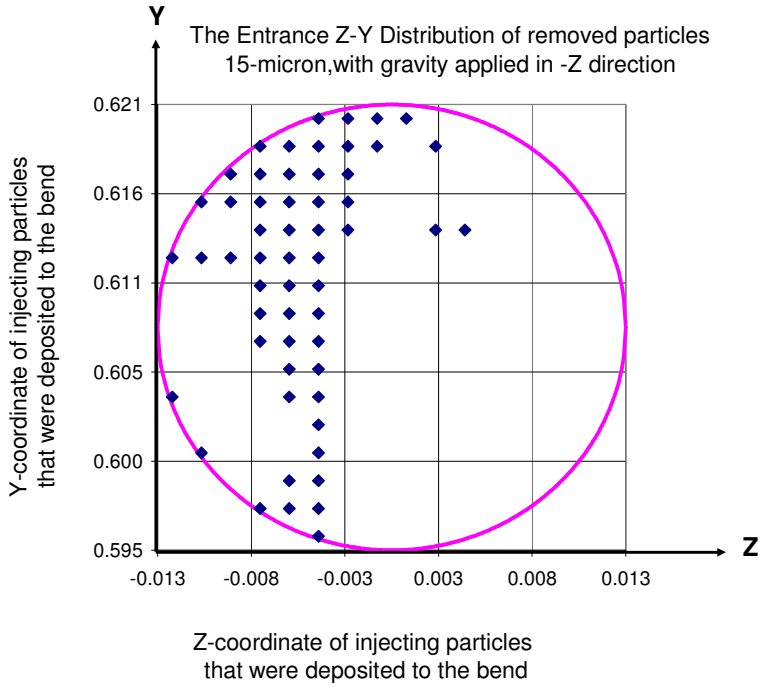

Fig 7.15 The coordinate of particles at entrance for15-micron, unit density injections, removed from the flow.

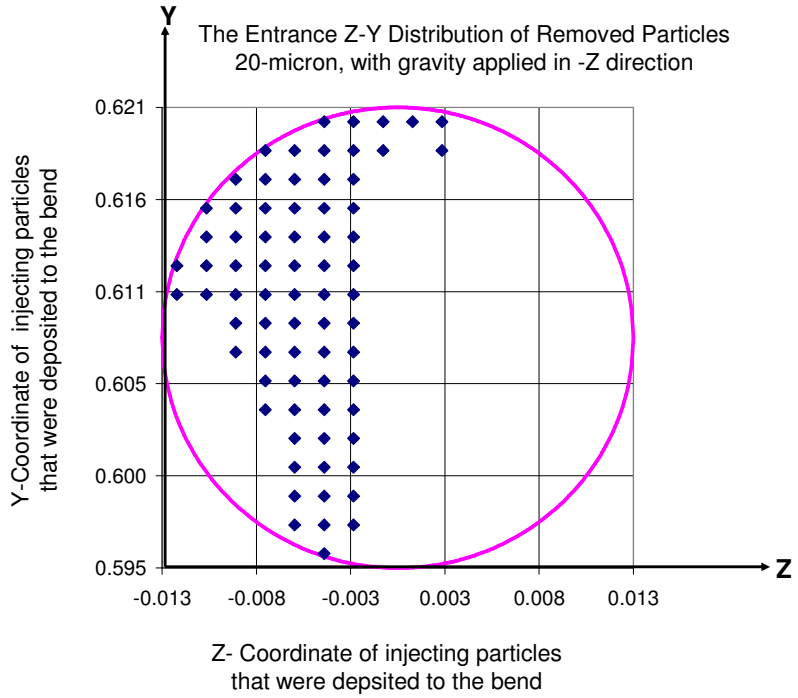

Fig 7.16 The coordinate of particles at entrance for 20-micron, unit density injections, removed from the flow.

As seen in the figures, the removed particles are mainly in the lower half of the bend, in the direction of applied gravity. By introducing the effect of force of gravity to the particles, the deposition efficiency is increased by about 15-20 % for particles bigger than 10 micron. The particles at exit of calculation domain are not distributed evenly in the area; therefore, the chances of getting no particles while pulling from some points in the middle of exit domain are very high. This suggests that more mixing is required.

Chapter 8. Conclusions and Discussions

The objectives of this research work were (i) to design an airborne instrument to measure the aerodynamic diameter and concentration of suspended dust particles in the range from 1 μm to 30 μm from aircraft, (ii) to evaluate the performance of a low turbulence inlet used in ACE-Asia field program in 2000 by quantifying the particle enhancements in the inlet diffuser and particle losses in bend of the inlet, and (iii) to study the effect of gravity on the numerical results of calculating the particle deposition in bend of the low turbulence inlet used in NOAA research in 2004.

The designed instrument consisted of a low turbulence inlet and a laser-Doppler velocimeter. The low turbulence inlet reduced the air speed without generation of additional turbulence. It used the boundary layer suction through a porous diffuser to remove about 80% of the air that was responsible for turbulence generation and particle loss due to turbulent deposition of particles to the diffuser walls. It also made it possible to solve the flow and calculate the particle trajectories in laminar flow using the computational fluid dynamics software. The laser-Doppler velocimeter determined the velocity of the particles as they entered the viewing volume of the velocimeter. The aerodynamic diameter of the particles and their concentration in ambient air were then calculated from the velocity measurements.

The aerodynamic diameter of a particle combines the effects of particle size, shape and density into one parameter. It determines the sedimentation characteristics of the particles in the atmosphere, which is very important in the study of climate models.

The effect of particles hitting the leading edge of the inlet and bouncing off to enter the viewing volume of LDV at a lower velocity was quantified. Particles in the size range of 1-30 μm were injected to the flow and particle trajectories were calculated in Fluent. In each particle size range, there were a few particles that hit the leading edge of the inlet bounced back and ended up in the viewing volume of the velocimeter. These particles were lass than 10% of the total number of particles that were introduced to the flow in each size range. The instrument output of velocity measurement included these bounced particles, which led to the ambiguity in calculation of the actual number of particles that entered the viewing volume at a specific velocity. A response matrix was created to account for the number of particles that hit the leading edge of the inlet, and relocate them to their corresponding size bins.

The response matrix was created for seven cases with different flow conditions, inlet geometry, aircraft velocities and ambient air properties.

The collision of particles with the leading edge of the inlet was assumed to be an elastic collision for all the cases studied. The assumption of elastic collision was justified considering the fact that the uncertainty in the size distribution that may enter the calculation by assuming the elastic collision is much less than the reported discrepancies in the size distribution of particles in the interested size range.

The designed instrument is not suitable for the measurement of ice particles. The effect of ice particle shatter on impact with the leading edge of the instrument is not known.

The performance of the low turbulence inlet used in ACE-Asia field program was evaluated in this work. The enhancement of particles in the porous diffuser and the particle losses in transport through the inlet bend were calculated.

The enhancement factor was defined as the ratio of the number of particles per unit mass of air at the exit of the inlet to the number of particles per unit mass of air at the inlet entrance. The enhancement factor of the particles was calculated in models of different flow conditions. The enhancement factor as a function of the flow rate at the exit of the diffuser was compared for internal and total cases. Internal case refers to a case in which the flow inside the diffuser was modeled in Fluent. In total cases, the flow inside and around the diffuser is modeled in Fluent. The results of the enhancement factor calculations justified the use of internal flow models.

The particle losses in transport through bends of low turbulence inlets used in ACE-Asia and NOAA field programs were calculated. The effect of the force of gravity on the deposition efficiency of particles was studied. Deposition efficiency of particles was defined as the ratio of the number of particles that are lost due to deposition to the walls of the bend to the total number of particles that entered the bend. It was concluded that gravity played an important role in deposition of particles to the walls of the bend for particles larger than 10 μm.

There is a strong need to better understand the net impact of aerosol particles on Earth's climate. The new technique developed in this work can be utilized towards the development of new instruments to measure the particles in other size ranges.

Further analysis of particle motion in different flow conditions, other than those discussed in this work, will expand the benefits of using this technique towards the particle measurement in other regions of the atmosphere.

This new idea needs to be tested in the field experiments before it can claim to be a reliable instrument. The experimental analysis of the prototype model of the instrument is an essential part of the future work.

Bibliography

Brock, C. A., Sullivan, A. P., Peltier, R. E., Weber, R. J., Wollny, A., de Gouw, J. A., Middlebrook, A., Atlas, E., Stohl, A., Trainer, M. K., Cooper, O. R., Fehsenfeld, F. C., Frost, G., Holloway, J. S., Hubler, G., Neuman, J. A., Ryerson, T. B., Warneke, C., and Wilson, J. C. (2008). "Sources of Particulate Matter in the Northeastern United States in Summer: 2. Evolution of Chemical and Microphysical Properties." 113, D08302, doi:10.1029/2007JD009241.

Brock C. A., Hudson, P. K., Lovejoy, E. R., Sullivan, A., Nowak, J. B., Huey, L. G., Cooper, O. R., de Gouw, J., Fehsenfeld, F. C., Holloway, J. S., Hübler, G., Lafleur, B. G., Neuman, J. A., Nicks, D. K., Orsini, D. A., Parrish, D. D., Ryerson, T. B., Tanner, D. J., Trainer, M., Warneke, C., Weber, R. J., Wilson, J. C. (2004). "Particle Characteristics Following Cloud-Modified Transport from Asia to North America." *J. Geophys. Res.* 109, D23S26, doi:10.1029/2003JD004198.

Brockmann, John E. (2001). "Sampling and Transport of Aerosols." *Aerosol Measurement: Principles, Techniques and Applications.* 2nd ed. Edited by P. A. Baron and K. Willeke, Wiley Interscience, New York.

Brown, R. C. (1993). *Air Filtration: An Integrated Approach to the Theory and Applications of Fibrous Filters.* Pergamon Press, Oxford.

Cheng, Y. S., and Yeh, Y. C. (1979). "Particle Bounce in Cascade Impactors." *Environ. Sci. Techno.* 13(11):1392-1396.

Cheng, Y. S., and Wang, C. S. (1981). "Motion of Particles in Bends of Circular Pipes." *Atmos. Environ.* 15:301-306.

Dahneke, B. (1971). "The Capture of Aerosol Particles by Surfaces." *J. Colloid Interface Sci.* 37:342-353.

Durst, F., and Melling, A. (1976). *Principles and Practice of Laser-Doppler Anemometry.* Academic press.

Durst, F., and Loy, T. (1985). "Investigations of Laminar Flow in a Pipe with Sudden Contraction of Cross Sectional Ares." *Computers anf Fluids.* 13:15-36.

Dye, J. E., and Baumgardner, D. (1984). "Evaluation of the Forward Scattering Spectrometer Probe. Part I: Electronic and Optical Studies." *J. Atmos. Oceanic Techno.* 1:329-344.

Ellenbecker, M. J., Leith, D., and Price, J. M. (1980). "Impaction and Particle Bounce at High Stokes Numbers." *J. Air Pollution Control Associ.* 30:1224-1227.

Fluent release 6.2.16, User's Guide, Fluent Incorporated.

Gesler, D. (2000). "Numerical Analysis of Sampling Efficiency in a Reduced Turbulence Inlet for Airborne Aerosol Sampling." MSME, Mechanical Engineering, University of Denver, Denver, CO.

Herman, M., Stratmann, F., Wilck, M., and Wiedensohler, A. (2001). "Sampling Characteristics of an Aircraft-Borne Aerosol Inlet Syatem." *J. Atmos. Oceanic Techno.* 18:7-19.

Hinds, W. C. (1982). *Aerosol Technology, properties, Behavior, and Measurement of Airborne particles.* John Wiley & Sons, New York.

Huebert, B. J., Lee, G., and Warren, W. (1990). "Airborne Aerosol Inlet Passing Efficiency Measurement." *J. Geophys. Res.* 95:16369-16381.

Huebert, B. J., Howell, S. G., Covert, D., Bertram, T., Clark, A., Anderson, J. R., Lafleur, B. G., Seebaugh, W. R., Wilson, J. C., Gesler, D., Blomquist, B., Fox, J. "PELTI: Measuring the Passing Efficiency of an Airborne Low Turbulence Aerosol Inlet." *Aerosol Sci. Techno.* 38:803-826.

King, W. D. (1984). "Air Flow and Particle Trajectories around Aircraft Fuselages I: Theory." *J. Atmos. Oceanic Techno.* 1:5-13.

Kline, J., Huebert, B., Howell, S., Blomquist, B., Zhuang, J., Bertram, T., and Carrillo, J. (2004). "Aerosol Composition and Size versus Altitude Measured from the C-130 during ACE-Asia." *J. Geophys. Res.* 109, D19S08, doi:10.1029/2004JD004540.

Langner, J., and Rodhe, H. (1991). "A Global 3-Dimensional Model of the Tropospheric Sulfur Cycle." *J. Atmos. Chemistry.* 13(3):225-263.

Marple V. A., and Liu, B. Y. H. (1974). "Characteristics of Laminar Jet Impactors." *Environ. Sci. Techno.* 8:648-654.

McFarland, A. R., Gong, H., Muyshondt, A., Wente, W. B., and Anand, N. K. (1997). "Aerosol Deposition in Bends with Turbulent Flow." *24th DOE/NRC Nuclear Air Cleaning and Treatment Conference* NUREG/CP-0153:441-459.

Morris, S. A., and Alexander, A. J. (1972). "An Investigation of Particle Trajectories in Two-Phase Flow Systems." *J. Fluid Mech.* 55(2):193-208.

Mullins, Benjamin. J., Agranovski, Igor. E., and Braddock, Roger. D. (2003). "Particle Bounce During Filteration on Wet and Dry Filters." *Aerosol Sci. Techno.* 37:587-600.

Pui, D. Y. H., Romay-Novas, F., and Liu, B. Y. H. (1987). "Experimental Study of Particle Deposition in Bends of Circular Cross Section." *Aerosol Sci. Techno.* 7: 301-315.

Raes, F., and Vandingenen, R. (1992). "Simulations of Condensation snd Cloud Condensation Nuclei from Biogenic SO2 in the Remote Marine Boundary-Layer." *J. Geophys. Res.* 97:12901-12912.

Seebaugh, W. R. (1991). "Application of Principles of Aerodynamics to Inlet/Diffuser Design." *Airborne Aerosol Inlet Worksho.* NCAR, Boulder, CO.

Seinfeld, John H. (1986). *Atmospheric Chemistry and Physics of Air Pollution.* John Wiley & Sons, Inc.

Soh, W. Y., Berger, S. A. (1984). "Laminar Entrance Flow in a Curved Pipe." *J. of Fluid Mechanics.* 148:109-135.

Tang, Y., Carmichael, G. R., Seinfeld, J. H., Dabdub, D., Weber, R. J., Huebert, B., Clarke, A. D., Guazzotti, S. A., Sodeman, D. A., Prather, K. A., Uno, I., Woo, J. H., Yienger, J. J., Streets, D. G., Quinn, P. K., Johnson, J. E., Song, C. H., Grassian, V. H., Sandu, A., Talbot, R. W., and Dibb, J. E. (2004)."Three-dimensional Simulation of Inorganic Aerosol Distribution in East Asia during Spring 2001." *J. Geophys. Res.* 109, D19S23, doi:10.1029/2003JD004201.

Tsai, C. J., Pui, D. Y. H., and Liu, B. Y. H. (1990). "Capture and Rebound of Small Particles Upon Impact with Solid Surfaces." *Aerosol Sci. Techno.* 12:497-507.

Tsai, C. J., and Pui, D. Y. H. (1990). "Numerical Study of Particle Deposition in Bends of a Circular Cross-Section- Laminar Flow Regime." *Aerosol Sci. Techno.* 12:813-831.

Ward-Smith, A. J. (1980). *The Fluid Dynamics of Flow in pipes and Ducts.* Clarendon press, Oxford.

White, Frank M. (2003). *Fluid Mechanics.* Mc Graw Hill: Von Hoffmann press.

Wilson, J.C. (1977). "Aerodynamic Particle Size Measurement by Laser-Doppler Velocimetry." Ph.D. Thesis, Particle Technology Laboratory, University of Minnesota, Minneapolis.

Wilson, J. C., and Liu, B. Y. H. (1980). "Aerodynamic Particle Size Measurement by Laser-Doppler Velocimetry." *J. Aerosol Sci.* 11:139-150.

Wilson, J. C., and Seebaugh, R. W. (2001). "Measurement of Aerosol from Aircraft." *Aerosol Measurement: Principles, Techniques and Applications.* 2nd ed. Edited by P. A. Baron and K. Willeke, Wiley Interscience, New York.

Wilson, J. C., Lafleur, B. G., Hilbert, H., Seebaugh, W. R., Fox, J., Brock, C. A., Huebert, B. J., Gesler, D. W., Mullen, J., and Reeves, J. M. (2004). "Function and Performance of a Low Turbulence Inlet for Sampling Super-micron Particles from Aircraft Platform." *Aerosol Sci. Techno.* 38:790-802.

Appendices

A. Details of Different Discretization Techniques in Fluent

The discretization of conservation equations of mass and momentum was discussed in Chapter 2. The details of different methods of discretization and the advantages of each method are presented in this appendix (Fluent, 6.2.16).

As mentioned earlier, Fluent uses a control-volume-based technique to convert the governing equations to algebraic equations that can be solved numerically. This control volume technique consists of integrating the governing equations about each control volume, yielding discrete equations that conserve each quantity on a control-volume basis.

Discretization of the governing equations can be illustrated by considering the steady-state conservation equation for transport of a scalar quantity ϕ. This is demonstrated by the following equation written in integral form for an arbitrary control volume V as follows:

$$\oint \rho \phi \vec{v} . d\vec{A} = \oint \Gamma_{\phi} \nabla \phi . d\vec{A} + \int_{V} S_{\phi} \, dV \tag{A.1}$$

ρ is the density, $\vec{v}$ is the velocity vector, $\vec{A}$ is the surface area vector, Γ_{ϕ} is the coefficient of diffusion for ϕ, $\nabla \phi$ is the gradient of ϕ and S_{ϕ} is the source of ϕ per unit volume.

Equation A.1 is applied to each control volume, or cell, in the computational domain. The two-dimensional, triangular cell shown in Figure A.1 is an example of such a control volume. Discretization of equation A.1 on a given cell yields

$$\sum_{f}^{N_{faces}} \rho_f \vec{v}_f \phi_f . \vec{A}_f = \sum_{f}^{N_{faces}} \Gamma_\phi (\nabla \phi)_n . \vec{A}_f + S_\phi V \qquad \text{(A.2)}$$

N_{faces} is the number of faces enclosing cell, ϕ_f is the value of ϕ convected through face f, $\rho_f \vec{v}_f \phi_f . \vec{A}_f$ is the mass flux through the face, $\vec{A}_f$ is the area of the face, $(\nabla \phi)_n$ is the magnitude of $\nabla \phi$, normal to face f and V is the cell volume.

The equations solved by Fluent take the same general form as the one given above and apply readily to multi-dimensional, unstructured meshes composed of arbitrary polyhedra.

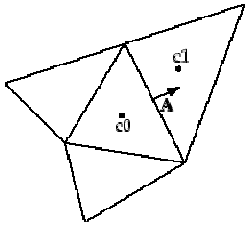

Figure A.1 Control volume used to illustrate discretization of a scalar transport equation.

By default, Fluent stores discrete values of the scalar ϕ at the cell centers C_0 and C_1 in Figure A.1. However, face values ϕ_f are required for the convection terms in Equation A.2 and must be interpolated from the cell center values. This is accomplished using an upwind scheme.

Upwinding means that the face value ϕ_f is derived from quantities in the cell upstream, or ``upwind," relative to the direction of the normal velocity v_n in Equation A.2. In Fluent several upwind schemes are available: first-order upwind, second-order upwind, power law, and QUICK. These schemes are described in detail in sections A.2 through A.6. The diffusion terms in Equation A.2 are central-differenced and are always second-order accurate.

A.1 First-Order Upwind Scheme

When first-order accuracy is desired, quantities at cell faces are determined by assuming that the cell-center values of any field variable represent a cell-average value and hold throughout the entire cell; the face quantities are identical to the cell quantities. Thus when first-order upwinding is selected, the face value ϕ_f is set equal to the cell-center value of ϕ in the upstream cell

A.2 power-Law Scheme

The power-law discretization scheme interpolates the face value of a variable, ϕ, using the exact solution to a one-dimensional convection-diffusion equation

$$\frac{\partial}{\partial x}(\rho u \phi) = \frac{\partial}{\partial x}\Gamma \frac{\partial \phi}{\partial x} \qquad \text{(A.3)}$$

Γ and ρu are constant across the interval ∂x. Equation A.3 can be integrated to yield the following solution describing how ϕ varies with x:

$$\frac{\phi(x)-\phi_0}{\phi_L-\phi_0}=\frac{\exp\ (Pe\ \frac{x}{L})-1}{\exp\ (Pe)-1} \tag{A.4}$$

$$\phi_0=\phi\ at\ x=0$$
$$\phi_L=\phi\ at\ x=L$$

Pe is the Peclet number:

$$Pe=\frac{\rho u L}{\Gamma} \tag{A.5}$$

The variation of ϕ (x) between *x=0* and *x=L* is depicted in Figure A.2 for a range of values of the Peclet number. Figure A.2 shows that for large *Pe*, the value of ϕ at *x=L/2* is approximately equal to the upstream value. This implies that when the flow is dominated by convection, interpolation can be accomplished by simply letting the face value of a variable be set equal to its ``upwind'' or upstream value. This is the standard first-order scheme for Fluent.

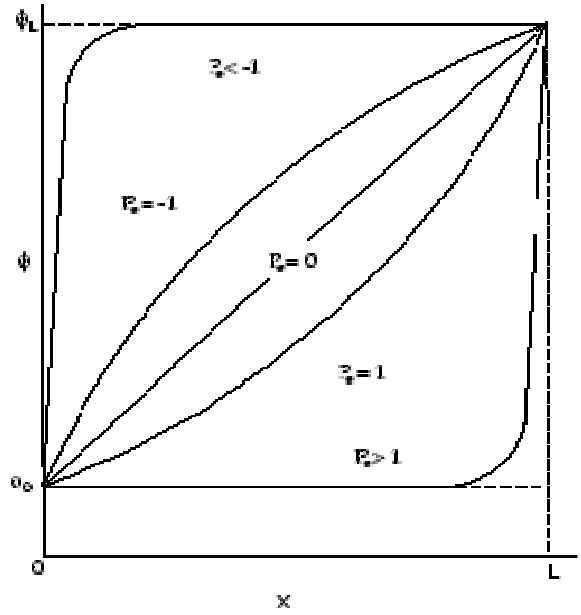

Figure A.2 Variation of a variable Φ between *x=0* and *x=L* (Equation A.3).

If the power-law scheme is selected, Fluent uses Equation A.4 in an equivalent ``power law" format as its interpolation scheme.

As discussed in Section A.2, Figure A.2 shows that for large *Pe*, the value of ϕ at *x=L/2* is approximately equal to the upstream value. When *Pe*=0 (no flow, or pure diffusion), Figure A.2 shows that ϕ may be interpolated using a simple linear average between the values at *x=0* and *x=L*. When the Peclet number has an intermediate value, the interpolated value for ϕ at *x=L/2* must be derived by applying the ``Power law" equivalent of Equation A.4.

A.3 Second-Order Upwind Scheme

When second-order accuracy is desired, quantities at cell faces are computed using a multidimensional linear reconstruction approach. In this approach, higher-order accuracy is achieved at cell faces through a Taylor series expansion of the cell-centered solution about the cell centroid. Thus when second-order upwinding is selected, the face value ϕ_f is computed using the following expression:

$$\phi_f = \phi + \nabla\phi . \Delta\vec{S} \tag{A.6}$$

ϕ and $\nabla\phi$ are the cell-centered value and its gradient in the upstream cell, and $\Delta\vec{S}$ is the displacement vector from the upstream cell centroid to the face centroid. This formulation requires the determination of the gradient $\nabla\phi$ in each cell. This gradient is computed using the divergence theorem, which in discrete form is written as:

$$\nabla\phi = \frac{1}{V}\sum_{f}^{N_{faces}} \tilde{\phi}_f \vec{A} \tag{A.7}$$

Here the face values $\tilde{\phi}_f$ are computed by averaging ϕ from the two cells adjacent to the face. Finally, the gradient $\nabla\phi$ is limited so that no new maxima or minima are introduced.

A.4 QUICK Scheme

For quadrilateral and hexahedral meshes, where unique upstream and downstream faces and cells can be identified, Fluent also provides the QUICK scheme for computing a higher-order value of the convected variable ϕ at a face. QUICK-type schemes are based on a weighted average of second-order-upwind and central interpolations of the variable. For the face "e" in Figure A.3, if the flow is from left to right, such a value can be written as: (A.8)

$$\phi_e = \theta \left[\frac{S_d}{S_c + S_d}\phi_P \; \frac{S_c}{S_c + S_d}\phi_E \right] + (1 - \theta) \left[\frac{S_u + 2S_c}{S_u + S_c}\phi_P - \frac{S_c}{S_u + S_c}\phi_W \right]$$

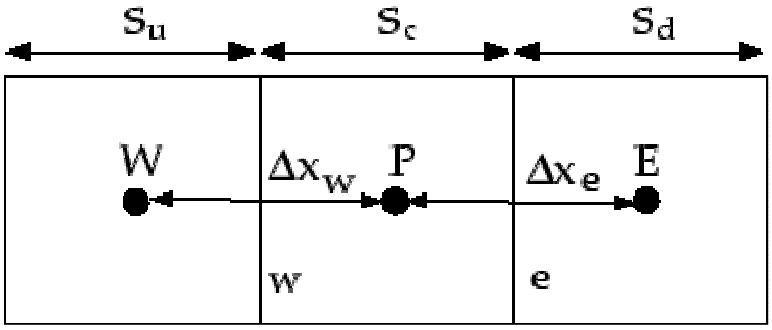

Figure A.3 One-Dimensional control volume.

θ=1 in the above equation results in a central second-order interpolation while θ=0 yields a second-order upwind value. The traditional QUICK scheme is obtained by setting θ=1/8. The implementation in Fluent uses a variable, solution-dependent value of θ, chosen so as to avoid introducing new solution extrema.

The QUICK scheme will typically be more accurate on structured grids aligned with the flow direction. Fluent allows the use of the QUICK scheme for unstructured or hybrid grids as well; in such cases the usual second-order upwind discretization scheme will be used at the faces of non-hexahedral (or non-quadrilateral, in 2D) cells. The second-order upwind scheme will also be used at partition boundaries when the parallel solver is used.

A.5 Central-Differencing Scheme

A second-order-accurate central-differencing discretization scheme is available for the momentum equations when you are using the LES turbulence model. This scheme provides improved accuracy for LES calculations.

The central-differencing scheme calculates the face value for a variable ϕ_f as follows:

$$\phi_{f,CD} = \frac{1}{2}(\phi_0 + \phi_1) + \frac{1}{2}(\nabla\phi_{r,0}.\vec{r}_0 + \nabla\phi_{r,1}.\vec{r}_1 \quad \text{(A.9)}$$

The indices 0 and 1 refer to the cells that share face f, $\nabla\phi_{r,0}$ and $\nabla\phi_{r,1}$ are the reconstructed gradients at cells 0 and 1, respectively, and $\vec{r}$ is the vector directed from the cell centroid toward the face centroid.

It is well known that central-differencing schemes can produce unbounded solutions and non-physical wiggles, which can lead to stability problems for the numerical procedure. These stability problems can often be avoided if a deferred approach is used for the central-differencing scheme. In this approach, the face value is calculated as follows:

$$\phi_f = \phi_{f,UP} + (\phi_{f,CD} - \phi_{f,UP}) \quad \text{(A.10)}$$

Up stands for upwind. As indicated, the upwind part is treated implicitly while the difference between the central-difference and upwind values is treated explicitly. Provided that the numerical solution converges, this approach leads to pure second-order differencing.

A.6 Linearized Form of the Discrete Equation

The discretized scalar transport equation A.2 contains the unknown scalar variable Φ at the cell center as well as the unknown values in surrounding neighbor cells. This equation will, in general, be non-linear with respect to these variables. A linearized form of Equation A.2 can be written as:

$$a_p \phi = \sum_{nb} a_{nb} \phi_{nb} + b \tag{A.11}$$

The subscript nb refers to neighbor cells, and a_p and a_{nb} are the linearized coefficients for ϕ and ϕ_{nb}.

The number of neighbors for each cell depends on the grid topology, but will typically equal the number of faces enclosing the cell (boundary cells being the exception).

Similar equations can be written for each cell in the grid. This results in a set of algebraic equations with a sparse coefficient matrix. For scalar equations, Fluent solves this linear system using a point implicit (Gauss-Seidel) linear equation solver in conjunction with an algebraic multigrid (AMG) method.

B. Computational Fluid Dynamics

B.1 Fluent Introduction

Fluent (6.2.16) is a finite volume based computational code used primarily for modeling fluid flow, heat transfer and chemical reaction in gas phase systems which are laminar, turbulent, incompressible or compressible. Fluent incorporates aspects of the finite element method and the spectral element method in solving complex fluid flow problems such as non-Newtonian and free-surface flows. Like many CFD codes, Fluent uses 'weighted residuals" in the formulation of its converged solutions, which is better known as the Galerkin method. Solutions are based on the conversation equations of mass (continuity), momentum, energy and chemical species using a control volume based finite difference method. Discretization schemes include first order upwind differencing, second order differencing, power law and QUICK (see Appendix A for details). Evaluating problems consists of four primary steps: (1) geometry generation, (2) grid generation, (3) solution and (4) post-processing.

B.2 Geometry and Grid Generation

Gambit (v-2.2.30) was used for all models evaluated in this study. Geometry and grid generation as well as the setting of preliminary boundary condition are not integrated with the Fluent software. Geometry and Grid files were created in Gambit and the grid files were imported into Fluent.

A 2-D geometry was created for the analysis of the diffuser used in this work. The determination of aerodynamic diameter and enhancement factor of the particles were carried out in 2-D models in Gambit and Fluent. A 3-D model was created for the

analysis of particle deposition in the bend of ACE-Asia and NOAA inlets. All the geometries were created in Cartesian space. Grid density, size, type and boundary conditions were then specified. The grid file was then written into Gambit and imported to Fluent.

B.3 Fluent Release 6.2.16

Fluent 6.2.16 is a menu driven software package. The menu structure is relatively easy to navigate and the on-line help available is quite informative. Fluent has a separate graphical window that allows display of the grid and post-processing results. The graphical features are mouse driven and allow zooming, rotating and translation. In viewing results, the mouse can also be used to query specific variable values within the domain. The results from these queries are display on the Fluent user interface window.

After importing the grid files into Fluent, the general parameters were then input under the 'Define' menu. Material properties (e.g. air for flow problem) and operating conditions (e.g. operating pressure). The specific boundary types (e.g. mass flow or velocity inlet, pressure outlet…) and respective boundary conditions were then input.

Also under the 'Define' menu the solution models were set (e.g. Energy for compressible flows), Viscous (laminar or turbulent flows), Discrete phase (particle transport). The solver options were also selected. All models in this study used the segregated, implicit solver (see appendix A for details).

B.4 Flows and Particle Trajectories Calculation

Discrete phase calculations were preformed in this study after the flow calculations were converged. Under the 'Solve' menu the solution controls for solving the flow were specified. Solutions controls include discretization technique selection (i.e.

SIMPLE, SIMPLEC…) and the under-relaxation parameters (i.e. velocity (momentum), pressure, density…). The variables within the domain were then initialized based on existing boundary conditions. Residual monitors were then set. The iterative solution process was then started. When all variable residuals are within the specified residuals, the solution is considered converged. To calculate the particle trajectory, the discrete phase solver was activated (after the flow was converged) in the 'Define' menu. Particle injections were specified in the 'Define: Injections' menu. Individual particles as well as particle injection files were generated. Particle information (i.e. diameter, temperature, material were specified for each injection. It was important at this point to set the discrete phase boundary conditions for all boundaries. This was done in the 'Define: Boundary Conditions' menu. Boundary conditions such as trap reflect and escape was set for all inlets, outlets and walls. The flow field was solved and trajectories were calculated accordingly. The case and data files were saved in Fluent.

B.5 Fluent Post-Processing

The post-processing tools facilitate the evaluation of solution results. Three primary tools are available: contour plots, vector plots, and a variety of reporting features. In addition, discrete phase (particle) tools are available. The scope of available tools extends beyond what is described here.

Contour plots are accessed through the 'Display' menu and provide graphical information of the non-directional values of a multitude of variables. Each plot divides the specified (or default maximum and minimum) range of a particular variable into a set number of contours of constant value. Each division has a different color. A color bar on

the left side of the graphical display window indicates the value of a variable for a given color band.

Vector plots are also accessed through the 'Display' menu and provide magnitude and directional graphical information for a variety of variables at node points. Velocities, for instance, are shown with vectors indicating direction and whose length is proportional to the velocity magnitude at a specified node point (velocities are stored on the nodes of the staggered grid and scalars at the grid nodes).

Fluent provides additional tools that allow non-graphical reporting of variables at specific locations. Under the 'Report' menu fluxes, integral averages and listing of variable values at (or across) specified boundaries/surfaces are available. Surfaces, lines and points of interest other than the boundaries can be specified under the 'Surface' menu and observed in the same manner. In addition, under the 'File' menu, external ASCII files (called 'profiles') can be created which include nodal information about any variable within the domain. This is helpful in performing external data comparisons and evaluations.

Under the 'Display: particle Tracks' menu, Fluent allows graphical visualization of particle trajectories. The 'Track' button activates the particle trajectory calculation. Dependent upon how boundary discrete phase conditions have been set (i.e. escape, trap…) particles pass through the domain (or get trapped). A report of the total number of particles processed (in the case of a particle injection with more than 1 particle), the number trapped and the number escaped is displayed in the user interface window. This is useful of evaluating particle deposition efficiently within the domain. The 'Display' button shows the particle trajectories through the domain in the graphical window**.**

C. Slip Correction Factor for 1-20 μm particles

Table C.1 Slip correction factor for particles 1-20 microns in standard air (Equation 2.13).

Dp(micron)	Cc(Slip Correction)	Dp(micron)	Cc(Slip Correction)
1	1.165	11	1.015
2	1.082	12	1.014
3	1.055	13	1.013
4	1.041	14	1.012
5	1.033	15	1.011
6	1.027	16	1.01
7	1.023	17	1.01
8	1.02	18	1.009
9	1.018	19	1.009
10	1.016	20	1.008

D. Specifications of Commercially available Velocimeters

The specifications of two types of commercially available velocimeters given in this appendix correspond to the products of Measurement Science Enterprise, Inc. **www.measurementsci.com**.

D.1 Micro-V system

The micro-V is a non-intrusive, time of flight, velocity sensor, capable of measuring velocity of the flow or moving objects at a fixed distance from the sensor surface. The sensor is extremely compact, has no moving parts, does not include any active components, and is suitable for use in harsh environments. The sensor uses diffractive optic elements to project two parallel light sheets (~ 300 micron long and 100 micron apart). The light scattered by the particles in the flow or by a moving surface is collected through the same sensor element. The light source and the electronics are connected to the sensor via optical fibers. The opto-electronics enclosure can be located several meters from the sensor.

When a particle travels through the optical probe volume, the receiver detects two bouts of scattered light. The processor uses an auto correlation- based algorithm to determine time elapsed between the two peaks, t, from which the velocity of the particle is calculated. This processor runs on Windows and provides an easy-to-use graphical interface.

The probe volume of micro-V is 0.0075 mm^3, i.e. (250 µm x 100 µm x 300 µm). The sensor body dimensions are 9 mm diameter x 75 mm length. The velocity measurement range of the instrument is 0.001-30 m/s. The laser power in the probe is 7

mw, and the wavelength of the laser light is 658 nm. The operating temperature range of the system is 5-40 °C.

D.2 Mini LDV

The Mini LDV unit contains a laser, miniature beam shaping optics, receiving optics, and a detection system. The sensor is 38 mm in diameter and 100 mm long, and the fixed distance between the sensor and the probe volume can be selected between 33 mm to 240 mm. Mini LDV simplifies measurement of the speed of moving surfaces, fiber, and particles in air and liquid. Optional or custom systems can be supplied including automated traversing systems for automatic velocity profiling.

The Mini LDV probe contains a laser diode, diffraction grating beam-splitter, transmitting and receiving optics. The receiving fiber optic cable is connected to the sensor drive, which contains the photo detector and power supply for the laser. The output from the sensor drive is band pass filtered and digitized before being transferred to a PC for processing and output.

The software is a general- purpose data acquisition and processing package with output of mean values and time records of velocity. When used with a traversing system, automatic velocity profiles can be obtained.

There are three different Mini LDVs available which are primarily different in their probe volume, working distance, fringe spacing, and the operating velocity range.

Table D.1 shows the specifications of Micro-V system and three Mini LDV products.

Table D.1 Comparison of different velocimeters to measure particle velocity.

Product	Micro-V	Mini LDV_33	Mini LDV_100	Mini LDV_240
Principle of Operation	TOF laser velocimetry	Doppler effect	Doppler effect	Doppler effect
Laser Wavelength, λ	658 nm	660 nm	660 nm	660 nm
Laser Power	7 mW	60 mW	60 mW	60 mW
Laser Cable Length	5 m	5 m	5 m	5 m
Velocity	0.001-30 m/s	0.004-46 m/s 0.018-460m/s	0.008-93 m/s 0.040-930 m/s	0.012-140 m/s 0.050-1400 m/s
Resolution	0.1 %	0.2 %	0.2 %	0.2 %
Accuracy	0.3 %	0.3 %	0.3 %	0.3 %
Probe Volume (dx dy dz), μm^3	250x100x300	30x60x200	70x70x500	100x200x1200
Standoff distance in air, mm	7.5 mm	33 mm	100 mm	240 mm
Fringe Spacing, μm	100 μm	4.6 μm	4 μm	14 μm
Body Size	9 mm dia. x 75 mm length	30 mm dia. x 160 mm length	30 mm dia. x 160 mm length	30 mm dia. x 160 mm length
Temperature Range	5-40 °C	0-40 °C	0-40 °C	0-40 °C
PC Requirements	PCI bus, windows 2000 or XP, IP4	PCI bus, windows 2000, IP4	PCI bus, windows 2000, IP4	PCI bus, windows 2000, IP4
Photo Detector Dynamic Range	DC to MHz	DC to 100 KHz, 2 MHz, 10 MHz or 100 MHz	DC to 100 KHz, 2 MHz, 10 MHz or 100 MHz	DC to 100 KHz, 2 MHz, 10 MHz or 100 MHz
Timestamp Resolution	2 ns	2 ns	2 ns	2 ns
Max. Output Data Rate	10 KHz	10 KHz	10 KHz	10 KHz
Bandwidth		100 MHz	100 MHz	100 MHz

E. Variation of Pressure, Temperature, Density and Viscosity with Altitude in Troposphere and Stratosphere regions

Table E.1 Variation of air properties with altitude.

Altitude, Z (km)	Pressure, P (Pa)	Temperature, T (K)	Density, ρ Ideal gas law (kg/m3)	Density, ρ Imperical eqn. (kg/m3)	Viscosity, μ (Kg/m.s)
0	101,300	288.15	1.225	1.211	1.7893E-05
0.1	100,104	287.5	1.214	1.199	1.7861E-05
0.2	98,920	286.85	1.202	1.187	1.7828E-05
0.3	97,746	286.2	1.190	1.176	1.7796E-05
0.4	96,585	285.55	1.179	1.165	1.7764E-05
0.5	95,434	284.9	1.168	1.153	1.7731E-05
0.6	94,295	284.25	1.156	1.142	1.7699E-05
0.7	93,166	283.6	1.145	1.131	1.7667E-05
0.8	92,049	282.95	1.134	1.120	1.7634E-05
0.9	90,942	282.3	1.123	1.109	1.7602E-05
1	89,846	281.65	1.112	1.098	1.7569E-05
1.1	88,761	281	1.101	1.087	1.7537E-05
1.2	87,687	280.35	1.090	1.076	1.7504E-05
1.3	86,623	279.7	1.079	1.066	1.7471E-05
1.4	85,569	279.05	1.069	1.055	1.7439E-05
1.5	84,526	278.4	1.058	1.045	1.7406E-05
1.6	83,494	277.75	1.048	1.034	1.7373E-05
1.7	82,471	277.1	1.037	1.024	1.7341E-05
1.8	81,459	276.45	1.027	1.014	1.7308E-05
1.9	80,457	275.8	1.017	1.003	1.7275E-05
2	79,465	275.15	1.007	0.993	1.7242E-05
2.1	78,482	274.5	0.997	0.983	1.7210E-05
2.2	77,510	273.85	0.987	0.973	1.7177E-05
2.3	76,547	273.2	0.977	0.964	1.7144E-05
2.4	75,594	272.55	0.967	0.954	1.7111E-05
2.5	74,651	271.9	0.957	0.944	1.7078E-05
2.6	73,717	271.25	0.947	0.934	1.7045E-05
2.7	72,793	270.6	0.938	0.925	1.7012E-05
2.8	71,878	269.95	0.928	0.915	1.6979E-05
2.9	70,973	269.3	0.919	0.906	1.6946E-05
3	70,077	268.65	0.909	0.897	1.6912E-05
3.1	69,189	268	0.900	0.887	1.6879E-05
3.2	68,312	267.35	0.891	0.878	1.6846E-05
3.3	67,443	266.7	0.881	0.869	1.6813E-05
3.4	66,583	266.05	0.872	0.860	1.6780E-05
3.5	65,732	265.4	0.863	0.851	1.6746E-05
3.6	64,889	264.75	0.854	0.842	1.6713E-05

Altitude, Z (km)	Pressure, P (Pa)	Temperature, T (K)	Density, ρ Ideal gas law (kg/m3)	Density, ρ Imperical eqn. (kg/m3)	Viscosity, μ (Kg/m.s)
3.7	64,056	264.1	0.845	0.833	1.6680E-05
3.8	63,231	263.45	0.837	0.825	1.6646E-05
3.9	62,415	262.8	0.828	0.816	1.6613E-05
4	61,608	262.15	0.819	0.807	1.6579E-05
4.1	60,809	261.5	0.811	0.799	1.6546E-05
4.2	60,018	260.85	0.802	0.790	1.6512E-05
4.3	59,235	260.2	0.793	0.782	1.6479E-05
4.4	58,461	259.55	0.785	0.774	1.6445E-05
4.5	57,696	258.9	0.777	0.765	1.6412E-05
4.6	56,938	258.25	0.768	0.757	1.6378E-05
4.7	56,188	257.6	0.760	0.749	1.6344E-05
4.8	55,447	256.95	0.752	0.741	1.6311E-05
4.9	54,713	256.3	0.744	0.733	1.6277E-05
5	53,987	255.65	0.736	0.725	1.6243E-05
5.1	53,269	255	0.728	0.717	1.6209E-05
5.2	52,559	254.35	0.720	0.709	1.6176E-05
5.3	51,857	253.7	0.712	0.702	1.6142E-05
5.4	51,162	253.05	0.705	0.694	1.6108E-05
5.5	50,474	252.4	0.697	0.686	1.6074E-05
5.6	49,794	251.75	0.689	0.679	1.6040E-05
5.7	49,122	251.1	0.682	0.671	1.6006E-05
5.8	48,457	250.45	0.674	0.664	1.5972E-05
5.9	47,799	249.8	0.667	0.657	1.5938E-05
6	47,149	249.15	0.660	0.649	1.5904E-05
6.1	46,506	248.5	0.652	0.642	1.5870E-05
6.2	45,869	247.85	0.645	0.635	1.5836E-05
6.3	45,240	247.2	0.638	0.628	1.5801E-05
6.4	44,618	246.55	0.631	0.621	1.5767E-05
6.5	44,003	245.9	0.624	0.614	1.5733E-05
6.6	43,395	245.25	0.617	0.607	1.5699E-05
6.7	42,793	244.6	0.610	0.600	1.5664E-05
6.8	42,199	243.95	0.603	0.593	1.5630E-05
6.9	41,611	243.3	0.596	0.587	1.5596E-05
7	41,030	242.65	0.589	0.580	1.5561E-05
7.1	40,455	242	0.583	0.573	1.5527E-05
7.2	39,887	241.35	0.576	0.567	1.5492E-05
7.3	39,325	240.7	0.569	0.560	1.5458E-05
7.4	38,770	240.05	0.563	0.554	1.5423E-05
7.5	38,221	239.4	0.556	0.547	1.5389E-05
7.6	37,678	238.75	0.550	0.541	1.5354E-05

Altitude, Z (km)	Pressure, P (Pa)	Temperature, T (K)	Density, ρ Ideal gas law (kg/m3)	Density, ρ Imperical eqn. (kg/m3)	Viscosity, μ (Kg/m.s)
7.7	37,142	238.1	0.544	0.535	1.5319E-05
7.8	36,612	237.45	0.537	0.529	1.5285E-05
7.9	36,088	236.8	0.531	0.523	1.5250E-05
8	35,570	236.15	0.525	0.516	1.5215E-05
8.1	35,058	235.5	0.519	0.510	1.5180E-05
8.2	34,552	234.85	0.513	0.504	1.5146E-05
8.3	34,052	234.2	0.507	0.498	1.5111E-05
8.4	33,558	233.55	0.501	0.493	1.5076E-05
8.5	33,070	232.9	0.495	0.487	1.5041E-05
8.6	32,587	232.25	0.489	0.481	1.5006E-05
8.7	32,111	231.6	0.483	0.475	1.4971E-05
8.8	31,639	230.95	0.478	0.470	1.4936E-05
8.9	31,174	230.3	0.472	0.464	1.4901E-05
9	30,714	229.65	0.466	0.458	1.4866E-05
9.1	30,260	229	0.461	0.453	1.4831E-05
9.2	29,811	228.35	0.455	0.447	1.4796E-05
9.3	29,367	227.7	0.450	0.442	1.4761E-05
9.4	28,929	227.05	0.444	0.437	1.4725E-05
9.5	28,496	226.4	0.439	0.431	1.4690E-05
9.6	28,068	225.75	0.433	0.426	1.4655E-05
9.7	27,646	225.1	0.428	0.421	1.4620E-05
9.8	27,229	224.45	0.423	0.416	1.4584E-05
9.9	26,817	223.8	0.418	0.411	1.4549E-05
10	26,410	223.15	0.413	0.406	1.4513E-05
10.1	26,007	222.5	0.407	0.401	1.4478E-05
10.2	25,610	221.85	0.402	0.396	1.4442E-05
10.3	25,218	221.2	0.397	0.391	1.4407E-05
10.4	24,831	220.55	0.392	0.386	1.4371E-05
10.5	24,449	219.9	0.388	0.381	1.4336E-05
10.6	24,071	219.25	0.383	0.376	1.4300E-05
10.7	23,698	218.6	0.378	0.372	1.4265E-05
10.8	23,330	217.95	0.373	0.367	1.4229E-05
10.9	22,966	217.3	0.368	0.362	1.4193E-05
11	22,607	216.65	0.364	0.358	1.4157E-05
11.1	22,253	216.65	0.358	0.352	1.4157E-05
11.2	21,905	216.65	0.352	0.347	1.4157E-05
11.3	21,562	216.65	0.347	0.341	1.4157E-05
11.4	21,225	216.65	0.341	0.336	1.4157E-05
11.5	20,892	216.65	0.336	0.330	1.4157E-05
11.6	20,565	216.65	0.331	0.325	1.4157E-05

Altitude, Z (km)	Pressure, P (Pa)	Temperature, T (K)	Density, ρ Ideal gas law (kg/m3)	Density, ρ Imperical eqn. (kg/m3)	Viscosity, μ (Kg/m.s)
11.7	20,243	216.65	0.326	0.320	1.4157E-05
11.8	19,926	216.65	0.321	0.315	1.4157E-05
11.9	19,614	216.65	0.316	0.310	1.4157E-05
12	19,307	216.65	0.311	0.305	1.4157E-05
12.1	19,005	216.65	0.306	0.301	1.4157E-05
12.2	18,708	216.65	0.301	0.296	1.4157E-05
12.3	18,415	216.65	0.296	0.291	1.4157E-05
12.4	18,127	216.65	0.292	0.287	1.4157E-05
12.5	17,843	216.65	0.287	0.282	1.4157E-05
12.6	17,563	216.65	0.283	0.278	1.4157E-05
12.7	17,289	216.65	0.278	0.273	1.4157E-05
12.8	17,018	216.65	0.274	0.269	1.4157E-05
12.9	16,752	216.65	0.270	0.265	1.4157E-05
13	16,489	216.65	0.265	0.261	1.4157E-05
13.1	16,231	216.65	0.261	0.257	1.4157E-05
13.2	15,977	216.65	0.257	0.253	1.4157E-05
13.3	15,727	216.65	0.253	0.249	1.4157E-05
13.4	15,481	216.65	0.249	0.245	1.4157E-05
13.5	15,238	216.65	0.245	0.241	1.4157E-05
13.6	15,000	216.65	0.241	0.237	1.4157E-05
13.7	14,765	216.65	0.238	0.234	1.4157E-05
13.8	14,534	216.65	0.234	0.230	1.4157E-05
13.9	14,306	216.65	0.230	0.226	1.4157E-05
14	14,083	216.65	0.227	0.223	1.4157E-05
14.1	13,862	216.65	0.223	0.219	1.4157E-05
14.2	13,645	216.65	0.220	0.216	1.4157E-05
14.3	13,431	216.65	0.216	0.212	1.4157E-05
14.4	13,221	216.65	0.213	0.209	1.4157E-05
14.5	13,014	216.65	0.209	0.206	1.4157E-05
14.6	12,811	216.65	0.206	0.203	1.4157E-05
14.7	12,610	216.65	0.203	0.199	1.4157E-05
14.8	12,413	216.65	0.200	0.196	1.4157E-05
14.9	12,218	216.65	0.197	0.193	1.4157E-05
15	12,027	216.65	0.193	0.190	1.4157E-05
15.1	11,839	216.65	0.190	0.187	1.4157E-05
15.2	11,653	216.65	0.187	0.184	1.4157E-05
15.3	11,471	216.65	0.185	0.181	1.4157E-05
15.4	11,291	216.65	0.182	0.179	1.4157E-05
15.5	11,115	216.65	0.179	0.176	1.4157E-05
15.6	10,941	216.65	0.176	0.173	1.4157E-05

15.7	10,769	216.65	0.173	0.170	1.4157E-05
15.8	10,601	216.65	0.171	0.168	1.4157E-05
15.9	10,435	216.65	0.168	0.165	1.4157E-05
16	10,272	216.65	0.165	0.162	1.4157E-05
16.1	10,111	216.65	0.163	0.160	1.4157E-05
16.2	9,952	216.65	0.160	0.157	1.4157E-05
16.3	9,797	216.65	0.158	0.155	1.4157E-05
16.4	9,643	216.65	0.155	0.153	1.4157E-05
16.5	9,492	216.65	0.153	0.150	1.4157E-05
16.6	9,344	216.65	0.150	0.148	1.4157E-05
16.7	9,198	216.65	0.148	0.145	1.4157E-05
16.8	9,054	216.65	0.146	0.143	1.4157E-05
16.9	8,912	216.65	0.143	0.141	1.4157E-05
17	8,772	216.65	0.141	0.139	1.4157E-05
17.1	8,635	216.65	0.139	0.137	1.4157E-05
17.2	8,500	216.65	0.137	0.134	1.4157E-05
17.3	8,367	216.65	0.135	0.132	1.4157E-05
17.4	8,236	216.65	0.132	0.130	1.4157E-05
17.5	8,107	216.65	0.130	0.128	1.4157E-05
17.6	7,980	216.65	0.128	0.126	1.4157E-05
17.7	7,855	216.65	0.126	0.124	1.4157E-05
17.8	7,732	216.65	0.124	0.122	1.4157E-05
17.9	7,611	216.65	0.122	0.120	1.4157E-05
18	7,492	216.65	0.121	0.119	1.4157E-05
18.1	7,375	216.65	0.119	0.117	1.4157E-05
18.2	7,259	216.65	0.117	0.115	1.4157E-05
18.3	7,146	216.65	0.115	0.113	1.4157E-05
18.4	7,034	216.65	0.113	0.111	1.4157E-05
18.5	6,924	216.65	0.111	0.110	1.4157E-05
18.6	6,815	216.65	0.110	0.108	1.4157E-05
18.7	6,709	216.65	0.108	0.106	1.4157E-05
18.8	6,603	216.65	0.106	0.104	1.4157E-05
18.9	6,500	216.65	0.105	0.103	1.4157E-05
19	6,398	216.65	0.103	0.101	1.4157E-05
19.1	6,298	216.65	0.101	0.100	1.4157E-05
19.2	6,200	216.65	0.100	0.098	1.4157E-05
19.3	6,103	216.65	0.098	0.097	1.4157E-05
19.4	6,007	216.65	0.097	0.095	1.4157E-05
19.5	5,913	216.65	0.095	0.094	1.4157E-05
19.6	5,820	216.65	0.094	0.092	1.4157E-05
19.7	5,729	216.65	0.092	0.091	1.4157E-05
19.8	5,640	216.65	0.091	0.089	1.4157E-05
19.9	5,551	216.65	0.089	0.088	1.4157E-05
20	5,464	216.65	0.088	0.086	1.4157E-05

F. Response Matrices for Cases with Different Ambient Conditions and Inlet Geometry.

F.1a Response matrix for ACE-Asia, TAS=113.6 m/s, P=84,600 Pa.

Velocity Channels	Velocity Range	32 ≤ Dp < 34	30 ≤ Dp < 32	28 ≤ Dp < 30	26 ≤ Dp < 28	24 ≤ Dp < 26	22 ≤ Dp < 24	20 ≤ Dp < 22	18 ≤ Dp < 20	16 ≤ Dp < 18	14 ≤ Dp < 16	6 ≤ Dp <14	4 ≤ Dp <6	2 ≤ Dp < 4	1 ≤ Dp < 2
1	111.99 ≤ Vp < 112.18	12													
2	111.75 ≤ Vp < 111.99		12												
3	111.48 ≤ Vp < 111.75			12											
4	111.15 ≤ Vp < 111.48				12										
5	110.77 ≤ Vp < 111.15					12									
6	110.32 ≤ Vp < 110.77						12								
7	109.82 ≤ Vp < 110.32							12							
8	109.28 ≤ Vp < 109.82								12						
9	108.71 ≤ Vp < 109.28	1	1							12					
10	108.17 ≤ Vp < 108.71			1	1						12				
11	107.54 ≤ Vp < 108.17	1	2			1	1					48			
12	106.42 ≤ Vp < 107.54			1	1	2	1	2	1			7	12		
13	102.00 ≤ Vp < 106.42	1	1	2	1	1	1	2	4	4	4	22		12	
14	100.01 ≤ Vp < 102.00														11
Total # of Particles in each size range		15	16	16	15	16	15	16	17	16	16	77	12	12	11

Note: The empty spaces are filled with zero in actual response matrix calculations.

F.1b Response matrix for ACE-Asia, TAS=113.6 m/s, P=84,600 Pa, fractional form.

Velocity Channels	Velocity Range	32 ≤ Dp < 34	30 ≤ Dp < 32	28 ≤ Dp < 30	26 ≤ Dp < 28	24 ≤ Dp < 26	22 ≤ Dp < 24	20 ≤ Dp < 22	18 ≤ Dp < 20	16 ≤ Dp < 18	14 ≤ Dp < 16	6 ≤ Dp <14	4 ≤ Dp <6	2 ≤ Dp < 4	1 ≤ Dp < 2
1	111.99 ≤ Vp < 112.18	0.8	0	0	0	0	0	0	0	0	0	0	0	0	0
2	111.75 ≤ Vp < 111.99	0	0.75	0	0	0	0	0	0	0	0	0	0	0	0
3	111.48 ≤ Vp < 111.75	0	0	0.75	0	0	0	0	0	0	0	0	0	0	0
4	111.15 ≤ Vp < 111.48	0	0	0	0.8	0	0	0	0	0	0	0	0	0	0
5	110.77 ≤ Vp < 111.15	0	0	0	0	0.75	0	0	0	0	0	0	0	0	0
6	110.32 ≤ Vp < 110.77	0	0	0	0	0	0.8	0	0	0	0	0	0	0	0
7	109.82 ≤ Vp < 110.32	0	0	0	0	0	0	0.75	0	0	0	0	0	0	0
8	109.28 ≤ Vp < 109.82	0	0	0	0	0	0	0	0.71	0	0	0	0	0	0
9	108.71 ≤ Vp < 109.28	0.07	0.06	0	0	0	0	0	0	0.75	0	0	0	0	0
10	108.17 ≤ Vp < 108.71	0	0	0.06	0.07	0	0	0	0	0	0.75	0	0	0	0
11	107.54 ≤ Vp < 108.17	0.07	0.13	0	0	0.06	0.07	0	0	0	0	0.62	0	0	0
12	106.42 ≤ Vp < 107.54	0	0	0.06	0.07	0.13	0.07	0.13	0.06	0	0	0.09	1	0	0
13	102.00 ≤ Vp < 106.42	0.07	0.06	0.13	0.07	0.06	0.07	0.13	0.24	0.25	0.25	0.29	0	1	0
14	100.01 ≤ Vp < 102.00	0	0	0	0	0	0	0	0	0	0	0	0	0	1
Total # of Particles in each size range		1	1	1	1	1	1	1	1	1	1	1	1	1	1

F.1c Inverse response matrix for ACE-Asia, TAS=113.6 m/s, P=84,600 Pa.

1.25	0	0	0	0	0	0	0	0	0	0	0	0	0
0	1.33	0	0	0	0	0	0	0	0	0	0	0	0
0	0	1.33	0	0	0	0	0	0	0	0	0	0	0
0	0	0	1.25	0	0	0	0	0	0	0	0	0	0
0	0	0	0	1.33	0	0	0	0	0	0	0	0	0
0	0	0	0	0	1.25	0	0	0	0	0	0	0	0
0	0	0	0	0	0	1.33	0	0	0	0	0	0	0
0	0	0	0	0	0	0	1.4	0	0	0	0	0	0
-0.1	-0.1	0	0	0	0	0	0	1.3	0	0	0	0	0
0	0	-0.1	-0.1	0	0	0	0	0	1.33	0	0	0	0
-0.1	-0.3	0	0	-0.1	-0.1	0	0	0	0	1.6	0	0	0
0	0.02	-0.1	-0.1	-0.2	-0.1	-0.2	-0.1	0	0	-0.1	1	0	0
-0	0.02	-0.1	-0.1	-0	-0	-0.2	-0.3	-0.3	-0.33	-0.5	0	1	0
0	0	0	0	0	0	0	0	0	0	0	0	0	1

F.2a Response matrix for PELTI, TAS=115.6 m/s, P=93,521 Pa.

Velocity Channels	Velocity Range	25 ≤ Dp < 30	20≤ Dp< 25	15 ≤ Dp < 20	10 ≤ Dp < 15	8 ≤ Dp < 10	6 ≤ Dp < 8	4 ≤ Dp < 6	2 ≤ Dp < 4	1 ≤ Dp < 2
1	110.01 ≤ Vp < 111.15	12								
2	108.39 ≤ Vp < 110.01		12							
3	106.06 ≤ Vp < 108.39	2		12						
4	102.91 ≤ Vp < 106.06	3	2		12					
5	101.73 ≤ Vp < 102.91		1	2		12				
6	101.03 ≤ Vp < 101.73						11			
7	100.31 ≤ Vp <101.03		2	1				11		
8	96.60 ≤ Vp < 100.31			2	6	7	11	2	11	
9	94.29 ≤ Vp < 96.60						3			11
Total # of Particles in each size range		17	17	17	18	19	25	13	11	11

Note: The empty spaces are filled with zero in actual response matrix calculations.

F.2b Response matrix in fractional form for PELTI, TAS=115.6 m/s, P=93,521 Pa.

Velocity Channels	Velocity Range	25 ≤ Dp< 30	20≤ Dp< 25	15 ≤ Dp < 20	10 ≤ Dp < 15	8 ≤ Dp < 10	6 ≤ Dp < 8	4 ≤ Dp < 6	2 ≤ Dp < 4	1≤ Dp < 2
1	110.01 ≤ Vp < 111.15	0.71	0	0	0	0	0	0	0	0
2	108.39 ≤ Vp < 110.01	0	0.71	0	0	0	0	0	0	0
3	106.06 ≤ Vp < 108.39	0.12	0	0.71	0	0	0	0	0	0
4	102.91 ≤ Vp < 106.06	0.18	0.12	0	0.67	0	0	0	0	0
5	101.73 ≤ Vp < 102.91	0	0.06	0.12	0	0.63	0	0	0	0
6	101.03 ≤ Vp < 101.73	0	0	0	0	0	0.44	0	0	0
7	100.31 ≤ Vp <101.03	0	0.12	0.06	0	0	0	0.85	0	0
8	96.60 ≤ Vp < 100.31	0	0	0.12	0.33	0.37	0.44	0.15	1	0
9	94.29 ≤ Vp < 96.60	0	0	0	0	0	0.12	0	0	1
Total # of Particles in each size range		1	1	1	1	1	1	1	1	1

F.2c Inverse response matrix for PELTI, TAS=115.6 m/s, P=93,521 Pa.

1.42	0	0	0	0	0	0	0	0
0	1.42	0	0	0	0	0	0	0
-0.2	0	1.42	0	0	0	0	0	0
-0.4	-0.25	0	1.5	0	0	0	0	0
0.04	-0.13	-0.3	0	1.58	0	0	0	0
0	0	0	0	0	2.27	0	0	0
0.02	-0.2	-0.1	0	0	0	1.18	0	0
0.13	0.16	-0.1	-0.5	-0.6	-1	-0.18	1	0
0	0	0	0	0	-0.3	0	0	1

F.3a Response matrix for PELTI, TAS=119.2 m/s, P=86,168 Pa.

Velocity Channels	Velocity Range	25 ≤ Dp < 30	20≤ Dp< 25	15 ≤ Dp < 20	10 ≤ Dp < 15	8 ≤ Dp < 10	6 ≤ Dp < 8	4 ≤ Dp < 6	2 ≤ Dp < 4	1 ≤ Dp < 2
1	109.83 ≤ Vp < 111.54	12								
2	107.53 ≤ Vp < 109.83		12							
3	104.45 ≤ Vp < 107.53	3		11						
4	100.511 ≤ Vp < 104.45	2	3	1	11					
5	99.00 ≤ Vp < 100.51		2	2		11				
6	97.79 ≤ Vp < 99.00			1	1		11			
7	95.95 ≤ Vp <97.79			2	4	5	6	11		
8	92.32 ≤ Vp < 95.95				2	11			10	
9	90.83 ≤ Vp < 92.32									10
Total # of Particles in each size range		17	17	17	18	27	17	11	10	10

Note: The empty spaces are filled with zero in actual response matrix calculations.

F.3b Response matrix in fractional form for PELTI, TAS=119.2 m/s, P=86,168 Pa.

Velocity Channels	Velocity Range	25 ≤ Dp < 30	20≤ Dp< 25	15 ≤ Dp < 20	10 ≤ Dp < 15	8 ≤ Dp < 10	6 ≤ Dp < 8	4 ≤ Dp < 6	2 ≤ Dp < 4	1 ≤ Dp < 2
1	109.83 ≤ Vp < 111.54	0.71	0	0	0	0	0	0	0	0
2	107.53 ≤ Vp < 109.83	0	0.71	0	0	0	0	0	0	0
3	104.45 ≤ Vp < 107.53	0.18	0	0.65	0	0	0	0	0	0
4	100.511 ≤ Vp < 104.45	0.12	0.18	0.06	0.61	0	0	0	0	0
5	99.00 ≤ Vp < 100.51	0	0.12	0.12	0	0.41	0	0	0	0
6	97.79 ≤ Vp < 99.00	0	0	0.06	0.06	0	0.65	0	0	0
7	95.95 ≤ Vp <97.79	0	0	0.12	0.22	0.19	0.35	1	0	0
8	92.32 ≤ Vp < 95.95	0	0	0	0.11	0.41	0	0	1	0
9	90.83 ≤ Vp < 92.32	0	0	0	0	0	0	0	0	1
Total # of Particles in each size range		1	1	1	1	1	1	1	1	1

F.3c Inverse response matrix for PELTI, TAS=119.2 m/s, P=86,168 Pa.

1.42	0	0	0	0	0	0	0	0
0	1.42	0	0	0	0	0	0	0
-0.39	0	1.55	0	0	0	0	0	0
-0.24	-0.41	-0.1	1.64	0	0	0	0	0
0.11	-0.41	-0.4	0	2.45	0	0	0	0
0.06	0.04	-0.1	-0.1	0	1.55	0	0	0
0.06	0.15	-0	-0.3	-0.45	-0.5	1	0	0
-0.02	0.21	0.2	-0.2	-1	0	0	1	0
0	0	0	0	0	0	0	0	1

F.4a Response matrix for PELTI, TAS=120.4 m/s, P=74,920 Pa.

Velocity Channels	Velocity Range	25 ≤ Dp < 30	20≤ Dp< 25	15 ≤ Dp < 20	10 ≤ Dp < 15	8 ≤ Dp < 10	6 ≤ Dp < 8	4 ≤ Dp < 6	2 ≤ Dp < 4	1 ≤ Dp < 2
1	109.32 ≤ Vp < 111.43	12								
2	106.43 ≤ Vp < 109.32		12							
3	102.50 ≤ Vp < 106.43	5		11						
4	97.15 ≤ Vp < 102.50	1	4	3	11					
5	94.79 ≤ Vp < 97.15			2		10				
6	92.65 ≤ Vp < 94.79			1	4		10			
7	90.41 ≤ Vp <92.65				3	7	8	10		
8	86.85 ≤ Vp < 90.41				2	10			10	
9	85.46 ≤ Vp < 86.85									9
Total # of Particles in each size range		18	16	17	20	27	18	10	10	9

Note: The empty spaces are filled with zero in actual response matrix calculations.

F.4b Response matrix in fractional form for PELTI, TAS=120.4 m/s, P=74,920 Pa.

Velocity Channels	Velocity Range	25 ≤ Dp < 30	20≤ Dp< 25	15 ≤ Dp < 20	10 ≤ Dp < 15	8 ≤ Dp < 10	6 ≤ Dp < 8	4 ≤ Dp < 6	2 ≤ Dp < 4	1 ≤ Dp < 2
1	109.32 ≤ Vp < 111.43	0.67	0	0	0	0	0	0	0	0
2	106.43 ≤ Vp < 109.32	0	0.75	0	0	0	0	0	0	0
3	102.50 ≤ Vp < 106.43	0.28	0	0.65	0	0	0	0	0	0
4	97.15 ≤ Vp < 102.50	0.06	0.25	0.18	0.55	0	0	0	0	0
5	94.79 ≤ Vp < 97.15	0	0	0.12	0	0.37	0	0	0	0
6	92.65 ≤ Vp < 94.79	0	0	0.06	0.2	0	0.56	0	0	0
7	90.41 ≤ Vp <92.65	0	0	0	0.15	0.26	0.44	1	0	0
8	86.85 ≤ Vp < 90.41	0	0	0	0.1	0.37	0	0	1	0
9	85.46 ≤ Vp < 86.85	0	0	0	0	0	0	0	0	1
Total # of Particles in each size range		1	1	1	1	1	1	1	1	1

F.4c Inverse response matrix for PELTI, TAS=120.4 m/s, P=74,920 Pa.

1.5	0	0	0	0	0	0	0	0
0	1.33	0	0	0	0	0	0	0
-0.6	0	1.55	0	0	0	0	0	0
0.06	-0.6	-0.5	1.82	0	0	0	0	0
0.2	0	-0.5	0	2.7	0	0	0	0
0.05	0.22	0.01	-0.7	0	1.8	0	0	0
-0.1	-0	0.2	0.02	-0.7	-0.8	1	0	0
-0.1	0.06	0.23	-0.2	-1	0	0	1	0
0	0	0	0	0	0	0	0	1

F.5a Response matrix for PELTI, TAS=140.3 m/s, P=53,379Pa.

Velocity Channels	Velocity Range	25 ≤ Dp < 30	20≤ Dp< 25	15 ≤ Dp < 20	10 ≤ Dp < 15	8 ≤ Dp < 10	6 ≤ Dp < 8	4 ≤ Dp < 6	2 ≤ Dp < 4	1 ≤ Dp < 2
1	129.57 ≤ Vp < 131.74	12								
2	126.53 ≤ Vp < 129.57		12							
3	122.16 ≤ Vp < 126.53	4	1	11						
4	115.80 ≤ Vp < 122.16	1	4	3	11					
5	112.82 ≤ Vp < 115.80			3		11				
6	110.03 ≤ Vp < 112.82				3		11			
7	107.37 ≤ Vp <110.03				4	5	3	10		
8	102.63 ≤ Vp < 107.37					2	11		10	
9	100.56 ≤ Vp < 102.63					5				10
Total # of Particles in each size range		17	17	17	18	23	25	10	10	10

Note: The empty spaces are filled with zero in actual response matrix calculations.

F.5b Response matrix in fractional form for PELTI, TAS=140.3 m/s, P=53,379Pa.

Velocity Channels	Velocity Range	25 ≤ Dp < 30	20≤ Dp< 25	15 ≤ Dp < 20	10 ≤ Dp < 15	8 ≤ Dp < 10	6 ≤ Dp < 8	4 ≤ Dp < 6	2 ≤ Dp < 4	1 ≤ Dp < 2
1	129.57 ≤ Vp < 131.74	0.71	0	0	0	0	0	0	0	0
2	126.53 ≤ Vp < 129.57	0	0.71	0	0	0	0	0	0	0
3	122.16 ≤ Vp < 126.53	0.24	0.06	0.65	0	0	0	0	0	0
4	115.80 ≤ Vp < 122.16	0.06	0.24	0.18	0.61	0	0	0	0	0
5	112.82 ≤ Vp < 115.80	0	0	0.18	0	0.48	0	0	0	0
6	110.03 ≤ Vp < 112.82	0	0	0	0.17	0	0.44	0	0	0
7	107.37 ≤ Vp <110.03	0	0	0	0.22	0.22	0.12	1	0	0
8	102.63 ≤ Vp < 107.37	0	0	0	0	0.09	0.44	0	1	0
9	100.56 ≤ Vp < 102.63	0	0	0	0	0.22	0	0	0	1
Total # of Particles in each size range		1	1	1	1	1	1	1	1	1

F.5c Inverse response matrix for PELTI, TAS=140.3 m/s, P=53,379Pa.

1.42	0	0	0	0	0	0	0	0
0	1.42	0	0	0	0	0	0	0
-0.5	-0.13	1.55	0	0	0	0	0	0
0.01	-0.51	-0.4	1.64	0	0	0	0	0
0.19	0.05	-0.6	0	2.09	0	0	0	0
-0	0.19	0.17	-0.6	0	2.27	0	0	0
-0	0.08	0.2	-0.3	-0.5	-0.3	1	0	0
-0	-0.09	-0	0.27	-0.2	-1	0	1	0
-0	-0.01	0.12	0	-0.5	0	0	0	1

F.6a Response matrix for PELTI, TAS=154.6 m/s, P=45,778 Pa.

Velocity Channels	Velocity Range	25 ≤ Dp < 30	20≤ Dp< 25	15 ≤ Dp < 20	10 ≤ Dp < 15	8 ≤ Dp < 10	6 ≤ Dp < 8	4 ≤ Dp < 6	2 ≤ Dp < 4	1 ≤ Dp < 2
1	141.71 ≤ Vp < 144.41	12								
2	137.76 ≤ Vp < 141.71		12							
3	131.93 ≤ Vp < 137.76	4	3	11						
4	123.14 ≤ Vp < 131.93		3	4	11					
5	118.62 ≤ Vp < 123.14			1	1	10				
6	114.22 ≤ Vp < 118.62				5	2	10			
7	110.40 ≤ Vp <114.22				2	4	5	10		
8	105.36 ≤ Vp < 110.40					2	12		9	
9	103.14 ≤ Vp < 105.36					1				9
Total # of Particles in each size range		16	18	16	19	19	27	10	9	9

Note: The empty spaces are filled with zero in actual response matrix calculations.

F.6b Response matrix in fractional form for PELTI, TAS=154.6 m/s, P=45,778 Pa.

Velocity Channels	Velocity Range	25 ≤ Dp < 30	20≤ Dp< 25	15 ≤ Dp < 20	10 ≤ Dp < 15	8 ≤ Dp < 10	6 ≤ Dp < 8	4 ≤ Dp < 6	2 ≤ Dp < 4	1 ≤ Dp < 2
1	141.71 ≤ Vp < 144.41	0.75	0	0	0	0	0	0	0	0
2	137.76 ≤ Vp < 141.71	0	0.67	0	0	0	0	0	0	0
3	131.93 ≤ Vp < 137.76	0.25	0.17	0.69	0	0	0	0	0	0
4	123.14 ≤ Vp < 131.93	0	0.17	0.25	0.58	0	0	0	0	0
5	118.62 ≤ Vp < 123.14	0	0	0.06	0.05	0.53	0	0	0	0
6	114.22 ≤ Vp < 118.62	0	0	0	0.26	0.11	0.37	0	0	0
7	110.40 ≤ Vp <114.22	0	0	0	0.11	0.21	0.19	1	0	0
8	105.36 ≤ Vp < 110.40	0	0	0	0	0.11	0.44	0	1	0
9	103.14 ≤ Vp < 105.36	0	0	0	0	0.05	0	0	0	1
Total # of Particles in each size range		1	1	1	1	1	1	1	1	1

F.6c Inverse response matrix for PELTI, TAS=154.6 m/s, P=45,778 Pa.

1.33	0	0	0	0	0	0	0	0
0	1.5	0	0	0	0	0	0	0
-0.48	-0.4	1.45	0	0	0	0	0	0
0.21	-0.3	-0.6	1.73	0	0	0	0	0
0.04	0.07	-0.1	-0.2	1.9	0	0	0	0
-0.16	0.18	0.48	-1.2	-0.5	2.7	0	0	0
-0	-0	0	0.07	-0.3	-0.5	1	0	0
0.07	-0.1	-0.2	0.54	0.04	-1.2	0	1	0
-0	-0	0.01	0.01	-0.1	0	0	0	1